DOCTORAL DISSERTATION

Studies on direct synthesis of alcohols from syngas over metal oxides catalysts

金属酸化物触媒を用いた合成ガスによるアルコールの直接合成の研究

Tao Zhang

(張 涛)

Tsubaki Laboratory

Department of Applied Chemistry

Graduate School of Science and Engineering

University of Toyama, Japan

Preface

Nowadays, the increasing demand on clean fuel and valuable chemicals ignited the research on catalytic converting carbon contained substances. Syngas, composed by hydrogen and CO, is an important platform material for synthesing gasoline, diesel oil and many valuable chemicals. Among all the downstream products of syngas, higher alcohols are considered to be valuable chemicals and fuel additives to offset the disadvantage of alcohols production from petrochemical and biological fermentation. Generally, alkali modified methanol catalysts (mainly composed by Cu based catalyst and ZnCr catalyst) are used to produce iso-butanol and methanol owing to the higher selectivity of alcohols and pre-longed catalyst life span.

However, there are still some important issues that need to be further studied in these catalysts system. For example, the exacting form and their effects of alkali metals on the activation of syngas and their influence on the mechanisms of carbon chain growth; The relatively high reaction temperature and pressure (400 ^{o}C, 10.0 MPa) versus the lower CO conversion (around 30 %) and higher selectivity of CO_2 (around 30 %) for K-ZnCr isobutanol catalyst. In this thesis, the effects of K_2O on the catalytic performance of Cu based catalyst was investigated by density functional theory (DFT) calculation. In addition, the performance of K-ZnCr catalyst was boosted by both controlling the co-precipitation temperature to increase the concentration of surface OH groups, and doping Ga^{3+} in the lattice of $ZnCr_2O_4$.

Through the above investigation, the following conclusions were obtained. That is (ⅰ) K_2O presents a strong adsorption on the Cu (111) surface owing to the strong interaction between atom O and surface Cu atoms. The difference of the adsorption energies among all the possible adsorption sites is very samll. Owing to the strong interaction, K_2O denotes its electrons to copper which further promotes the formation of CHO groups through CO hydrogenation and inhibit the formation of CH_3OH through OCH_3 hydrogenation that usually considered as the rate control step of methanol formation. In addition, on K_2O/Cu(111) surface, CH_2O reacted with CH_2 is the most favorable C_2 oxygenate formation route which presentes only a 1.10 eV activation energy. (ⅱ) By controlling the co-precipitation temperature during K-ZnCr catalyst preparation, the selectivity of alcohol and iso-butanol can be modulated. DRFTS of CO adsorption show that for the catalyst prepared at 60 ^oC, the relatively higher amount of surface OH groups was produced which facilitate the formation of COOH intermediates and further boost the performance of K-ZnCr iso-butanol catalyst. (ⅲ) Ga^{3+} can be used as an effective promoter to improve the selectivity and space time yield of alcohols of K-ZnCr catalyst. The reason lies in the formation of Ga^{3+} doped $ZnCr_2O_4$ compound which facilitate the formation of CHO and weakened the adsorption of CO_2 and H_2O. Owing to the formation of new catalyst structure and weakened adsorption of CO_2 and H_2O, water-gas-shift reaction is suppressed which promotes the efficiency of iso-butanol synthesis. The analysis to the structure of K-Ga_xZnCr catalysts show that the morphology of the catalysts and the interactions between ZnO and ZnCr spinel were all changed owing to the formation of the different compound. When the molar faction of

Ga^{3+} is lower than 1.10 %, ZG is the newly formed compound which promotes the performance of K-ZnCr catalyst. However, by further increasing the amount of Ga^{3+}, $ZnGa_2O_4$ is formed which only modify the surface acidity and basicity of K-ZnCr catalyst and showed negative impact on the performance of the catalyst.

By means of the above work, the roles of alkali oxides on the activation of CO and C_2 oxygenate formation and the goals that further improve the efficiency of K-ZnCr catalyst are all realized in this thesis. The research will throw light on further improving the performance of alkali modified methanol catalysts that used to directly synthesis of higher alcohols from syngas.

Contents

Chapter 1

Insight into activation of CO and initial C_2 oxygenate formation during synthesis of higher alcohols from syngas on the model catalyst K_2O/Cu(111) surface

On K_2O/Cu (111) surface, CHO, CH_2O and CH_2 originated from the H assisted dissociation of CO. CH_2CH_2O is the most favorable C_2 oxygenates formation pathway.

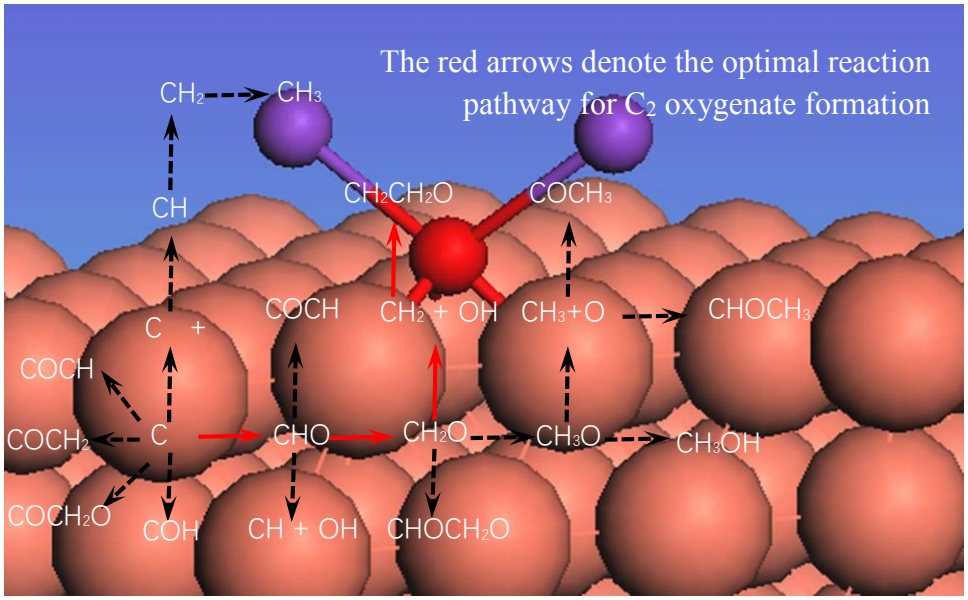

Abstract

Alkali-metal-modified Cu-based catalysts are important in low-temperature synthesis of methanol and higher alcohols from syngas. Spin-polarized density functional theory calculations with periodic slab models were performed for a K_2O/Cu(111) model catalyst to investigate the interactions between K_2O and the Cu(111) surface, and activation of CO. The results show that K_2O interacts strongly with the Cu (111) surface via electron transfer between K_2O and the Cu (111) surface. This changes CO activation and modulates the mechanism of formation of the initial C_2 oxygenates. Although K_2O significantly promotes CO direct dissociation, H-assisted dissociation of CO is still the most energetically favorable route. The optimal reaction pathway for C_2 oxygenate formation is proposed based on a climbing-image nudged elastic band calculation. The reactions starts with CO hydrogenation to yield the preferred monomers, i.e., CHO, CH_2O, and CH_2, through the pathways CO + H → CHO + H → CH_2O + H → CH_2 + OH, with reaction barriers of 0.92, 0.97, and 0.58 eV. The reaction of CH_2 with CH_2O is the main C_2 oxygenate formation route on the K_2O/Cu (111) surface. These results clarify the effects of K_2O on Cu-based catalysts and elucidate the mechanism of C_2 oxygenate formation during alcohol synthesis from syngas.

Keywords: CO, K_2O, C_2 oxygenates formation, Density functional theory

1.1 Introduction

Higher alcohols are important raw materials and are widely used in the chemical, pharmaceutical, and energy sectors [1-4]. They are mainly produced from petrochemicals or by biological fermentation [1]. A potential alternative route, i.e., direct synthesis from syngas (CO and H_2), is more efficient and environmentally friendly. Modification with an alkali-metal oxide of the Cu-based catalysts used for methanol production provides promising catalysts for the production of higher alcohols such as ethanol and isobutanol from syngas [3, 4]. In these catalysts, the alkali-metal oxide acts as an electron donor or structural auxiliary and plays an important role in stabilizing the surface structure of the catalyst, inhibiting hydrocarbon formation, and thereby boosting formation of higher alcohols[5-13]. Reports of previous studies show [1, 3, 7, 14-18] that K_2O is the preferred promoter because it can affect the electronic states of Cu surface species and adsorption of CO through alkali-metal–Cu interactions. Campos et al.[14] reported that K is adsorbed on the top sites of a Cu (111) surface through local specific interactions. Li et al. [15] used Kelvin probe to investigate the co-adsorption of CO and K on Cu (111) surface. They found that CO was adsorbed on a K-covered Cu (111) surface at room temperature, and that the work function changed with the degree of coverage by K (θ_K). An et al. [16] used a combination of transmission electron microscopy and density functional theory (DFT) calculations to clarify the effects of K deposition on the atomic and electronic structures, and the chemical activities of Cu_xO/Cu (111). The results showed pseudomorphic growth of K on the model catalyst up to a coverage of 0.19 ML. K binds to the surface by strong ionic

interactions with chemisorbed oxygen and weak electrostatic interactions with Cu ions. The deposited K has a strong impact on the electronic structure of the surface, and this induces a significant reduction in the work function and strong electron polarization. They also found that the presence of K does not promote CO adsorption on the model catalyst but accelerates CO_2 activation. Stelmachowski et al. [17] used the Kelvin method to investigate N_2O decomposition on an alkali-metal-modified Co_3O_4 catalyst. They reported that modification improved the decomposition performance and suggested that this is because the electronic nature of the alkali metal lowers the spinel work function. Ou et al. [18] performed a systematic study of Na- and Cs-promoted Cu (111) catalysts and reported a reduction in the dissociation activation barrier of CO_2. Although the described studies have improved our understanding of the effects of K on a Cu surface, the mechanism of CO activation on Cu surfaces modified with an alkali-metal oxide is still unclear for two reasons: (1) the electronic state of an alkali metal deposited on a surface differs from that of a surface-deposited alkali-metal oxide and (2) the larger configuration of the alkali-metal oxide affects the geometric configuration of the initial state, the transition state, and the final states, and modulates the reaction energy and reaction barrier of a specific elementary reaction.

Theoretical investigations of the mechanism of C_2 oxygenate formation on a Cu surface have been performed to clarify the initial C–C bond formation process in alcohol synthesis by CO hydrogenation [5, 19, 20]. Zheng et al. [19] investigated the possible mechanisms of ethanol formation from syngas on a Cu (100) surface and found that CH_3 insertion into CHO to give CH_3CHO is the most favorable reaction (the

activation energy is 0.44 eV), and is responsible for C_2 oxygenate formation. In contrast, Zhang et al. [20] reported that C_2 oxygenates are formed mainly by CO insertion into CH_2 on a Cu (110) surface, with an activation barrier of 0.47 eV. Although deposition of K modulates the surface acidity or basicity of a Cu-based catalyst [21], there are no reports of theoretical studies of K_2O-promoted Cu-based catalysts for C_2 oxygenate formation from syngas. The activation of CO on a K_2O-promoted Cu surface and the mechanism of C_2 oxygenate formation also need to be clarified.

In this study, to address these gaps in the literature, a K_2O-modified Cu (111) model catalyst was constructed and DFT calculations were used to investigate the effects of K_2O on CO activation and C_2 oxygenate formation.

1.2 Computational Detail

1.2.1 Surface model

Cu (111) surface was obtained from the experimental face centered cubic (fcc) crystal structure with the lattice parameter of 3.64 Å[22]. A periodic p (3×3) unit cell comprising nine atoms in each layer was used, which corresponds to an adsorbed surface of a 1/9 of a monolayer. The surface was modeled using a three-layer slab model with a 15 Å vacuum slab. In the optimization process, the atoms in the upper two layers together with the K_2O, CO and other adsorbents were allowed to relax, whereas, the bottom one layer was fixed at their bulk position. The four different adsorption sites: top, bridge (bri), fcc hollow and hexagonal closed packed (hcp) hollow were shown as X. Sun. et al. [23].

K_2O/Cu (111) surface was obtained based on the optimized Cu (111) surface by investigate the adsorption behavior of K_2O on Cu (111) surface.

1.2.2 Calculation methods

Spin-polarized DFT calculations were performed using the Vienna abinito simulation package (VASP) [24, 25]. The interaction between ionic cores and electrons was described using the projector-augmented wave (PAW) method[26]. The exchange-correlation energy was calculated within the generalized gradient approximation (GGA) together with the Perdew-Burke-Ernzerhof (PBE) method [27, 28]. After the optimization by PBE, revised Perdew-Burke-Ernzerhof (RPBE) functional was adopted to get the better agreement with experiment for the absorption energy of CO [28-30]. A plane wave basis set was 450 eV to solve the Kohn-Sham equations. The Brillouin zone was sampled using a 3×3×1 Monkhorst-Pack k-points with the fessel-Paxton smearing of 0.10 eV. The relaxation of the electronic degrees of freedom was assumed to be converged, if the total energy change and the band structure energy change between two steps are both smaller than 10^{-5} eV. A force difference between two steps less than 0.01 eV/Å was used as the criterion for convergence of ionic relax.

The climbing-image nudged elastic band methods (CI-NEB)[31, 32] were used to investigated the transition states, and vibrational frequencies were analyzed to evaluate a transition state with only one imaginary frequency. The transition state was thought to be converged when the forces acting on the atoms are all lower than 0.05 eV/atom for the various degree of freedom atom. In addition, in the discussion of the DFT results,

zero point energy (ZPE) corrections were included in this study if necessary. The molecules in the gas phase were calculated using a 10×10×10 Å cubic unit cell.

The adsorption energy that was used to measure the strength of adsorbent-substrate adsorption are defined as follows:

$E_{ads} = E_{sub} + E_{mol} - E_{mol/sub}$

Where E_{sub} and E_{mol} are the total energies of substrate and free adsorbent alone, $E_{mol/sub}$ is the total energy of adsorbent-substrate system in the equilibrium state. With this definition, positive values of adsorption energy denote that adsorption is more stable than the corresponding substrate and free molecules.

For the dissociate of CO on the K_2O/Cu (111) surface, the reaction energy (ΔE) and activation barriers (E_a) were calculated on the basis of the following equations:

$$\Delta E = E_{pro/[K2O/Cu(111)]} - E_{rea/[K2O/Cu(111)]}$$

$$E_a = E_{TS/[K2O/Cu(111)]} - E_{rea/[K2O/Cu(111)]}$$

Where $E_{pro/[K2O/Cu(111)]}$ is the total energy for the products, $E_{rea/[K2O/Cu(111)]}$ is the total energy for the reactants and $E_{TS/[K2O/Cu(111)]}$ is the energy of transition state of an elementary reaction on K_2O/Cu (111) surface.

1.3. Results and discussion

1.3.1 Adsorption of K_2O on Cu (111) surface

The binding abilities of K_2O at interfacial sites were compared by calculating the K_2O adsorption energies at various sites on the Cu (111) surface, including O atom adsorption at fcc, hcp, top, and bri sites. The detailed adsorption configurations are

shown in Fig. 1.1. On the Cu (111) surface, the fcc site is the primary binding position for K_2O adsorption, with an energy release of 4.60 eV. The binding strengths of the top, bri, and hcp sites with K_2O are lower (4.57-4.58 eV, Table 1.1). Our calculated binding energies are not consistent with recently published theoretical results. Wang et al. obtained a binding energy of 3.47 eV at the GGA-PW91 level [33], which is 1.13 eV lower than that in our work. The deviation of the GGA-PW91 value from our PBE value is at least partially explained by the different calculation levels.

The detailed adsorption configurations of K_2O at the above sites (Table 1.1 and Fig. 1.1) show that there is little difference among the geometric properties of K_2O adsorbed on different sites on the Cu (111) surface. Our calculated geometric structures for K_2O are consistent with those reported by Wang et al.[33] and Zasada et al. [10]. The small impacts of surface sites on the adsorption configurations and binding energies can be ascribed to the high mobility of K_2O on Cu (111) surfaces, as shown by the calculated results reported by Petersen et al. [34].

To explore the effects of K_2O on the electron distribution on the Cu (111) surface, we analyzed the Bader charges on K_2O/Cu (111) and Cu (111) surfaces (Table 1.2). The charge on the Cu surface with adsorbed K_2O is more negative than that on the clean Cu (111) surface. Although the calculated Bader charge is smaller than that reported by Wang [33], the trend in the charge distribution in our calculations is consistent with Wang's results. This indicates that K_2O donates electrons to the Cu (111) surface, and this interaction would modulate CO activation.

1.3.2 Dissociation of CO on K_2O/Cu (111) surface

The CO activation pathways on catalysts for alcohol synthesis from CO have been extensively investigated in previous studies [5, 12, 19, 20, 34-37]. The direct dissociation of CO can start with C–O bond scission to form adsorbed C and O, followed by C–H bond formation to produce CH_x (x = 1, 2, and 3). Alternatively, C–H or C–O bond formation can occur first to give a CH_xO intermediate which can further hydrogenated into CH_x; these C_1 monomers can then participate in the formation of C_2 oxygenates.

In this work, DFT calculations were performed on K_2O/Cu (111) surfaces to investigate CO adsorption. Then CO activation was investigated by CI-NEB analysis to verify the reaction routes of CO on a K_2O-promoted Cu-based catalyst. Adsorption of the reactants and all possible intermediates involved in CO activation on clean and K_2O-promoted Cu (111) surfaces were all considered. The preferential adsorption positions and corresponding adsorption energies are listed in Table 1.3 [K_2O/Cu(111)] and Table 1.4 [Cu(111)]. According to our DFT calculations, CO on Cu (111) preferentially occupies the hcp site, with a binding energy 1.06 eV (Table 1.4); this agrees well with the results of other calculations at a similar level of theory [19,20,22,35,36]. We found that the adsorption energy of CO after K_2O modification (1.06 eV) is the same as that for the unmodified surface, but the adsorption energies of C, O, and CHO are changed by K_2O addition. The calculated results are consistent with those from Mei's and Liu's study [12,38]. A comparison of the activation routes on clean and K_2O-doped Cu (111) surfaces shows differences between the two catalysts. The activation barrier for direct dissociation of CO decreases by 2.50 eV after K_2O

promotion (3.79 eV vs 1.29 eV, see Fig. 1.2 and Fig. 1.3). This suggests that K_2O makes direct dissociation of CO energetically favorable. This trend is in accordance with those seen in previous studies [10]. Similar results were obtained for CHO formation (Fig. 1.2 and Fig. 1.3); the reaction barrier decreases by 0.18 eV (1.10 vs 0.92 eV). The effects of K_2O on COH formation were also investigated by DFT calculations. Unlike direct dissociation and CHO formation, the activation barrier is 1.98 eV higher after K_2O modification (4.18 vs 2.20 eV, Fig. 1.2 and Fig 1.3). The different effects of K_2O addition on CO activation can be at least partially explained by enhancement of the adsorption energies of C, O, CHO, and COH caused by electrostatic interactions (Tables 1.3 and 1.4) [38]. Similar trends in the effects of K_2O or K on the activation of CO and related species in many reactions associated with CO hydrogenation have been reported. Zhao et al. [35] showed that K_2O adsorption can stabilize or destabilize surface CH_x species and modify the effective barriers because of short-ranged promotion and electronic effects. Petersen et al. [34] viewed the interactions between co-adsorbed CO and zero-valent K, which can enhance CO adsorption and weaken the C–O bond. Erikat [39] found that K atom could stabilize reactants and increase the reactivity of an Ir (100) catalyst in CO oxidation. In our study, a similar pattern was observed for the effects of K_2O on CO adsorption, and the adsorption and reaction trends are in accordance with those previously reported.

Bader charge analysis was performed to investigate the origins of these differences. The data in Table 1.2 show that when CO is adsorbed on a K_2O/Cu (111) surface, the charge on CO becomes more negative because both Cu and K_2O donate charge to CO

(see Table 1.2). The obtained patterns of interactions between K_2O, CO, and the catalyst are similar to those for CO adsorption on a K-doped MoS_2 (100) surface [12]. The altered surface electron distribution on CO and the K_2O/Cu (111) surface modulate CO activation. This will be discussed in section 1.3.3.

On the basis of the above results, we conclude that the hydrogenation of CO to CHO and direct dissociation to C and O are more plausible. Fig. 1.2 shows that the barriers to formation of CHO and C + O are 0.92 and 1.29 eV, respectively. Both reactions are more favorable than COH formation, and CHO formation is preferred. The CO adsorbed on the K_2O/Cu (111) surface undergoes hydrogenation to form CHO.

1.3.3 Formation of CH_x (x = 1–3)

Light hydrocarbons such as methane, ethane, ethylene, propane, and propylene are the major byproducts of higher alcohol synthesis from syngas. CH_x species are considered to be the monomers that polymerize to form these hydrocarbons, therefore the origin of these species is important in studying the use of carbon resources. Two previously reported possible pathways were investigated in this study. one is the direct hydrogenation of the C atom, the other is H-assisted dissociation of CH_xO (x = 1, 2, and 3). The results of the two possible pathways are calculated and discussed in the following text.

1.3.3.1 CH_x (x = 1–3) formation by dissociated CO hydrogenation

CH_x (x = 1, 2, and 3) formation from C and H on the K_2O/Cu (111) surface were studied with the aim of understanding the possibility of CH_x formation via dissociated

CO hydrogenation.

The formation of CH_x starts with C–O bond scission to produce adsorbed C and O, followed by C–H bond formation to add the first, second, and third H atoms to C (C + H → CH + H → CH_2 + H → CH_3). In this pathway, the first H can be transferred to a bri site on the Cu surface, to give TS 3-1 with a C–H distance of 1.90 Å (Fig. 1.4). The C–H bond formation step is exothermic by 1.35 eV via a 0.89 eV barrier (Fig. 1.4 A), and leads to the formation of a CH intermediate at the top site of the Cu surface. The second hydrogenation occurs by C–H bond formation with CH species, in which H can be transferred to CH via TS 3-2 (Fig. 1.4). The C–H bond formation step is exothermic by 0.25 eV (Fig. 1.4 B), and the activation barrier is much lower than that for the first C–H bond formation (0.21 vs 0.89 eV). This suggests that formation of the second C–H bond would easily proceed. In the third step, the H is transferred from a hollow site on the Cu surface to CH_2; the distance between C atom and dissociated H atom decreases to 3.91 Å in the transition state (Fig.1.4). Formation of the C–H bond is endothermic by 0.01 eV and the activation barrier is high (1.85 eV, Fig. 1.4 C). This indicates that it would be difficult for this process to proceed.

The above analysis suggests that CH_2 is the dominant species formed from CO direct dissociation because of the lower activation energy (0.21 eV) and moderate reaction energy.

1.3.3.2 CH_x formation by CH_xO (x = 1–3) hydrogenation

As mentioned earlier, another crucial pathway for CH_x formation on a K_2O/Cu (111) surface is H-assisted dissociation of CH_xO (x = 1, 2, and 3). For CH formation,

the reaction starts with CHO hydrogenation. Fig. 1. 5 show that the barriers to formation of CHOH, CH + OH, and CH_2O are 0.92, 1.28, and 0.69 eV, respectively. The figure also shows that the formation barriers for the three mentioned species are 0.47, −0.09, and −0.34 eV, respectively. Accordingly, CH_2O formation is more favorable on the K_2O/Cu(111) surface.

Similarly, CH_2O hydrogenation to CH_2 and OH is preferred to formation of CH_2OH and hydrogenation to CH_3O (Fig.1.6). Higher barriers, i.e., 1.49 and 0.98 eV, are obtained for the formation of CH_2OH and CH_3O, respectively, whereas a calculated barrier of 0.67 eV is obtained for the formation of CH_2. In addition, Fig. 1.6 shows that the production of CH_2 and OH is more favorable than CH_2OH and CH_3O formation; this is because of the lower formation energy (−0.35 vs 0.19 eV and −0.76 eV) on the K_2O/Cu (111) surface. We therefore conclude that CH_2 is the most favored monomer produced by CH_2O hydrogenation.

The calculated barrier for CH_3 formation by CH_3O hydrogenation is 1.51 eV (Fig.1.7), with C–O bond cleavage that is endothermic by 0.57 eV. This leads to the formation and adsorption of CH_3 at the bri site of the Cu surface via C. Some interesting comparisons can be made regarding the formation of CH_3 through CH_2 hydrogenation and CH_3O dissociation. An activation barrier difference of 0.34 eV is observed. However, the activation energy for the two pathways are all above 1.50 eV (1.51 vs 1.85 eV), which indicates that CH_3 formation would hardly proceed in our limited study.

The above analysis of CH_x formation suggests that when H reacts with CO adsorbed on the K_2O/Cu (111) surface, CO → CHO → CH_2O → CH_2 is the optimal

pathway for CH_x formation, and CH_2 is the most favored CH_x monomer, both kinetically and thermodynamically.

1.3.4 Methanol formation by CH_3O hydrogenation

On a Cu-based catalyst, the hydrogenation of CH_3O to produce CH_3OH is considered to be the slow step in methanol synthesis from syngas [22]. On a K_2O/Cu (111) surface, methanol formation can start from the reaction of CH_3O and H, with an activation barrier of 3.32 and heat release of 0.05 eV (Fig.1.7). Calculations were also performed for methanol formation on a Cu (111) surface for comparison. Our calculations gave an activation barrier of 1.43 eV, which is endothermic by 0.19 eV (Fig.1.8). These values are consistent with the available theoretical results (listed in Table 1.5). The reaction barrier and reaction energy are clearly higher when K_2O is present, which implies that methanol formation is inhibited by adding this auxiliary.

The difference for the structures of the transition states TS 3-11(Fig. 1.7 and Fig 1.8) for this pathway show that the distance between CH_2OH and H on the K_2O/Cu (111) surface is 1.93 Å larger than that on a pure Cu (111) surface. The deviations in the energies when K_2O is present can be at least partially explained by interactions between O and K, which alter the configuration of the transition state and increase the reaction barrier by 1.89 eV.

1.3.5 C_2 oxygenate formation

Having clarified CO activation on a K_2O-promoted Cu (111) surface, we then

investigated the origins of C_2 oxygenates in the K_2O/Cu system. The possible reaction pathways among all the monomers are shown in Fig. 1.9. These possible elementary reactions can be divided into three categories: (1) reactions between CH_x and CO, (2) insertion of CH_x into CHO, and (3) C–C chain formation of C_2 oxygenates via reactions between monomers such as CHO, CH_2O, CH_2, and CO. The potential energy diagram and detailed structures for these reactions are shown in Fig. 1.10 and Figs. 1.11-1.12.

Calculations were performed for three possible reaction pathways for CH_x insertion into CO. Fig. 1.10 show that the barriers for forming CHCO, CH_2CO, and CH_3CO are 0.66, 1.78, and 1.43 eV, respectively. All the reactions are exothermic, and CHCO formation is preferred. CH_xCO formation has been investigated by many researchers. Zhang et al. [20] reported that the activation barriers and reaction energies on a Cu (110) surface are 0.46 and −0.34 eV for $CH_2 + CO \rightarrow CH_2CO$, and 1.07 and −0.08 eV for $CH_3 + CO \rightarrow CH_3CO$. Zheng et al. [19] reported an activation barrier of 1.01 eV and a reaction energy of −0.21 eV for CH_3CO formation from CH_3 and CO on a Cu (100) surface.

The results discussed above show that the activation barriers and reaction energies obtained in previous studies differ from those obtained in the present study (see Table 1.6). This indicates that the C_2 oxygenate formation route is modulated by K_2O promotion. The activation barriers for the three possible elementary reactions increase with increasing number of H atoms in the CH_x group. An examination of the effects of K_2O and the volume of CH_x groups suggests that the interactions between K and O will have a significant impact on the configurations of CH_3 and CO, and this will change

the possible C_2 oxygenate formation route.

After studying the possible reactions between CH_x and CO, we investigated the possible reactions between CHO and CH_x. The activation barriers for CHOCH, $CHOCH_2$, and $CHOCH_3$ formation are 0.01, 1.08, and 1.74 eV, respectively, with reaction energies of −1.40, −1.91, and −1.08 eV, respectively (Fig.1.11). Some interesting observations were also made to probe the possible C_2 oxygenate formation routes from CHO and CH_x. Wang et al. investigated CHOCH formation through CHO and CH on CuZn (211) and Cs_2O–CuZn (211) surfaces; activation barriers of 1.04 and 0.85 eV were obtained [5]. These values are much higher than those obtained from our calculations. The differences between our results and those reported by Wang may arise from the differences between the basicities and sizes of K_2O and Cs_2O [21]. The activation barriers of 0.51 and 0.12 eV for $CHOCH_3$ formation on Cu (111) and Cu (100) surfaces are obtained respectively by Zheng et al. [19] . The values obtained from our calculations are smaller than those reported by Wang but larger than those reported by Zheng. The deviations are probably the result of promotion by the alkali-metal oxide, which changes the geometric structures of the adsorbed monomers involved in the reaction by electrostatic interactions, as discussed above.

A comparison of the trends in the activation barriers shows that the values gradually increase with increasing number of H atoms. This trend is similar to that for reactions between CH_x and CO. We conclude that stronger interactions between H atoms in CHO and CH_x and O in K_2O and CHO altered the energies and configurations of the transition states.

As discussed in section 1.3.3, CHO, CH_2O, and CH_2 are the predominant monomers formed during CO hydrogenation on a K_2O/Cu (111) surface. Calculations were performed to investigate the possibilities of C–C bond formation between CO and these monomers and the interactions among CHO, CH_2O, and CH_2. For C–C bond formation from CHO and CO, an activation barrier of 0.39 eV and a reaction energy of 0.23 eV were obtained (Fig. 1.12). In transition state TS 3-18, CO binds on the bri site through its C atom, CHO is adsorbed on the top site through the C atom, and the distance between the two bases is shortened to 3.28 Å. The calculated activation energies for this elementary reaction are 0.65 and 0.46 eV higher than those for the reactions on CuZn (211) and Cs_2O–CuZn (111) surfaces [5], respectively, and the reaction energies are 1.78 and 2.00 eV higher than those with the CuZn and Cs_2O–CuZn catalysts, respectively. This indicates that the reaction process on the K_2O/Cu (111) catalyst is different from that on the CuZn catalyst.

Other possible pathways for C_2 oxygenate formation from CH_2, CHO, CO, and CH_2O were also investigated. Fig. 1.12 shows the configurations of the initial state, transition state, and final state for the pathways TS 3-19 ($CH_2O + CH_2 \rightarrow CH_2OCH_2$), TS 3-20 ($CH_2O + CO \rightarrow CH_2OCO$), and TS 3-21 ($CH_2O + CHO \rightarrow CH_2OCHO$). The reaction coordinates of the three elementary reactions are also shown in Fig. 1.12. For TS 3-19, the reaction has an activation barrier of 0.41 eV and is exothermic by 0.61 eV. The C–C bond distance between CH_2O and CH_2 decreases from 3.57 Å in the initial state to 3.00 Å in the transition state to 1.68 Å in the final state. For C–C bond formation from CH_2O and CO, our DFT calculation gave an activation barrier of 1.09 eV and

reaction energy of 0.90 eV. The distance between CH_2O and CO decreases from 3.46 Å in the initial state to 2.39 Å in the transition state to 1.73 Å in the final state. For C–C bond formation from CH_2O and CHO, the reaction has an activation barrier of 0.46 eV and is exothermic by 0.24 eV. The distance between CH_2O and CHO decreases from 3.15 Å in the initial state to 2.32 Å in the transition state to 1.52 Å in the final state.

The results of our calculations indicate that the reaction between CHO and CH has the lowest activation barrier (only 0.01 eV, Fig. 1.12), but CH formation via the direct route and the H-assisted route are both energy demanding. Other possibilities for C–C bond formation should be considered. A comparison of the energy profiles of the elementary reactions that occur between most monomers clearly shows (Fig. 1.12) that TS 3-19 is the most favorable C_2 oxygenate formation route because it has the lowest activation barrier and reaction energy.

1.4. Conclusions

In this study, spin-polarized DFT calculations with a periodic slab model were used to investigate the electronic states, CO activation, and C_2 oxygenate formation route on a K_2O/Cu (111) surface. Our results show that the Cu (111) surface was modulated by K_2O addition. CO activation was altered by this modulation; H-assisted dissociation is more energetically favorable than CO direct dissociation for CO activation. For CHO formation by H-assisted dissociation of CO, CH_2O and CH_2 are the most favorable monomers. Methanol formation was retarded by K_2O modification of Cu (111) because of the increased activation energy of the rate-determining step in

CH_3O hydrogenation.

The reactions between CHO, CH_2, and CO, i.e., the favored monomers, were further probed to investigate the possible pathways for initial C_2 oxygenate formation. Our results show that CH_2 insertion into CH_2O to form CH_2CH_2O is the most favorable reaction route to C_2 oxygenates, both kinetically and thermodynamically. The results show that boosting H-assisted dissociation of CO increases the concentrations of CHO, CH_2, and CH_2O on K_2O-promoted Cu-based catalysts, and this eventually enhances production of higher alcohols.

References

[1] H.T. Luk, C. Mondelli, D.C. Ferre, J.A. Stewart, J. Perez-Ramirez, Status and prospects in higher alcohols synthesis from syngas, Chem. Soc. Rev. 46 (2017) 1358-1426.

[2] L. Tan, G. Yang, Y. Yoneyama, Y. Kou, Y. Tan, T. Vitidsant, N. Tsubaki, Iso-butanol direct synthesis from syngas over the alkali metals modified Cr/ZnO catalysts, Appl. Catal., A. 505 (2015) 141-149.

[3] Y. Wu, H. Xie, S. Tian, N. Tsubaki, Y. Han, Y. Tan, Isobutanol synthesis from syngas over K-Cu/ZrO_2-La_2O_3(x) catalysts: Effect of La-loading, J. Mol. Catal. A: Chem. 396 (2015) 254-260.

[4] X. Li, H. Xie, X. Gao, Y. Wu, P. Wang, S. Tian, T. Zhang, Y. Tan, Effects of calcination temperature on structure-activity of K-ZrO_2/Cu/Al_2O_3 catalysts for ethanol and isobutanol synthesis from CO hydrogenation, Fuel.227 (2018) 199-207.

[5] J. Sun, Q. Cai, Y. Wan, S. Wan, L. Wang, J. Lin, D. Mei, Y. Wang, Promotional effects of cesium promoter on higher alcohol synthesis from syngas over cesium-promoted Cu/ZnO/Al_2O_3 catalysts, Acs Catal. 6 (2016) 5771-5785.

[6] J. Sun, S. Wan, F. Wang, J. Lin, Y. Wang, Selective synthesis of methanol and higher alcohols over Cs/Cu/ZnO/Al_2O_3 catalysts, Ind. Eng. Chem. Res. 54 (2015) 7841-7851.

[7] S. Tian, S. Wang, Y. Wu, J. Gao, P. Wang, H. Xie, G. Yang, Y. Han, Y. Tan, The role of potassium promoter in isobutanol synthesis over Zn-Cr based catalysts, Catal. Sci. Technol. 6 (2016) 4105-4115.

[8] D. He, Y. Ding, H. Yin, T. Wang, H. Zhu, Effect of alkali promoters on catalytic performance of MnOx/ZrO_2 for synthesis of methanol and isobutanol from syngas, Chin. J. Catal. 24 (2003) 111-114.

[9] C. Huo, B. Wu, P. Gao, Y. Yang, Y. Li, H. Jiao, The mechanism of potassium promoter: enhancing the stability of active surfaces, Angew. Chem. 50 (2011) 7403-7406.

[10] F. Zasada, P. Stelmachowski, G. Maniak, J.-F. Paul, A. Kotarba, Z. Sojka, Potassium promotion of cobalt spinel catalyst for N_2O decomposition-accounted by work function measurements and DFT modelling, Catal. Lett. 127 (2009) 126-131.

[11] V.P. Santos, B. van der Linden, A. Chojecki, G. Budroni, S. Corthals, H. Shibata, G.R. Meima, F. Kapteijn, M. Makkee, J. Gascon, Mechanistic insight into the synthesis of higher alcohols from syngas: the role of K promotion on MoS_2 catalysts, Acs Catal. 3 (2013) 1634-1637.

[12] A. Andersen, S.M. Kathmann, M.A. Lilga, K.O. Albrecht, R.T. Hallen, D. Mei,

Effects of potassium doping on CO hydrogenation over MoS_2 catalysts: a first-principles investigation, Catal.Commun. 52 (2014) 92-97.

[13] M. Calatayud, C. Minot, Effect of alkali doping on a V_2O_5/TiO_2 catalyst from periodic DFT calculations, J. Phys. Chem. C, 111 (2007) 6411-6417.

[14] L. PadillaCampos, A. ToroLabbe, J. Maruani, Theoretical investigation of the adsorption of alkali metals on a Cu(111) surface, Surf. Sci. 385 (1997) 24-36.

[15] H. Li, L. Zhu, Y. Xu, A model of normal transfer of electrons on CO+K/Cu(111) surface, Appl. Surf. Sci. 126 (1998) 342-346.

[16] W. An, F. Xu, D. Stacchiola, P. Liu, Potassium-Induced effect on the structure and chemical activity of the CuxO/Cu(1 1 1) ($x \leq 2$) surface: a combined scanning tunneling microscopy and density functional theory study, ChemCatChem, 7 (2015) 3865-3872.

[17] P. Stelmachowski, G. Maniak, A. Kotarba, Z. Sojka, Strong electronic promotion of Co_3O_4 towards N_2O decomposition by surface alkali dopants, Catal. Commun. 10 (2009) 1062-1065.

[18] L. Ou, Y. Chen, J. Jin, Theoretical insights into the alkaline metal M (M = Na and Cs) promotion mechanism for CO_2 activation on the Cu(111) surface, Rsc Adv. 6 (2016) 67866-67874.

[19] H. Zheng, R. Zhang, Z. Li, B. Wang, Insight into the mechanism and possibility of ethanol formation from syngas on Cu(100) surface, J. Mol. Catal.A: Chem. 404-405 (2015) 115-130.

[20] R. Zhang, X. Sun, B. Wang, Insight into the preference mechanism of CHx(x= 1–3) and C–C chain formation involved in C_2 oxygenate formation from syngas on the

Cu(110) surface, J. Phy.Chem. C, 117 (2013) 6594-6606.

[21] E. Heracleous, E.T. Liakakou, A.A. Lappas, A.A. Lemonidou, Investigation of K-promoted Cu-Zn-Al, Cu-X-Al and Cu-Zn-X (X = Cr, Mn) catalysts for carbon monoxide hydrogenation to higher alcohols, Appl. Catal. A., 455 (2013) 145-154.

[22] L.C. Grabow, M. Mavrikakis, Mechanism of methanol synthesis on Cu through CO_2 and CO hydrogenation, Acs Catal. 1 (2011) 365-384.

[23] X. Sun, R. Zhang, B. Wang, Insights into the preference of CHx(x=1-3) formation from CO hydrogenation on Cu(111) surface, Appl. Surf. Sci. 265 (2013) 720-730.

[24] G. Kresse, J. Furthmuller, Efficiency of ab-initio total energy calculations for metals and semiconductors using a plane-wave basis set, Comput. Mater. Sci. 6 (1996) 15-50.

[25] G. Kresse, J. Furthmuller, Efficient iterative schemes for ab initio total-energy calculations using a plane-wave basis set, Phys. Rev. B 54 (1996) 11169-11186.

[26] G. Kresse, D. Joubert, From ultrasoft pseudopotentials to the projector augmented-wave method, Phys. Rev. B 59 (1999) 1758-1775.

[27] J.P. Perdew, K. Burke, M. Ernzerhof, Generalized gradient approximation made simple, Phys. Rev. Lett. 77 (1996) 3865-3868.

[28] A.A. Gokhale, S. Kandoi, J.P. Greeley, M. Mavrikakis, J.A. Dumesic, Molecular-level descriptions of surface chemistry in kinetic models using density functional theory, Chem. Eng. Sci. 59 (2004) 4679-4691.

[29] B.T. Loveless, C. Buda, M. Neurock, E. Iglesia, CO chemisorption and dissociation at high coverages during CO hydrogenation on Ru catalysts, J. Am. Chem.

Soc. 135 (2013) 6107-6121.

[30] M. Gajdos, J. Hafner, CO adsorption on Cu(111) and Cu(001) surfaces: Improving site preference in DFT calculations, Surf. Sci. 590 (2005) 117-126.

[31] G. Henkelman, B.P. Uberuaga, H. Jonsson, A climbing image nudged elastic band method for finding saddle points and minimum energy paths, J. Chem. Phys. 113 (2000) 9901-9904.

[32] D. Sheppard, R. Terrell, G. Henkelman, Optimization methods for finding minimum energy paths, J. Chem. Phys. 128 (2008).

[33] Y. Wang, G. Wang, Water dissociation on K_2O-pre-adsorbed transition metals: a systematic theoretical study, Phys. Chem. Chem. Phys. 20 (2018) 19850-19859.

[34] M.A. Petersen, M.J. Cariem, M. Claeys, E. van Steen, A DFT perspective of potassium promotion of chi-Fe5C_2(100), Appl. Catal., A. 496 (2015) 64-72.

[35] S. Zhao, X. Liu, C. Huo, Y. Li, J. Wang, H. Jiao, Potassium promotion on CO hydrogenation on the chi-Fe_5C_2(111) surface with carbon vacancy, Appl. Catal.,A. 534 (2017) 22-29.

[36] N. Yang, A.J. Medford, X. Liu, F. Studt, T. Bligaard, S.F. Bent, J.K. Norskov, Intrinsic selectivity and structure sensitivity of rhodium catalysts for C_{2+} oxygenate production, J. Am. Chem. Soc. 138 (2016) 3705-3714.

[37] S.S.C. Chuang, R.W. Stevens, R. Khatri, Mechanism of C_{2+} oxygenate synthesis on Rh catalysts, Top. Catal. 32 (2005) 225-232.

[38] Z. Liu, P. Hu, An insight into alkali promotion: a density functional theory study of CO dissociation on K/Rh(111), J. Am. Chem. Soc. 123 (2001) 12596-12604.

[39] I.A. Erikat, First principle study on alkali metals promotion of CO oxidation over Ir(100), Physica Status Solidi B-Basic Solid State Physics, 253 (2016) 983-989.

[40] Z. Chen, K.M. Neyman, K.H. Lim, N. Rösch, CH_3O decomposition on PdZn(111), Pd(111), and Cu(111). a theoretical study, Langmuir, (2004) 8068-8077.

[41] R. Zhang, G. Wang, B. Wang, Insights into the mechanism of ethanol formation from syngas on Cu and an expanded prediction of improved Cu-based catalyst, J. Catal. 305 (2013) 238-255.

[42] S. Wang, M. Jian, H. Su, W. Li, First-principles microkinetic study of methanol synthesis on Cu(221) and ZnCu(221) Surfaces, Chin. J. Chem. Phys. 31 (2018) 284-290.

Table 1.1 Adsorption configurations of K_2O on the Cu (111) surface from the four initial sites.

Absorption Site	d_{Cu-O}	d_{K-O}	∠K-O-K	E_{ads} (eV)
	2.009	2.540	108.385	4.57
top	2.044	2.551		
	2.020			
	2.013	2.554	109.50	4.58
bridge	2.048	2.535		
	2.014			
	2.041	2.563	107.657	4.60
Fcc	2.006	2.543		
	2.016			
	2.017	2.534		
Hcp	2.050	2.5554	108.817	4.57
	2.015			

Table 1.2 The bader charge distribution of CO adsorbed on Cu(111) and K_2O/Cu(111) surface.

surface model	Bader charger distribution		
	Cu	CO	K_2O
Cu(111)	0.0002		
CO/Cu(111)	0.4486	-0.4487	
K_2O/Cu(111)	-0.3347		0.3346
CO/K_2O/Cu(111)	0.3421	-0.8243	0.4817

Table 1.3 Adsorption energies and key geometric parameters for various relevant species involved in the dissociation of CO on the K_2O/Cu(111) surface.

Species	E_{ads} (eV)	Adsorption configuration	D_{Cu-X} (Å)	Bonding details	
				Bond length or angle	Length (Å)
C	8.79	H: through C	2.00		
O	7.49	H: through O	2.03		
H	3.59	H: through H	1.76		
CO	1.06	H: through C	2.01	C-O	1.25
COH	2.36	B: through C	1.97/2.48	C=O/O-H, ∠OCH	1.27/1.13,113.99
CHO	4.67	T: through C	1.99	C-O/O-H, ∠COH	1.43/0.99,103.58

H: the hcp site, B: the bridge site and T: the top site.

Table 1.4 Adsorption energies and key geometric parameters for various relevant species involved in the dissociation of CO on the Cu(111) surface.

Species	E_{ads} (eV)	Adsorption configuration	D_{Cu-X} (Å)	E_{ads} (eV) ref.
C	6.42	H: through C	2.00	7.63[19], 7.15[20], 6.50[23] , 4.91[40] ,6.09[41]
O	6.75	H: through O	2.03	6.97[19],6.81[20], 6.94[23] , 4.82[40], 5.19[41]
H	3.73	H: through H	1.76	3.74[19],3.70[20], 3.77[23], 2.46[40], 2.72[41]
CO	1.06	H: through C	2.01	1.06[19],1.15[20], 1.09[23], 0.86[40], 1.28[41]
COH	1.82	B: through C	1.97/2.48	2.01[19],2.28[20], 1.99[23], 2.11[41]
CHO	3.65	T: through C	1.99	3.81[19],3.53[20], 3.77[23], 3.67[41]

Note: [19] Cu (100); [20] Cu (110); [23] Cu (111); [40] Cu (111); [41] Cu (211) surface. H: the hcp site, B: the bridge site and T: the top site.

Table 1.5 The elementary reactions of CH_XO (x=2,3) and methanol formation.

Reaction	E_a, eV	ΔE, eV
$CHO+H \rightarrow CH_2O$	0.51[19],0.24[20], 0.47[22],0.51[23], 0.71[41], 0.58[42], 0.88[42]	-0.41[19],-0.51[20],-0.40[22],-0.23[23],-0.20[41], -0.21[42], -0.18[42]
$CH_2O+H \rightarrow CH_3O$	0.29[19],0.38[20],0.24[22],0.36[23],0.71[41], 0.13[42], 0.11[42]	0.80[19],-0.73[20],-1.02[22],-0.91[23],-0.78[41], -0.91[42], -1.24[42]
$CH_3O+H \rightarrow CH_3OH$	0.89[19],0.65[20],1.17[22],1.20[23],1.07[41], 0.91[42], 1.11[42]	-0.04[19],-0.02[20],-0.23[22],0.16[23],0.07[41], 0.10[42], 0.34[42]

Note: the surface model adopted in the elementary reaction. [19] Cu (100), [20] Cu (110), [22] Cu (111),[23] Cu (111), [41] Cu (211), [42] Cu (211) and CuZn (221).

Table 1.6 Activation energy and reaction energy for each elementary reaction on K_2O/Cu(111) surface.

Reaction no.	Elementary reaction	f/i cm^{-1}	Without ZPE correction, eV		With ZPE correction, eV		Reference, eV	
			E_a	ΔE	E_a	ΔE	E_a	ΔE
TS 3-12	CH + CO → CHCO	178.22	0.66	-0.80	0.65	-0.72		
TS 3-13	CH_2 + CO → CH_2CO	106.41	1.78	-0.72	1.67	-0.64	0.46[20], 1.09-1.65[12]	-0.34[20], -0.16-0.62[12]
TS 3-14	CH_3 + CO → CH_3CO	134.67	1.43	-0.41	1.24	-0.31	1.01[19],1.01[19], 1.07[20],1.46[41]	-0.21[19],-0.15[19], -0.08[20], 0.03[41],
TS 3-15	CHO + CH → CHOCH	60.88	0.01	-1.40	0.05	-1.31	1.04[5]a,0.85[5]b	-1.45[5]a,-1.72[5]b
TS 3-16	CHO + CH_2 →$CHOCH_2$	130.93	1.08	-1.91	1.00	-1.75	0.40[20]	-1.66[20]
TS 3-17	CHO + CH_3 → $CHOCH_3$	752.98	1.74	-1.08	1.23	-0.94	0.54[19],0.51[19], 0.58[20],0.91[41]	-1.00[19],-1.04[19], -0.84[20],-0.79[41]
TS 3-18	CHO + CO → CHOCO	40.59	0.39	0.23	0.40	0.28	0.41[5]a,0.23[5]b	0.23[5]a,0.23[5]b
TS 3-19	CH_2O + CH_2 → CH_2OCH_2	197.76	0.41	-0.61	0.36	-0.50		
TS 3-20	CH_2O + CO → CH_2OCO	602.89	1.09	0.90	0.93	0.86		
TS 3-21	CH2O + CHO → CH_2OCHO	339.07	0.46	-0.23	0.43	-0.19		

Note:[5]a. CuZn (111), b.Cs_2O-CuZn (111); [12] MoS_2; [19]: Cu (100) and Cu (111) ; [20]: Cu (110); [41]: Cu (211).

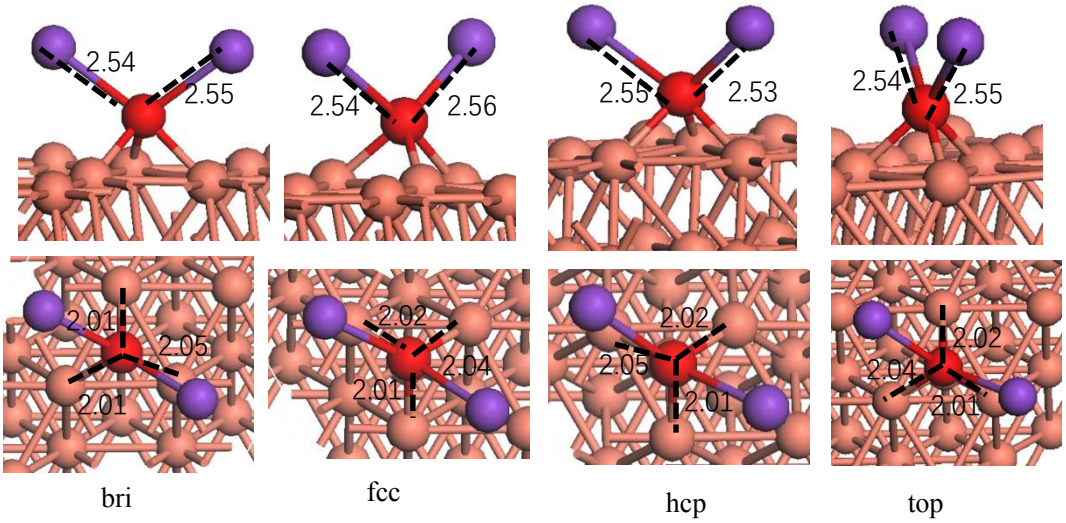

Fig.1.1 The optimized adsorption configurations of K_2O on Cu (111) surface.

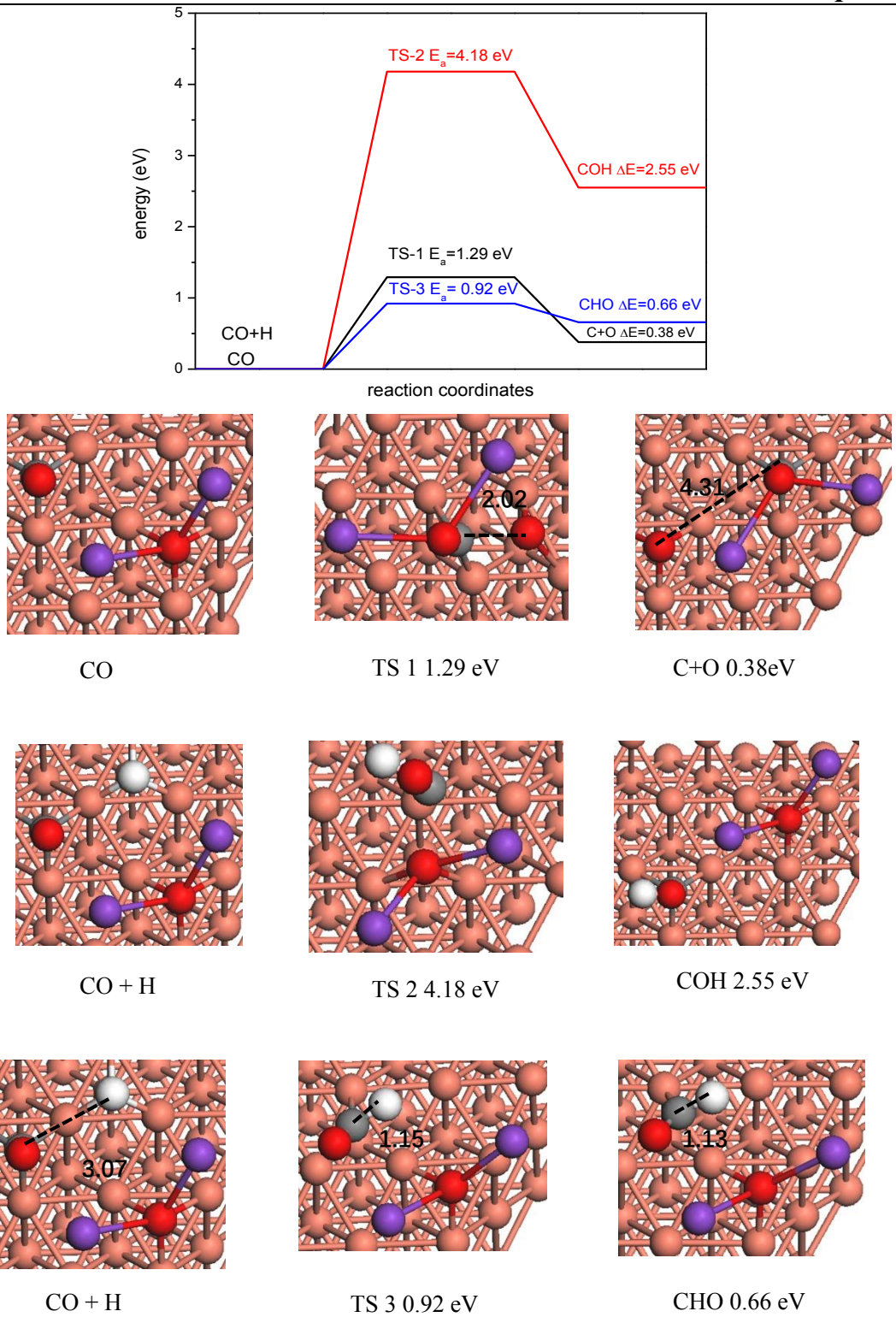

Fig. 1. 2 The the initial states, transition states and final states for the direct dissociation and H-assisted dissociation of CO on K_2O/Cu (111) surface.

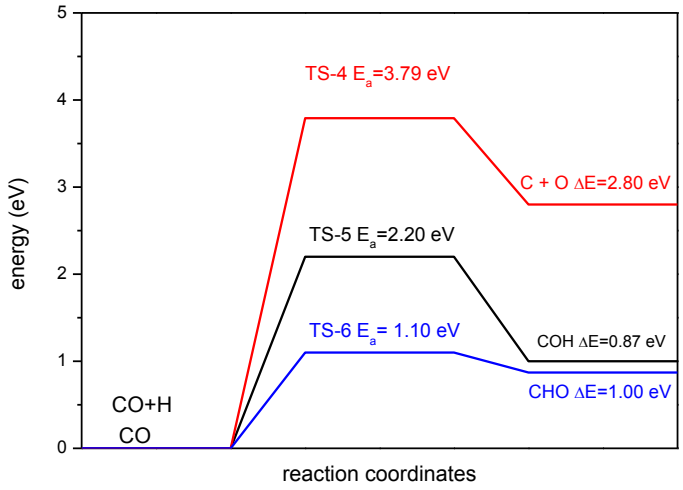

Fig. 1.3 The direct dissociation and H-assisted dissociation routes of CO on Cu(111) surface.

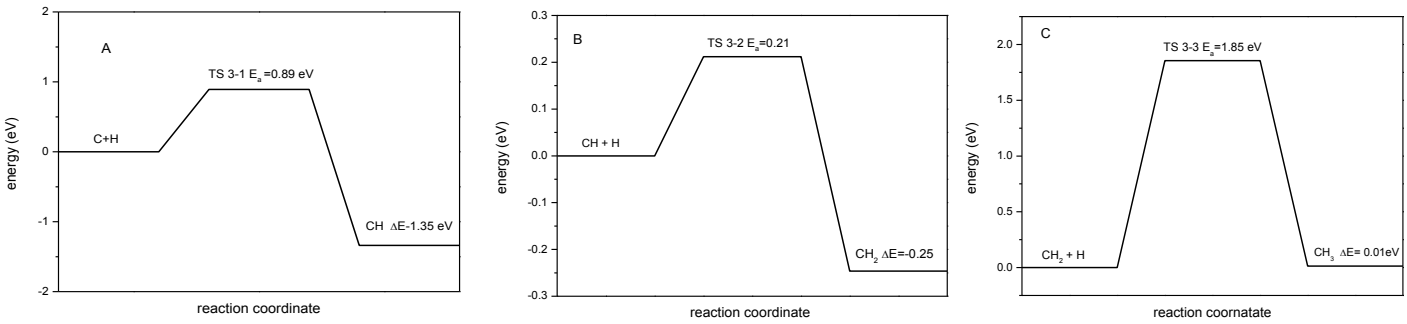

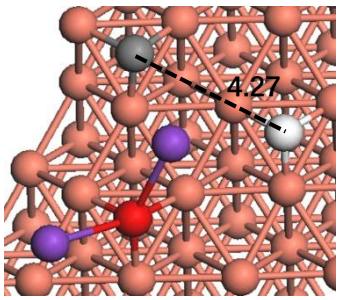

C+H

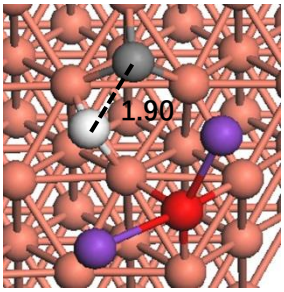

TS 3-1 0.89 eV

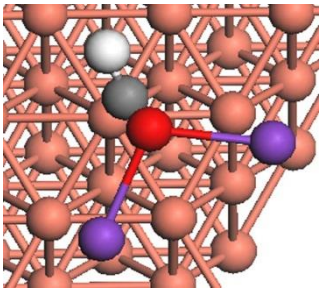

CH -1.35 eV

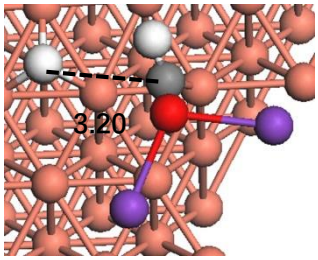

CH+H

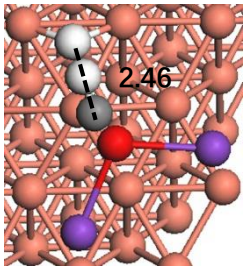

TS 3-2 0.21 eV

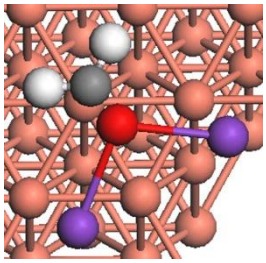

CH+H -0.25 eV

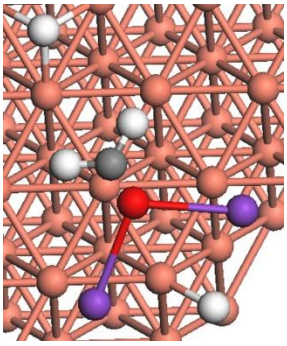

CH_2+H

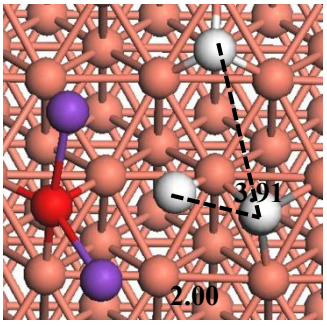

TS 3-3 1.85 eV

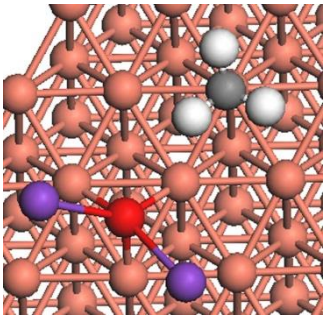

CH_3 0.01 eV

Fig. 1.4. The initial states, transition states and final states for CH, CH_2, and CH_3 formation by CO direct dissociation on K_2O/Cu(111) surface.

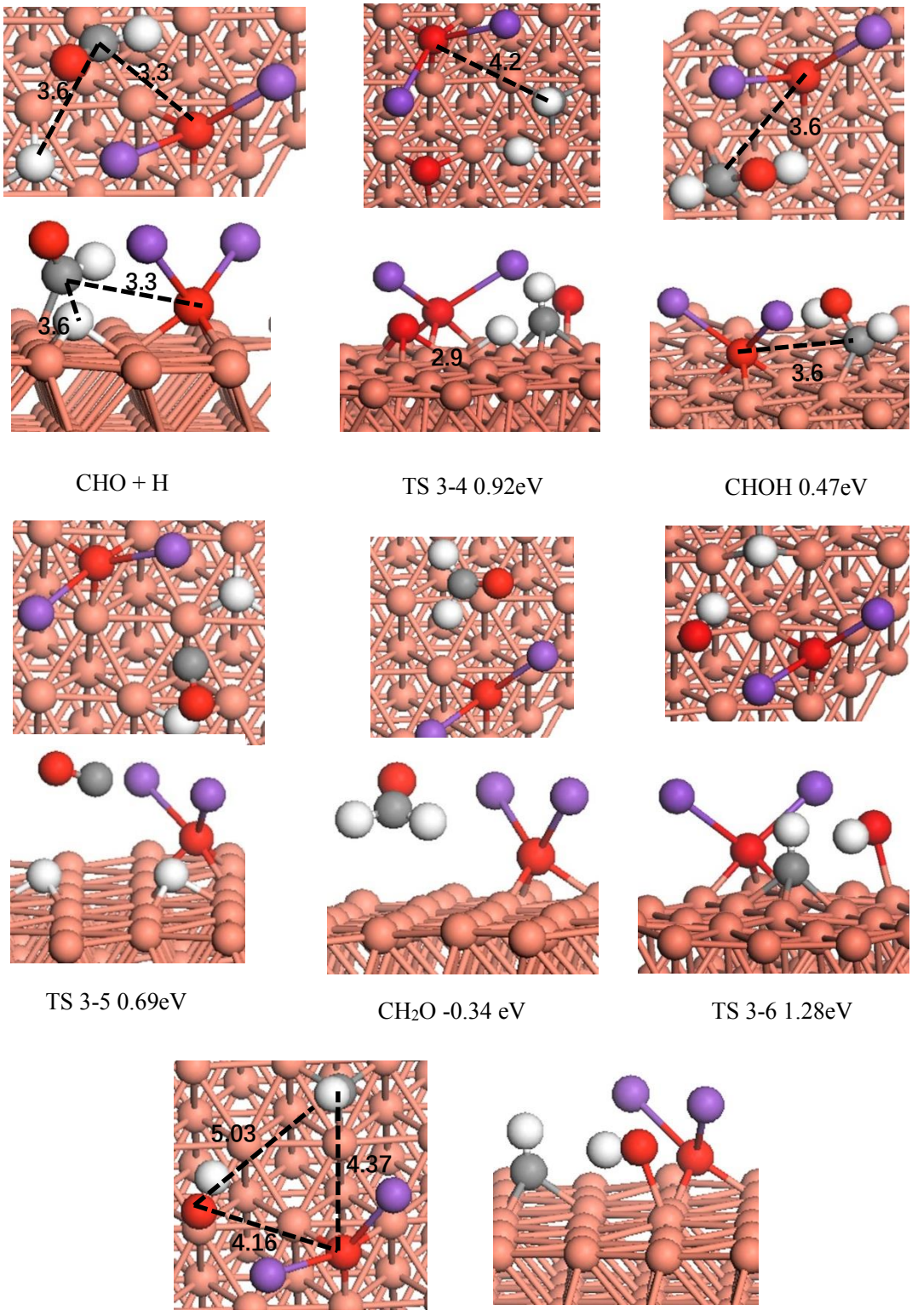

Fig. 1.5. The top and side views of initial states, transition states and final states of CH formation through CHO hydrogenation.

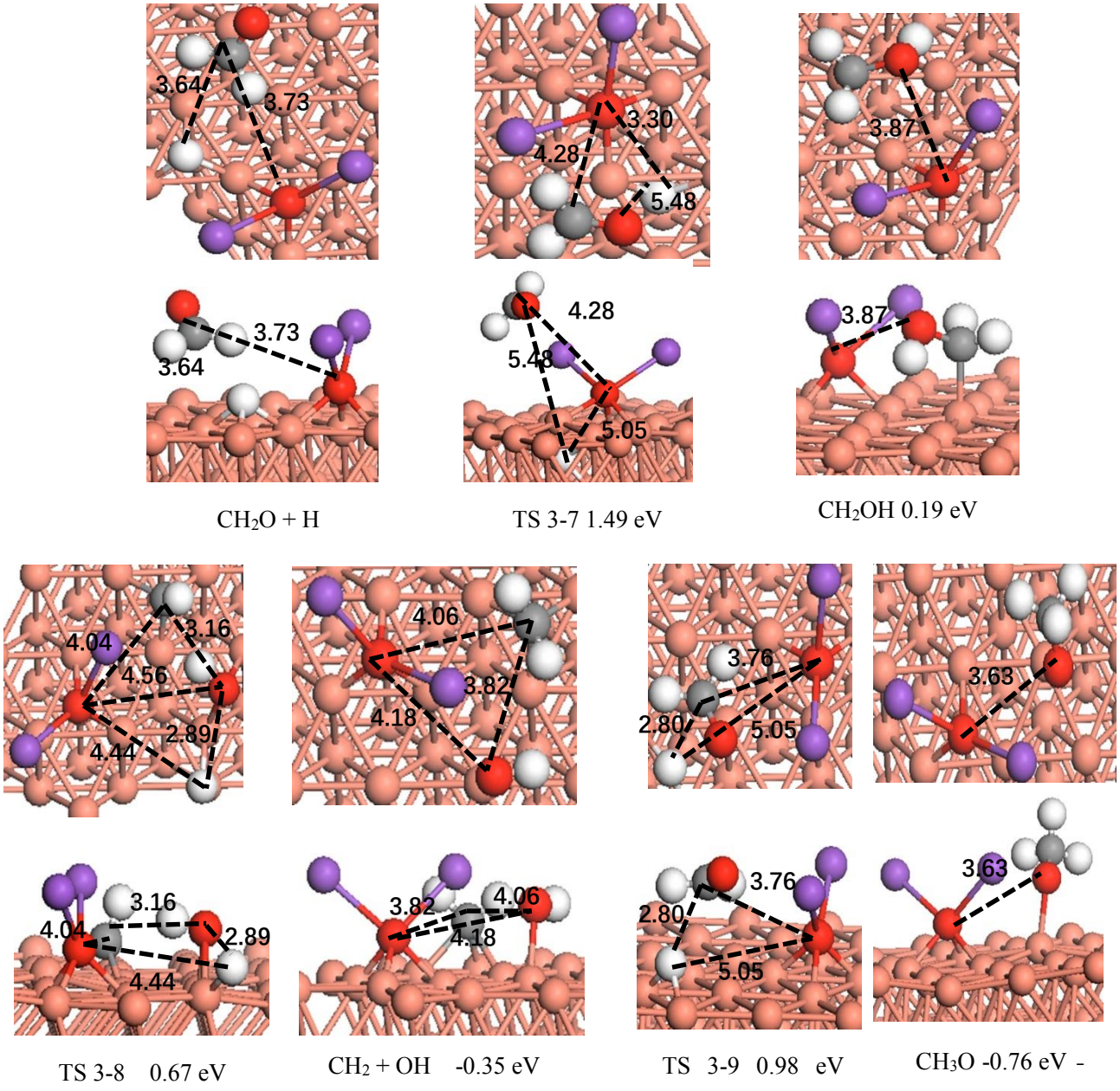

Fig. 1 .6. The initial states, transition states and final states of CH_2O hydrogenation on K_2O/Cu (111) surface.

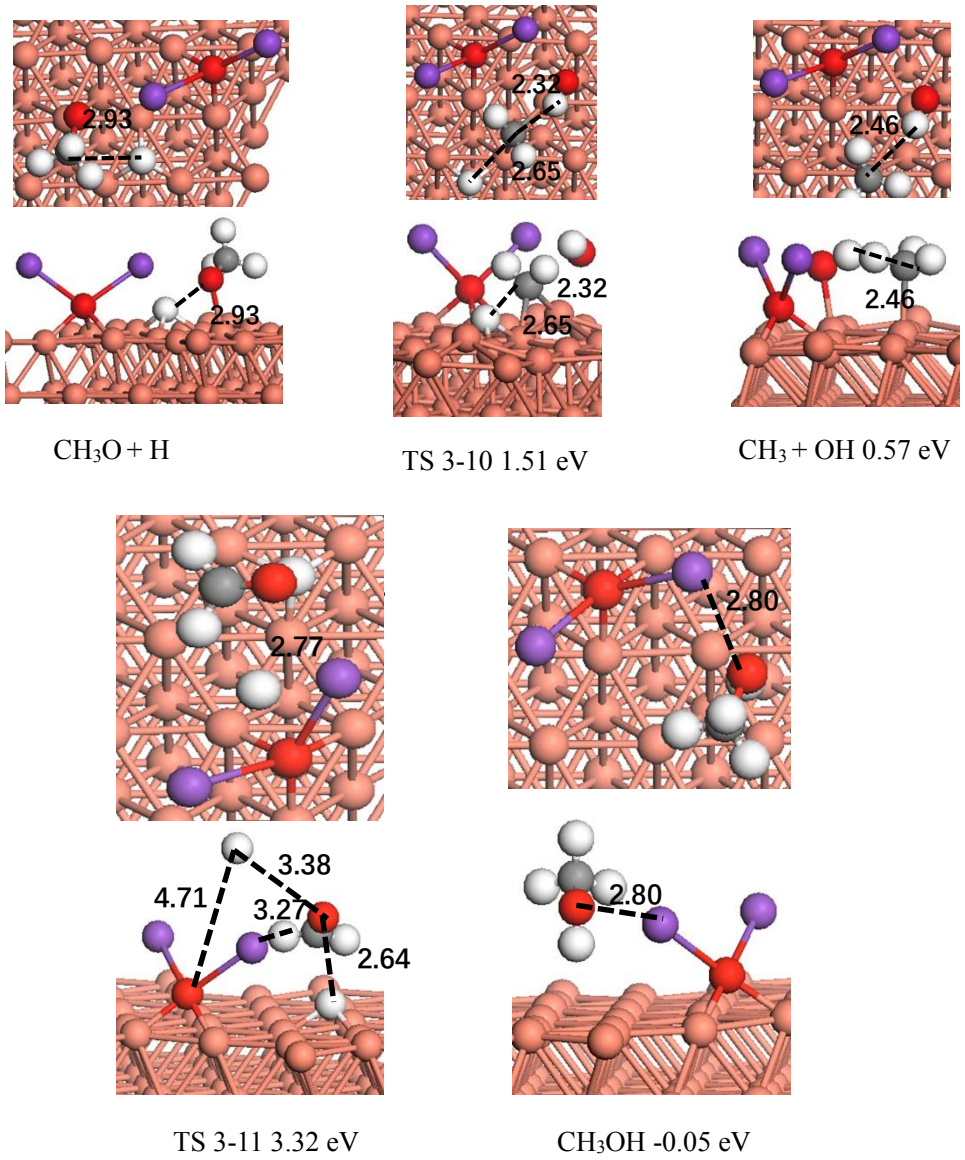

Fig. 1. 7. The top and side views of initial states, transition states and final states of hydrogenation of CH_3O on K_2O/Cu (111) surface.

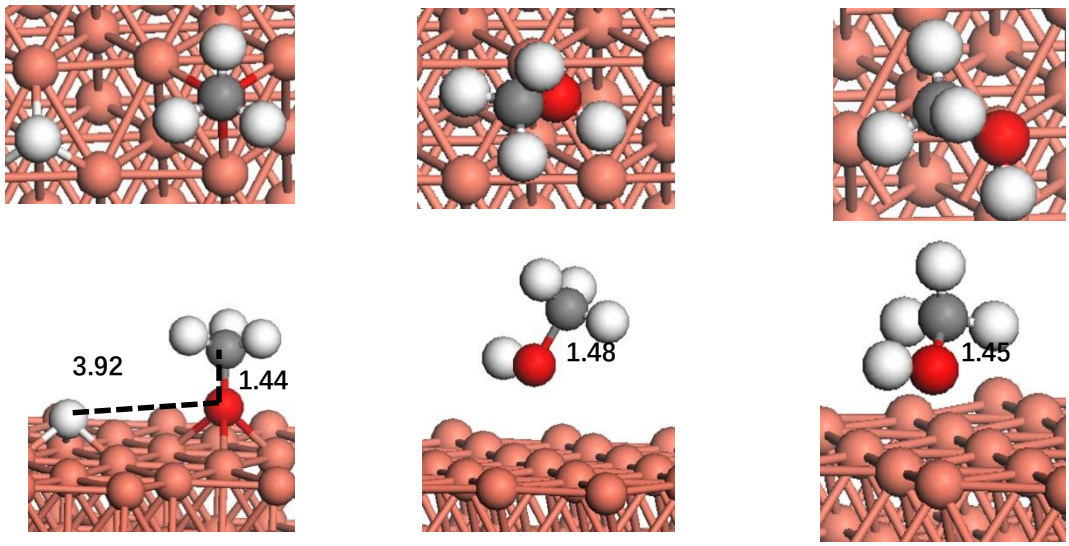

CH_3O + H TS 1.43 eV CH_3OH 0.19 eV

Fig. 1. 8. The top and side views of initial states, transition states and final states of CH_3O hydrogenation into CH_3OH on Cu (111) surface.

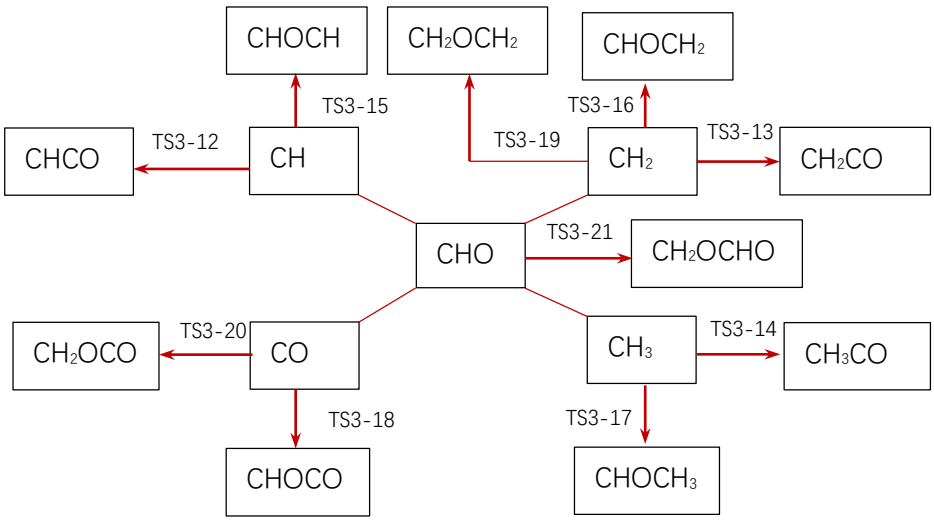

Fig. 1.9 The possible C_2 oxygenates formation routes between CHO, CHx and CO on K_2O/Cu (111) surface.

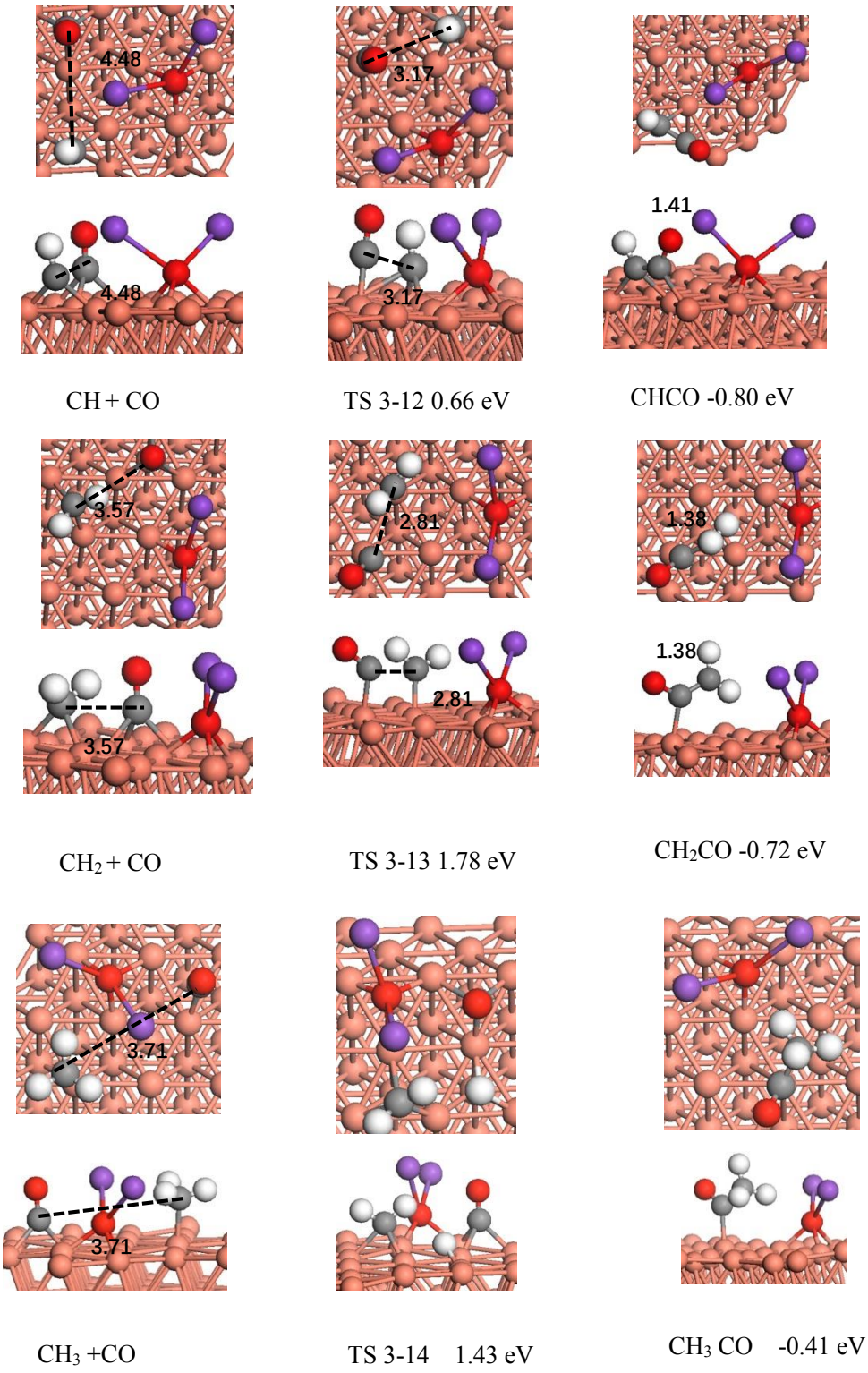

Fig. 1. 10. The top and side views of initial states, transition states and final states of hydrogenation for C_2 oxygenates formation starting from CH_x(x=1,2 and 3) and CO on K_2O/Cu (111) surface.

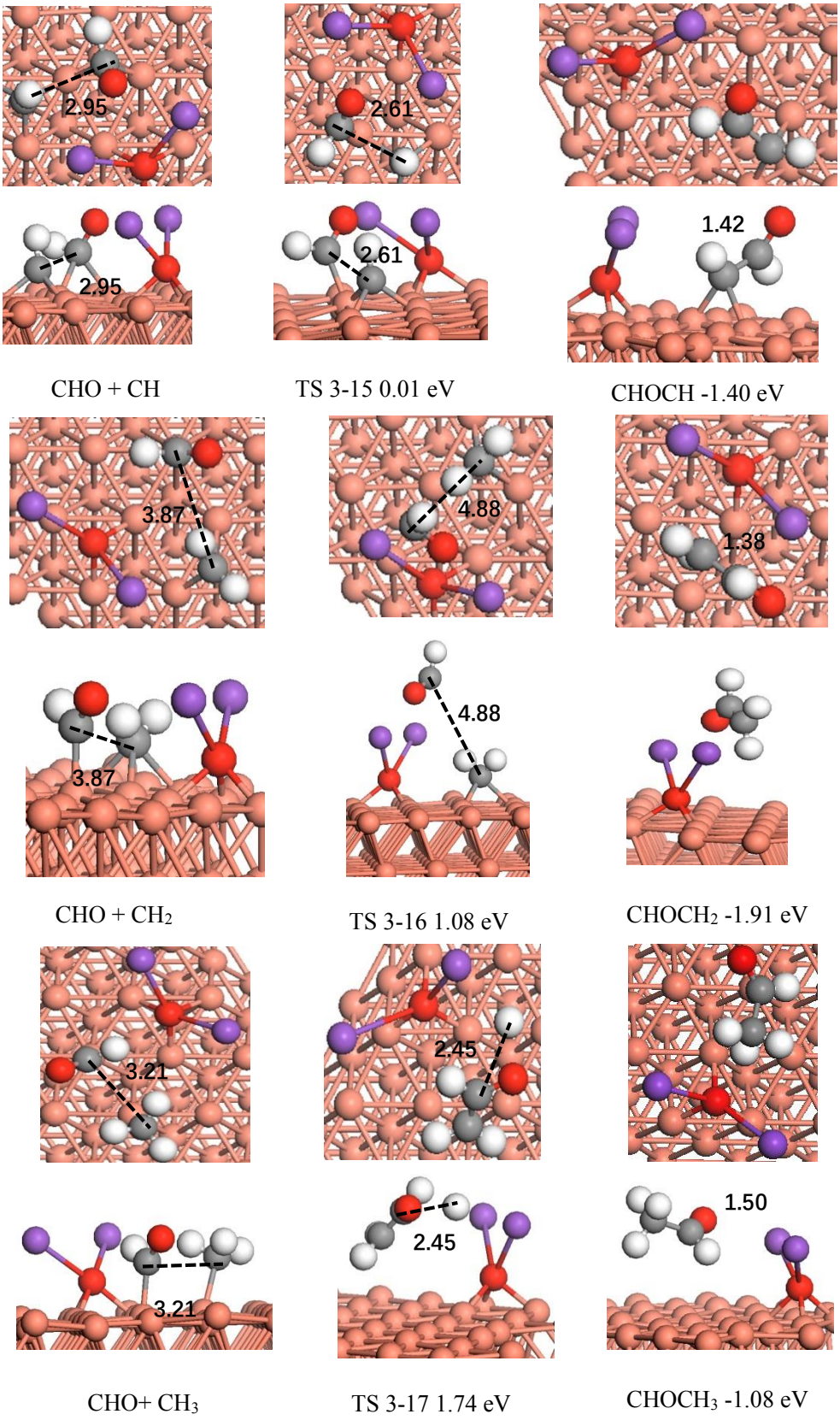

Fig. 1. 11. The top and side views of initial states, transition states and final states of C_2 oxygenates formation beginning from the interactions between CHO and CH_x (x=1,2 and 3) on K_2O/Cu (111) surface.

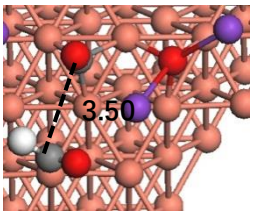

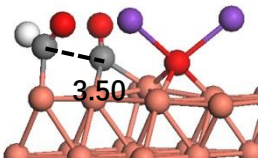

CHO + CO

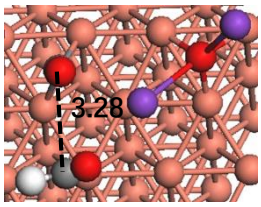

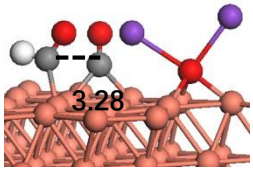

TS 3-18 0.39 eV

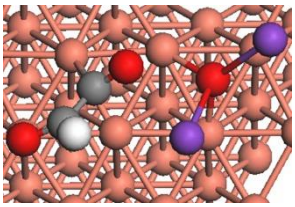

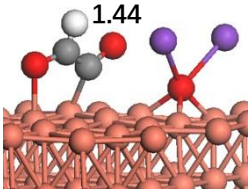

CHOCO 0.23eV

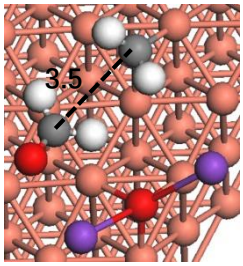

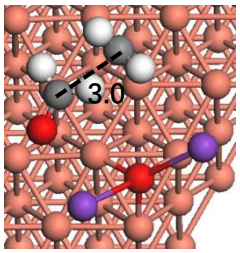

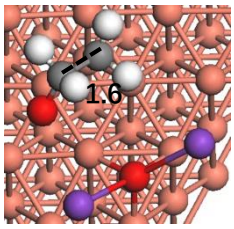

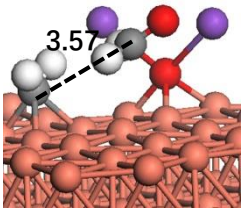

$CH_2 + CH_2O$

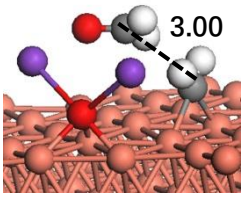

TS 3-19 0.41 eV

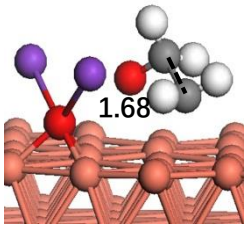

CH_2CH_2O -0.61eV

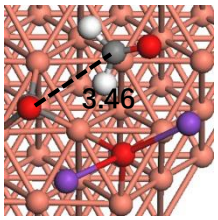

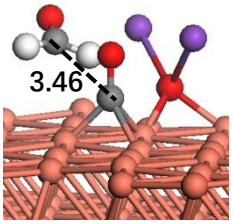

CH_2O+CO

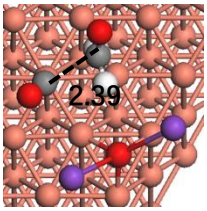

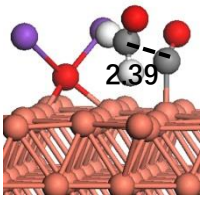

TS 3-20 1.09 eV

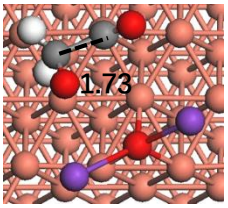

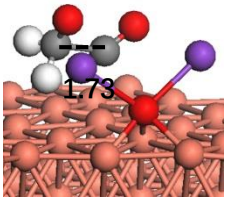

CH_2OCO0.90 eV

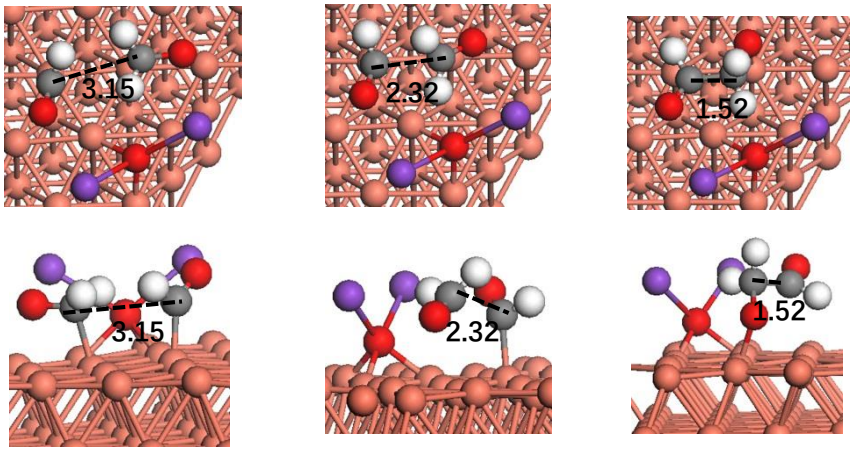

CH_2O+CHO TS 3-21 0.46 eV CH_2OCHO -0.24 eV

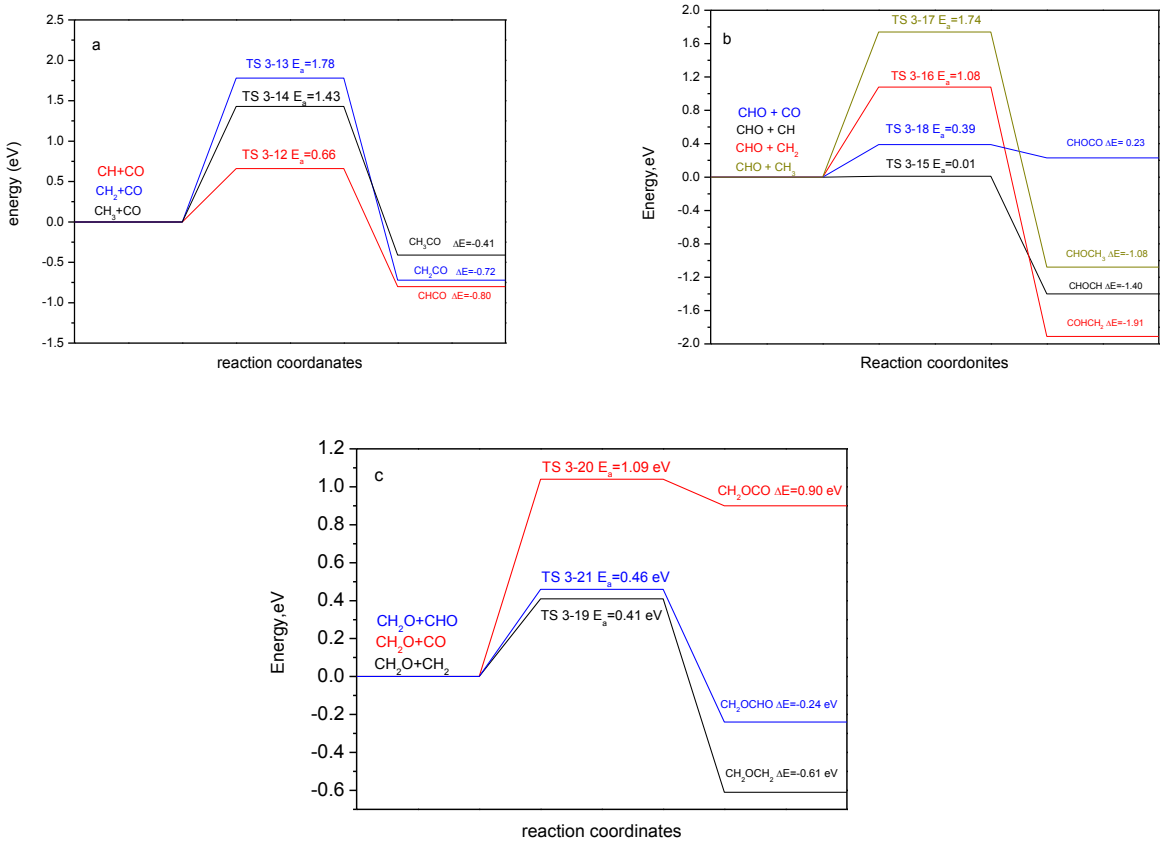

Fig. 1. 12. The reaction coordinates and top and side views of initial states, transition states and final states for C_2 oxygenates formation starting from the interaction between CO, CHO, CH_2O and CH_2 on K_2O/Cu (111) surface.

Chapter 2

Effects of surface hydroxyl groups induced by the co-precipitation temperature on the catalytic performance of direct synthesis of isobutanol from syngas

Higher CO conversion and selectivity of alcohol and isobutanol on ZC-60 catalyst was induced by the high concentration of surface OH. Formate is more easily formed than carbonates by CO reacted with surface OH, which initiates the growth of carbon chain and formation isobutanol.

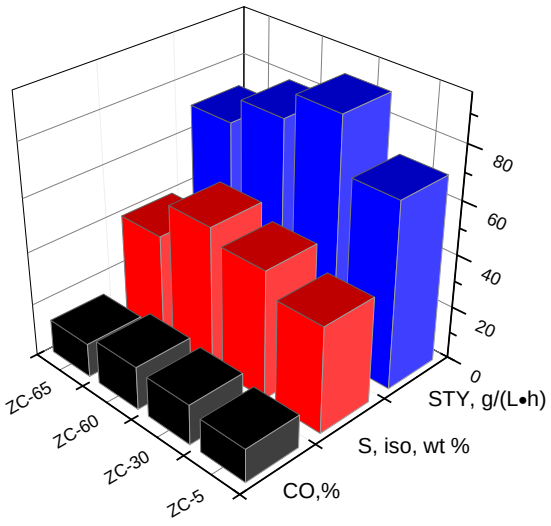

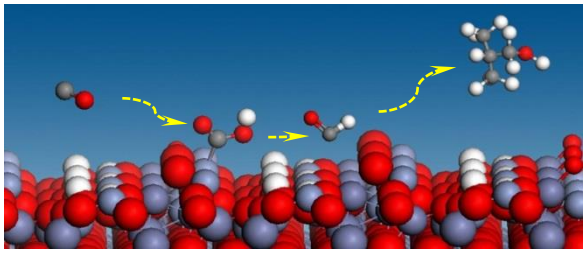

Abstract

A series of Zn-Cr oxides catalysts with different content of surface hydroxyl groups were prepared at different co-precipitation temperature. These catalysts were used for direct synthesis of isobutanol from syngas with an aim to investigate the effect of co-precipitation temperature on the catalytic activity of Zn-Cr catalysts. The co-precipitation temperature had a strong influence on surface OH groups leading to the different activities of ZnCr catalysts. Catalysts characterizations by XPS, XRD, H_2-TPR, CO_2-TPD, in situ FTIR of CO absorption and DFT calculation clearly revealed that the surface OH groups played important role in the absorption and activation of CO. The absorption energy of CO is intensified by the presence of surface OH, and it is easier to form formats than carbonates owning to the low activation barrier and reaction energy. Therefore, selectivity for alcohols showed an increased tendency with increasing the surface OH content on catalysts. Among all ZnCr catalysts, catalyst prepared at 60 ^{o}C (ZC-60) showed the best catalytic performance due to the highest concentration of surface OH groups.

Keywords: ZnCr catalyst, surface hydroxyl, isobutanol synthesis, DFT calculation

2.1 Introduction

Isobutanol attract considerable interest owing to its wide range of applications. In petroleum and fuel, isobutanol was employed as feedstocks to produce methyl tert-butyl ether (MTBE) or directly added into gasoline to elevate the octane number of motor fuel. It can be also used as raw materials to produce plasticizer, antioxidant, muskone, medicine or employed as solvent to purify rare earth metals [1, 2]. The rapid increase on isobutanol consumption requires more effective production approaches. Isobutanol synthesized from syngas can be realized effectively on ZnCr based catalysts, and ZnCr mixed oxides modified by K and Cs, have been widely studied due to their good stability, high isobutanol selectivity and acceptable CO conversion [3, 4]. For Cs modified ZnCr catalysts the composition of alcohol was slightly complex. Except methanol and isobutanol, other higher alcohols also presented. While for K modified ZnCr catalysts, the alcohols was mainly composed of methanol and isobutanol, and the selectivity of two alcohols is larger than 94%, which will simplify the separation process in isobutanol synthesis. Additionally, the simplification products are also the motivation for understanding the total catalytic process and the active sites of catalysts. To reveal the true active sites on K_2O/ZnCr catalyst, a lot of characterization were performed for the bulk, reduced and used catalysts. The isobutanol synthesis reaction from syngas on K promoted ZnCr catalyst had been characterized by X-ray diffraction, infrared spectroscopy and electron spin resonance spectroscopy, and analysis results shown that the active species is a non-stoichiometric spinel-like phase $Zn_xCr_{2/3(1-x)}O$ [5, 6]. In this non-stoichiometric structure, Zn^{2+} ions occupy not only the tetrahedral sites but also the

octahedral sites randomly distributed with Cr^{3+} ions [5, 6]. Rietveld method was used to analyze the XRD patterns of a series of ZnCr oxides catalyst that has different degrees on cation disorder distribution obtained by varied co-precipitation and post-calcinated method, the analysis results demonstrated that the productivity of isobutanol exhibits an approximately linear relationship with the level of cation disorder distribution [7]. The absorbed oxygenates and surface hydroxyl species on the catalyst surface caused by cation disorder distribution facilitates the formation of the significant intermediate species for alcohol synthesis from syngas [1,8,9]. However, the effect of surface oxygenates on the activation of CO, and distributions of products are still not clear. To study these problems, a series of catalysts with different concentration of surface hydroxyl and absorbed oxygenates were prepared by co-precipitation method and characterized by surface analysis, activity evaluation and DFT calculation to discover the actual effects of surface hydroxyl.

2.2 Experimental section

2.2.1 Catalysts preparation

The Zn-Cr mixed oxides catalysts were prepared by a typical co-precipitation procedure. Appropriate amounts of $Zn(NO_3)_2 \cdot 6H_2O$ mixed with $Cr(NO_3)_3 \cdot 9H_2O$ (the Zn to Cr atomic ratio is 1.0) and ammonium carbonate were dissolved in 500 mL of deionized water, separately. Then the two kinds of solution were pumped together in a well-stirred thermostated flask with three necks by peristaltic pumps at pH of 9

maintained at a certain temperature. Next, the dark blue suspension was aged for 2 h at the co-precipitation temperature, followed by filtering, washing thoroughly with deionized water at the same temperature, and drying at 100 ^{o}C overnight. The dried samples were labeled as ZnCr(OH)x-y, where x presents the contration of OH groups, y presents the co-precipition temterature, which equals to 5, 30, 60 and 95 respectively. The obtained ZnCr(OH)x-y samples were milled into powders and calcinated at 400 ^{o}C for 6 h to remove the residual carbonates, moisture etc. Then the samples were milled into powders and impregnated with 3.0 wt% K_2O as a promoter (from potassium carbonate) through an incipient wetness method. Finally, the samples were dried at 100 ^{o}C for 12 h and calcinated at 400 ^{o}C for 6 h to get the ZnCr catalysts. The catalysts were labeled as ZC-5, ZC-30, ZC-60 and ZC-95, where 5, 30, 60 and 95 stood for the co-precipitation temperature of 5, 30, 60 and 95 oC, respectively.

2.2.2 Catalysts characterization

The X-ray diffraction (XRD) data of the samples were recorded using a D8 Advance X-ray diffractometer in the 2θ range from 5^{o} to 80^{o} with Cu radiation. The scanning was taken with a 2θ step size of 4^{o} every minute.

The XPS patterns were recorded using an AXIS ULTRA DLD X-ray photoelectron spectrometer equipped with a multichannel detector. Charge referencing was done against adventitious carbon (C 1s, 284.8 eV). A Shirley-type background was subtracted from signals. The recorded spectra were fitted using Gauss-Lorentz curves to determine the surface composition of different samples.

IR spectra of CO adsorption and desorption were obtained using a TENSOR-27 spectrometer equipped with a liquid nitrogen cool MCT (Mercury-Cadmium-Telluride) detector in the range from 4000 to 600 cm^{-1} with 4 cm^{-1} resolution. The ultrahigh purity (>99.999%) gases of H_2, CO and Ar were used. A certain amount of well milled catalyst was mounted into the in situ IR sell with KBr window**.** Before CO adsorption, all of the catalysts were reduced with pure hydrogen for 2.0 h at 400 ^oC online. CO adsorption was taken at 50 ^oC and 400 ^oC after flowing for 0.5 h by pure Ar at the same temperature, and the adsorbents on the surface of Zn-Cr based catalysts were then measured.

The temperature desorption of CO_2 was recorded on TP-5050 automatic chemical adsorption instrument in the range of 323 K to 873 K. The catalysts were saturated with CO_2 at 323 K for 0.5 h after pre-reduced in the gas that contains 10% H_2 in Ar. Then pure Ar flowed for 2 h at the same temperature to eliminate the physically adsorbed water and contaminates. Finally, the temperature was increased with the rate of 5 $^oC/min^{-1}$ under Ar flow. The desorbed species were analyzed on GC 4000A by thermal conductivity measurements.

Nitrogen adsorption-desorption isotherms were carried out at 77 K using a Micromeritics ASAP 2020 analyzer. Before absorption, the samples were out-gassed at 623 K for 10 h. The specific surface area (S_{BET}) was calculated according the Barrett-Joyner-Halenda (BJH) formula applied to the desorption branch.

The bulk composition of Zn and Cr were determined by inductive coupling plasma optical emission spectrophotometry (ICP-AES) using a Varian analyzer. About 0.010 g of the catalyst was dissolved in a mixture of hydrochloric and nitric acid solutions for

digestion then diluted in a 1 wt% of nitric acid solution to determine the metal content.

2.2.3 Catalysts catalytic performance evaluation

Each of these catalysts was on line reduced with a 10% hydrogen-in-nitrogen mixture for 4 h at 400 ^{o}C. Then, these catalysts were tested for isobutanol synthesis in a fixed bed reactor using a feed gas of H_2 : CO mixture (2.6 : 1) at a space velocity of 3000 h^{-1}. The reactions were performed at temperature 400 ^{o}C and pressure 10.0 MPa. The products were analyzed by four online GCs. Inorganic gas products, like CO, H_2, H_2O and CO_2, were detected online equipped with a thermal conductivity detector using a GC 4000A (carbon molecular sieves column). The organic gas products containing hydrocarbons and methanol were detected online by a fame ionization detector using a GC 4000A (GDX-403 column). The alcohol products in liquid phase were analyzed by a fame ionization detector using a GC-7AG (Chromsorb101). The H_2O and methanol products in liquid phase were detected by thermal conductivity detector using a GC 4000A (GDX-401 column).

2.2.4 Computational Methods

All DFT calculations were performed using the Vienna ab initio simulations package (VASP) [10-12]. For the adsorption of CO, an ultrasoft pseudopotentialis was employed for all the ion electron interaction [13-15]. The exchange-correlation interaction for $ZnCr_2O_4$ model catalyst is treated with the local density approximation from the Ceperley-Alder scheme parameterized by Perdew and Zunger [16, 17]. For the absorption and reaction of formate and carbonate on non-stoichiometric spinel,

GGA-PBE functional was employed. The electron-ion interaction was described by PAW method. For all the calculation, kinetic cutoff energy for a plane wave basis set is 350 eV. All the structures were optimized until the maximum force on each atom was lower than 0.05eV $Å^{-1}$. The Brillouim zone sampled using 1×1×1 Gamma points only with Methfessel-Pack smearing of 0.2 eV.

Among all the low-index $ZnCr_2O_4$ surfaces, the (111) surface was modeled using a 2×2 supercell with dimensions of 11.44440 Å × 11.44560 Å × 28.93950 Å. Sixteen $ZnCr_2O_4$ molecular units in each slab were distributed in twelve layers. The vacuum regions separating the slabs were all set to the widths of 15 Å, this distance is enough to screen the self-interaction effects of the periodic boundary conditions. On $ZnCr_2O_4$ (111) surface, atoms in the three topmost layers were allowed to relax, the rest of the layers at the bottom were fixed to mimic the bulk effects. Surface of non-stoichiometric spinel (non-spinel) was constructed by exchange Zn and Cr on the surface of $ZnCr_2O_4$ (111) surface, the OH groups on the surface of non-stoichiometric (non-spinel-OH_3) was modeled by saturation oxygenate vacancies. The detailed process to construct the surface of non-stoichiometric and OH saturated surface were shown in the subsequent section of DFT calculation.

Reaction paths have been studied using climbing-image nudged elasic band method (CI-NEB). The transition state structure is deemed to converge when the force acting on the atoms are all less than 0.05 eV/Å for the various degrees of freedom set in the calculation. Transition states were confirmed by vibrational analysis yielding one imaginary frequency.

The binding energies of the adsorbed CO is defined as $E^{CO}_{ad}=E_{sur/CO}-E_{sur}-E_{CO.}$ The E_{sur} is the total energy of the slab of the surface; the E_{CO} is the total energy of free CO; $E_{sur/CO}$ is the total energy of the slab with the adsorbed CO molecule on the surface. The above equation means that a negative E^{CO}_{ad} value will lead to an exothermic adsorption reaction.

For the formation of formate and carbonate on non-spinel-OH_3, the reaction energy (Δ E) and activation energy (E_a) are calculated on the basis of the following equation:

$$\Delta E= E_{pro} - E_{rea}$$

$$E_a=E_{ts}–E_{rea}$$

where the E_{pro} is the energy of for adsorbed formate or carbonates; E_{rea} is the energy of absorbed CO on non-spinel-OH_3, and E_{ts} is the total energy of transition state on non-spinel OH_3 surface.

2.3 Results and discussion

2.3.1 The structure of ZnCr(OH)x-y and their thermal decomposition behavior

The XRD patterns of ZnCr(OH)x-y samples are shown in Fig.2.1 A. As shown, the remarkable diffractions located at 34.44 and 60.32 are the charactritic diifreaction peaks of the layered double hydroxide (LDH) (006) and (113) surfaces [18,19]. The difractions located at 12.96 for ZnCr(OH)x-95 may be caused by the formation of Cr(OH)x species. One can see an interesting phonmnen in the XRD patterns is the

intensified diffraction of Cr(OH)x species, which indicate that the exit forms of Zn and Cr can be altered by controlling the co-precipitation temperature. According to the investigation performed by Chen Z et al. [19], ZnCr-LDH is an important prossors to form $ZnCr_2O_4$. The different interaction between ZnCr-LDH and Cr(OH)x will induce different ZnCr oxide with different surface properties.

To further explore the thermal decomposition behavior, TG-DSC curves for all the processor samples are recorded. As can be see in Fig. 2.1 B, the ΔH during ZnCr(OH)x-y decomposition gives different strength for ZnCr(OH)x-5, ZnCr(OH)x-30 and ZnCr(OH)x-60 and ZnCr(OH)x-95 according to DSC curves, indicating the different interaction between the four samples. However, when further investagete the thermal decomposition of these samples by IR analysis (Fig. 2.1 C), one can see that there are no remarble different absorption for the sample both at 30 ^oC and 400 ^oC for 30 min. The only differene presented in the IR is the absorption in the range of 3000-3500 cm^{-1} which is denoted to the vibration of OH. IR characrizition show that the different amount of OH groups created for the different processors. To further investigate the ZnCr-x catalyst samples the detailed investigation was performed and listed in the following section.

2.3.2 The BET surface areas of the catalysts

The S_{BET} of the samples are 84.88, 62.90, 112.44 and 100.38 m^2/g for ZC-5, ZC-30, ZC-60 and ZC-95, respectively. The results showed that surface areas of ZnCr

catalysts were improved by increasing the co-precipitation temperature, which may be caused by the treatment of water solution of ammonium carbonate under higher temperature. Though the ZnCr catalyst with higher surface areas would be expected higher efficiency of alcohol synthesis, water gas shift reaction was also intensified under the reaction conditions. The competition between the two reactions would not be resulted in high catalyst efficiency.

2.3.3 Characterization of the catalysts using powder X-ray diffraction

The powder X-ray diffraction (XRD) patterns of the ZnCr catalysts are shown in Fig. 2. 2. In Fig. 2. 2 A, all the samples present the diffraction peaks for layered double hydroxides, no remarkable difference was observed for all the samples. These results suggest that the difference between the processors is very small. In Fig. 2. 2. A, no diffraction peaks for K_2O, K_2CO_3, K_2CrO_4, $K_2Cr_2O_7$ and Cr_2O_3 species were found in any of the XRD patterns. The main reflections were in consistent with crystalline ZnO and $Zn_xCr_{2/3(1-x)}O$ [5, 24-27]. With co-precipitation temperature increased from 5^oC to 95 ^oC, no changes were found in the diffraction position of two zinc species, whereas the intensity of these species was changed. For ZC-5, ZC-30 and ZC-60, a typical peak at 31^o indexed to ZnO was observed**.** The intensity of the peak decreased gradually in the order of : ZC-95 < ZC-30 < ZC-5 < ZC-60, indicating the morphology of ZnO was affected by the co-precipitation temperature. For all the spent catalysts (Fig. 2. 2 B), the intensity of ZnO became stronger than the fresh one, owning to the aggregation of ZnO during reaction. The morphology change of ZnO could effluence the interaction

between ZnO and $Zn_xCr_{2/3(1-x)}O$, and modifying the efficiency of the catalyst, which was further confirmed by subsequent analysis**.**

2.3.4 Characterization of the catalyst using X-ray photoelectron spectra

The X-ray photoelectron spectra of the samples are shown in Fig. 2.3 and Fig. 2.4. The feature caused by Cr and Zn were all presented. The Cr 2p peaks (Fig. 2.3) at 576.43 eV and 585.76 eV of Cr^{3+} and 579.45 eV of Cr^{6+} were remarkable [7, 8, 20, 21]. The XPS spectrum of Zn 2p peaks presented at 1021.20 eV and 1044.00 eV were shown in Fig. 2.4 [7, 8, 20, 21]. The position and intensity of these peaks were almost the same for all the samples with the co-precipitation temperature from 5 ºC to 95ºC. The Zn to Cr atomic ratios of the bulk and on the surface of the catalysts are shown in Table 2.1. For the bulk catalysts, the atomic rations were close to 1.0 in which were consistent with the recipe ratio for catalysts preparation. However, on the surface of catalysts, the atomic ratios were in a range of 0.741 to 0.836, which were smaller than the ratios of bulk catalysts. The observations were consistent with the former research results of our group [7, 9]. The lower atomic ratios of Zn to Cr on the surface of the catalyst was caused by the formation of non-stoichiometric spinel structure by the extra zinc cations entering the bulk catalyst.

2.3.5 O-XPS analysis of ZnCr catalysts

XPS spectra of O 1s of ZnCr catalysts were shown in Fig. 2.5. Two oxygen signals located at 529.60 and 531.0 eV were attributed to the lattice oxygen O_{latt} and the surface absorbed oxygen O_{ads}, respectively [1, 8].The $O_{ads}/(O_{latt} + O_{ads})$ molar ratio for the

catalysts was determined by quantitative calculation of the corresponding peaks areas and the results were shown in Table 2.2. The $O_{ads}/(O_{latt} + O_{ads})$ ratios increased with the co-precipitation temperature increased from 5 ºC to 95 ºC. The maximum value is 41% for ZC-60, which was much higher than ZC-5 and ZC-30 but close to ZC-95. The higher ratio of $O_{ads}/(O_{latt} + O_{ads})$ meant higher number of dangling bonds to stabilize the surface of spinel with disordered cations, indicating higher amount of active sites on the prepared catalysts [9]. The results of in situ CO infrared analysis described below suggested that the surface hydroxyl species played an important role in facilitating alcohols synthesis.

2.3.6 H_2-TPR catalysis of ZnCr catalysts

The redox properties of different catalysts were evaluated by H_2-TPR, the results are shown in Fig. 2.6. For each catalysts, there was only one hydrogen consumption peak in the temperature range of 300~400 ºC. As given in Fig. 2.6, the area of H_2 consumption peak had little change when the co-precipitation temperature changed from 5 ºC to 95 ºC, indicating that there was no the formation of new species or interaction. Though previous studies had shown that the H_2 consumptions of ZnCr catalyst was caused by the reduction of non-spinel $Zn_xCr_{2/3(1-x)}O$ [4,22], the exact structural information of $Zn_xCr_{2/3(1-x)}O$ was still not obtained until now. The surface OH groups species were used to stabilize oxygen vacancies created by cation disorder, which would be consumed by H_2 under higher temperature [1,9]. So the consumption of H_2 was partly caused by the surface oxygenates. Moreover, the over oxidized Cr

(Cr^{6+}) species were also reduced at the range of this temperature. Based on the above information, H_2 consumption was caused by the combination of surface oxygenates and oxidized Cr.

Integrating H_2 consumption peaks was employed to evaluate the concentration of $Zn_xCr_{2/3(1-x)}O$ and surface oxygenate. The following sequence was obtained: ZC-5 < ZC-95< ZC-60 <ZC-30, which indicated that ZC-60 and ZC-30 presented higher concentration of $Zn_xCr_{2/3(1-x)}O$ and surface oxygenate. The catalyst with more $Zn_xCr_{2/3(1-x)}O$ had been expected to show higher activity on alcohols synthesis [23]. So it cloud be expected that ZC-60 and ZC-30 presented higher CO conversion and alcohols selectivity than ZC-5 and ZC-94.

2.3.7 The acid-base properties characterization of ZnCr catalysts surface by using CO_2-TPD tests

CO_2-TPD was characterized to investigate the influence of co-precipitation temperature to the basic properties of the as prepared ZnCr catalysts. The profile and the fitted results are show in Fig. 2.7. Similar desorption peaks for CO_2 was observed on ZC-5 and ZC-30 catalysts, while the positions, heights and widths of ZC-60 and ZC-95 were quite different from those of ZC-5 and ZC-30. For ZC-60 catalyst, the weak base site appeared at 447 K, and the height and width were enhanced compared with other catalysts. For ZC-95, the weak base site appeared at 418 K, the strong base site shifted to 600 K and the middle base site of this ZC-95 emerged at 528 K was greatly enhanced compared with the other three catalysts. From the fitted results shown in Table

2.3, the distribution of basic strength of catalysts were different from one to another, while the total basicity increased with the co-precipitation temperature increased from 5 ^{o}C to 95 ^{o}C. The increased adsorption capacity of CO_2 may be caused by the surface oxygenates, which was beneficial to the formation of carbonate [24]. When the hydrothermal treatment was performed on the co-precipitated precursors of ZnCr catalysts at different temperature under atmospheric pressure, the configuration and amount of the carbonates and hydroxides on ZnCr catalysts would be changed, thus changing the basicity of ZnCr catalysts [19, 25].

Previous researchers[7, 22] have demonstrated that, the basicity of ZnCr catalyst effects β -addition, a process necessary for isobuatnol synthesis. Therefore, the basicity of ZnCr catalysts is an important factor to the formation of isobutanol. For these four ZnCr catalysts, strong basicity is suitable for β -addition reaction and isobutanol formation, thus higher selectivity of alcohols and isobutanol would be expected for ZC-60.

2.3.8 The FTIR spectra of ZnCr catalysts before and after reduction and its adsorption properties to CO

The FTIR spectra of ZnCr catalysts at different co-precipitated temperature before and after reduction in H_2 flow were shown in Fig. 2.8. According to Alfredo Riva et al. [26, 27], the band near 954 cm^{-1} and 1630 cm^{-1} are assigned to $\nu_{(Cr=O)}$ of chromate and absorbed water; the bands at 3682, 3668, 3648 cm^{-1} were due to the free surface OH groups; and the bands at 3578, 3510 cm^{-1} and a very broad absorption in the region

3500-2500 cm^{-1} were due to hydrogen-bonded OH groups. Weak bands near 1070-1490 cm^{-1} could be attributed to the carbonate species adsorbed on the catalysts external surface[23]. For the bulk catalysts (Fig. 2.7A), the vibration strength of chromate for ZC-5, ZC-30, and ZC-95 were stronger than ZC-60, while the strength of OH region of both free and hydrogen-bonded OH group for ZC-60 and ZC-95 are higher than ZC-5 and ZC-30. When the four catalysts were reduced inconstant H_2 flow by the same procedure, the difference of OH region was shown obviously. ZC-60 catalyst presented a remarkable absorption at 3646 cm^{-1}, while the other three catalysts only give signs on the strength and broader of the hydrogen-bonded region. This may be caused by the surface reduction reaction when H_2 was induced into the $Zn_xCr_{2/3(1-x)}O$ surface[28]. The following surface reaction supposed to occur on the ZnCr mixed oxide surface, possibly accounting for the formation of surface OH and H_2O derived from H_2:

$H_2 + 2\ O_{van1,surface} \rightarrow 2HO_{van1,surface}$ (1)

$H + HO_{van1,surface} \rightarrow O_{van2,surface} + OH$ (2)

The existence and strength of OH related surface may be in favor of the adsorption of CO and the formation of formate and carbonates during the reaction process [1].

In order to investigate the activation of CO on ZnCr catalysts, CO adsorption on the surface of the reduced catalysts were recorded by the FTIR spectra analysis preformed at 400 ^oC (Fig.2.9). FTIR absorption at 1550-1580 cm^{-1}, 1310 cm^{-1} and 1049-1078 cm^{-1} are ascribed to the formate adsorbed on ZnCr oxides[27, 29-32], while the peaks at 1610, 1370, 1352 cm^{-1} are ascribed to the carbonates adsorbed on metal oxide[27-29, 32, 33].As Fig 2.9 showed, when the catalysts were kept in the CO flow

at 400 ^{o}C for 50 min, the peaks resembling the $\nu_{as}(CO_2^-)$, δ(CH) and $\nu_s(CO_2^-)$ vibrations of formate group were obviously presented around 2964, 2855, 2732 cm^{-1}[26, 27].For all the catalysts, when the contact time of CO was prolonged, peaks denoted to the absorbance of formate and carbonates were intensified with the consumption of surface OH groups, which was indicated by the gradually decrease of wide bands at 3000 - 3500 cm^{-1}. The gradually decreasing of absorbance of surface OH and formate and carbonates indicated that surface OH participate in the activation of CO to form one of the C1 species for isobutanol synthesis.

As shown in Fig. 2.9, the consumption of surface OH groups and the increase of adsorbed formate and carbonates rely on the catalysts preparation process. For ZC-5 and ZC-95, the consumption amount of surface OH is lower than ZC-30 and ZC-60, and the intensity of carbonates is higher than foramte. While for ZC-30 and ZC-60, a big amount of surface OH consumption was obviously observed, and the amount of formate on ZC-60 is higher than ZC-30. Previous analysis to the surface Zn, Cr, and O species by XPS and FTIR spectra of bulk and reduced ZnCr catalyst mentioned above indicated that for ZC-60 a larger amount of surface OH was preserved. Since OH groups were considered to stabilize the surface oxygenate vacancies created by the disorder in ZnCr spinel [8], and more surface oxygenate vacancies cloud provide more catalysis sites to activation CO and synthesis of isobutanol. Hence, the higher selectivity of alcohols and isobutanol will be expected for ZC-60.

2.3.9 Catalyst active measurement

Table 2.3 shows the catalytic performance of ZnCr catalysts prepared at different co-precipitation temperature for isobutanol and methanol synthesis from syngas. The conversion of CO for ZC-5 and ZC-95 were extremely low, only ~12 %, and the selectivity of isobutanol were about 17 %, while for ZC-30 and ZC-60 the CO conversion were enhanced to 16 %.With the increase of CO conversion, alcohol selectivity were evaluated from 39% to 48% and 53% for ZC-30 and ZC-60, respectively. This trend was in accordance with the properties of OH groups for the four catalysts. As the analysis to FTIR spectrums of ZnCr oxides and CO absorption presented above, OH on the catalysts played a key role to the adsorption and activation of CO, and thus the high CO conversion and alcohol selectivity were observed on the catalyst with high concentration of surface OH.

2.3.10 Effects of surface OH on CO adsorption and the formation pathways of formate and carbonates on non-spinel-OH_3 surface by DFT calculations

As mentioned above, the existence of surface OH on ZnCr oxides catalysts predominately improved the activation of CO and selectivity to alcohols. To obtain a fundamental understand of the effects of the surface OH caused by oxygen defects on CO adsorption and activation, spin polarization DFT calculations over surface OH bonded spinel surfaces were investigated.

To mimic the surface properties of $Zn_xCr_{2/3(1-x)}O$, $ZnCr_2O_4$ (111) surface was chosen. The Zn and Cr atoms was replaced with a maximum number of 4 (when the number equals to 4, all the Zn and Cr on the surface of $ZnCr_2O_4$ was exchanged).

Energy of the system decreased gradually with the increasing number of exchanged atoms (Fig. 2.10), indicating the non-stoichiometric spinel is more stable than $ZnCr_2O_4$. After the surface of non-stoichiometric spinel was constructed, unsaturated oxygenates exposed on the surface was moved to mimic the vacancies; O5 and O3 site was moved for the formation energy of vacancies is low (Table 2.5). Then hydrogen was introduced to stabilize the surface oxygenates vacancies. The constructed model was denoted as non-spinel-OH_3.

The formation of formate and carbonates was studied by CI-NEB methods. The reaction coordinates and configuration of transition states were shown in Fig. 2.11 and Fig. 2.12. As can be seen from Fig. 2.11, formation of formate was found to exothermic by 0.68 eV, with an activation energy of 0.18 eV, while carbonates formation is found to be endothermic of 0.14 eV, with an activation of 3.89 eV. On the base of DFT results, we can obtain that result when CO reacted with surface OH, formation of formate both kinetically and thermodynamically.

On the constant flow of H_2, formate and carbonates can be easily hydrogenated into formal [34]. Previous research of our group ruled out that formal is one of the C_1 intermediate to form C_2 species which was considered to the rate determining step for isobutanol synthesis [16, 35, 36]. Under the reaction condition, the formate produced by CO reaction with surface OH can be easily transferred into formal, thus the catalyst with higher concentration of surface OH was expected to obtain ensure higher productivity of alcohol and isobutanol.

2.4 Conclusions

In this study, spectrums and surface analysis to the catalysts prepared at different co-precipitation temperature were adopted to investigate the effect of surface OH group on the catalytic performance of ZnCr catalyst for isobutanol direct synthesis from syngas. The studied results show that ZC-60 has the highest CO conversion (16.31%) and selectivity to isobutanol (18.30%) owing to the high concentration of surface OH. DFT calculation and FTIR absorption of CO results proved that the CO adsorption was intensified by surface OH, and formats is more easily formed than carbonates on non-spinel-OH_3 (111) surface both kinetically and thermodynamically. The high concentration of surface formate is in favor of the formation of the important C1 spices, therefore improving CO conversion and selectivity of alcohol and isobutanol on ZnCr mixed oxides catalyst.

References

[1] Tian S, Wang S, Wu Y, Gao J, Xie H, Li X, et al. The real active sites over Zn-Cr catalysts for direct synthesisi of isobutanol from syngas: structure-activity relationship. RSC Adv 2015;5:89273-81.

[2] Verkerk KAN, Bernd J, Heinrich FC, Wilhelm K. Recent developments in isobutanol synthesis from synthesis gas. Appl Catal A-Gen 1999;186:407-31.

[3] Sun X, Roberts GW. Synthesis of higher alcohols in a slurry reactor with cesium-promoted zinc chromite catalyst in decahydronaphthalene. Appl Catal

A-Gen 2003;247(1):133-42.

[4] Tan L, Yang G, Yoneyama Y, Kou Y, Tan Y, Vitidsant T, et al. Iso-butanol direct synthesis from syngas over the alkali metals modified Cr/ZnO catalysts. Appl Catal A-Gen 2015;505:141-9.

[5] Perego G. Characterization of heterogeneous catalysts by X-ray diffraction techniques. Catal Today 1998;41:251–9.

[6] Chen S, Wu Y, Cui P, Chu W, Chen X, Wu Z. Cation distribution in $ZnCr_2O_4$ nanocrystals investigated by X-ray absorption fine structure spectroscopy. J Phys Chem C 2013;117(47):25019-25.

[7] Tian S, Wang S, Wu Y, Gao J, Bai Y, Wang P, et al. Cation distribution in Zn–Cr spinel structure and its effects on synthesis of isobutanol from syngas: Structure–activity relationship. J Mol Catal A-Chem 2015;404-405:139-47.

[8] Tian S, Wang S, Wu Y, Gao J, Wang P, Xie H, et al. The role of potassium promoter in isobutanol synthesis over Zn–Cr based catalysts. Catal Sci Technol 2016;6(12):4105-15.

[9] Gao X, Wu Y, Yang G, Zhang T, Li X, Xie H, et al. Insight into the role of hydroxyl groups on the ZnCr catalyst for isobutanol synthesis from syngas. Appl Catal A-Gen 2017;547:1-11.

[10] Kresse G, Hafner J. Ab initio molecular dynamics for liquid metals. Phys Rev B 1993;47(1):558-61.

[11] Kresse G, Furthmüller J. Efficient iterative schemes for ab initio total-energy clculations using a plane-wave basis set. Phys Rev B 1996;54(16):11169-86.

[12] G. Kresse, Furthmüller J. Efficiency of ab-initio total energy calculations for metals and semiconductors using a plane-wave basis set. Comput Mater Sci 1996;6:15-50.

[13] Jia C, Fan W, Yang F, Zhao X, Sun H, Li P, et al. A theoretical study of water adsorption and decomposition on low-index spinel $ZnGa_2O_4$ surfaces: correlation between surface structure and photocatalytic properties. Langmuir 2013;29(23):7025-37.

[14] Jia C, Fan W, Cheng X, Zhao X, Sun H, Li P, et al. The roles of surface structure, oxygen defects, and hydration in the adsorption of CO_2 on low-index $ZnGa_2O_4$ surfaces: a first-principles investigation. Physical chemistry chemical physics : PCCP 2014;16(16):7538-7547.

[15] Li Y, Lian F, Chen N, Hao Z, Chou K-c. Structural predictions based on the compositions of cathodic materials by first-principles calculations. Int J Miner Metall Mater 2015;22:524-9.

[16] Gao X, Zhang T, Wu Y, Yang G, Tan M, Li X, et al. Isobutanol synthesis from syngas on Zn-Cr based catalysts: New insights into the effect of morphology and facet of ZnO nanocrystal. Fuel 2018;217:21-30.

[17] Zhang L, Ji GF, Zhao F, Gong ZZ. First-principles study of the structural, mechanical and electronic properties of ZnX_2O_4(X=Al, Cr and Ga). Chin Phys B 2011;20(4):1-7.

[18] Koilraj P, Kannan S. Aqueous fluoride removal using ZnCr layered double hydroxides and their polymeric composites: Batch and column studies. Chem

Eng J 2014; 234: 406-415.

[19] Z. Chen, Y. Zhang, W. Lu, Y. Cheng, J. Tan. Formation mechanism of hydrothermally synthesized $ZnCr_2O_4$ crystallites. J Synth Cryst 2014;43(2):355-60.

[20] Steinberger R, Duchoslav J, Arndt M, Stifter D. X-ray photoelectron spectroscopy of the effects of Ar^+ ion sputtering on the nature of some standard compounds of Zn, Cr, and Fe. Corros Sci 2014;82:154-64.

[21] Miyakoshi A, Kakuta N, Ueno A, Ichikawa M. Dehydrogenation of ethylbenzene over double oxide catalysts of ZnO–Cr_2O_3 catalyst preparation and their catalytic performances.NIPPON KAGAKU KAISHI2000(2):97-105.

[22] Kou Y, Xie H, Liu G, Wu Y, Zhang X, Han Y, et al. Effect of calcination temperature on the performance of ZnCr based catalyst in isobutanol synthesis. Journal of Fuel Chemistry and Technology 2013;41(6):703-9.

[23] Venugopal A, Sarkari R, Kumar SN, Kumar MK, John SS, Redd JK, et al. Effective utilization of glycerol for the synthesis of 2-methylpyrazine over ZnO-$ZnCr_2O_4$ catalyst. J Chem Sci 2014;126(2):387-93.

[24] Wang Y, Kovácik R, Meyer B, Kotsis K, Stodt D, et al. CO2 activation by ZnO through the formation of unsual tridentate surface carbonate. Ahgew Chem Int Ed 2007;46:5624-27.

[25] S. Naz, SK Durrani, M Mehmood, M Nadeem. Hydrothermal synthesis, structural and impedance studies of nanocrystalline zinc chromite spinel oxide material. J Saudi Chem Soc 2016;20(5):585-93.

[26] A. Riva, F. Trifirb, A. Vaccari, L. Mintchev, G. Busca. Structure and reactivity of zinc-chromium mixed oxides part 2.study of the surface reactivity by temperature-programmed desorption of methanol. J Chem Soc, Faraduy Trans I 1988;85(5):1423-35.

[27] A. Riva, F. Trifirb, A. Vaccari, G. Busca, L. Mintchev, D. Sanfilippo, et al. The promoting role of Cr and K in catalysts for high-pressure and high-temperature methanol and higher-alcohol synthesis. J Chem Soc Faraday TransI 1987;83:2213-25.

[28] V Sanchez Escribano, MA Larrubia Vargas, E. Finocchio, G. Busca. On the mechanisms and the selectivity determining steps in syngas conversion over supported metal catalysts: An IR study. Appl Catal A-Gen 2007;316(1):68-74.

[29] TC Schilke, IA Fisher, AT. Bell. In situ infrared study of methanol synthesis from CO_2/H_2 on titania and zirconia promoted Cu/SiO_2. J Catal 1999;184:144-56.

[30] K. Hadjiivanov, T. Venkov, H. Knözinger. Infrared study of the adsorption of methanol on oxidised and reduced Cu/SiO_2 catalysts. J Chem Soc Faraday Trans 1991;87(17):2795-2804.

[31] H. Noei, C. Wo, M. Muhler, Y. Wang. Activation of carbon dioxide on ZnO nanoparticles studied by vibrational spectroscopy. J Phys Chem C 2011;115:908-914.

[32] A.Fisher I, T.Bell A. In situ infrared study of methanol synthesis from H_2/CO over Cu/SiO_2 and Cu/ZrO_2 /SiO_2. J Catal 1998(178):153-73.

[33] Q. Sun, C. Liu, W. Pan, Q. Zhu, J. Deng. In situ IR studies on the mechanism of methanol synthesis over an ultrafine Cu/ZnO/Al_2O_3 catalyst. Appl Catal A-Gen 1998;171:301-8.

[34] A. Kiennemann, R .Kieffer, S. Boujana, G. A.Martin, J.A. Dalmon, P.Meriaudeau, et al. Evolution of alcohol synthesis catalysts under syngas. Ind.Eng.Chem.Res., 1994;33:1460-67.

[35] Y. Wu, H. Xie, Y. Kou, N. Tsubaki, Y. Han, Y. Tan. The mechanism of higher alcohol formation on ZrO_2-based catalyst from syngas. Korean J Chem Eng 2014;32(3):406-12.

[36] KJ. Smith, B. Anderson R. A chain growth scheme for the higher alcohols synthesis. J Catal 1984;85:428-36.

Table 2.1. The bulk and surface ratio of Zn/Cr for ZC-x catalyst samples.

Catalysts	Zn/Cr (bulk)	Zn/Cr (surface)
ZC-5	1.05	0.836
ZC-30	1.05	0.741
ZC-60	1.04	0.765
ZC-95	1.05	0.830

Table 2. 2. Ratios of the absorbed oxygenatesO_{ads} to the total oxygen species (O_{latt} + O_{ads}).

Catalysts	$O_{ads}/(O_{latt} + O_{ads})$
ZC-5	33.72
ZC-30	35.57
ZC-60	40.94
ZC-95	40.35

Table 2.3. The fitted area of CO_2-TPD profile for the samples

catalysts	area					
	α	β	γ	δ	ε	Σ
ZC-5	63.768	60.264	101.761	119.665	48.431	393.559
ZC-30	42.889	14.273	271.556	35.291	22.440	386.449
ZC-60	60.560	148.413	145.291	111.351	118.018	583.633
ZC-95	75.886	199.990	85.657	109.068	42.647	513.248

Table 2.4 Typical catalytic performance of ZnCr catalysts

catalysts	CO conversion	Alcohol, C	Total alcohol rate	Alcohol distribution (wt%)				
	(%)	mol %	(g/L.h)	Methanol	Ethanol	Propanol	Isobutanol	C_{5+} alcohol
ZC-5	12.60	39.93	70	74.95	3.17	0.35	17.08	1.70
ZC-30	15.11	48.42	90	76.65	2.78	0.36	16.27	1.57
ZC-60	16.31	53.49	80	75.06	2.27	0.03	18.30	1.21
ZC-95	12.71	39.63	70	76.51	2.64	0.27	16.95	1.49

Reaction conditions: temperature= 400 ^{o}C, pressure=10.0 MPa, and GHSV=3000 h^{-1}

Table 2.5. Formation energy of oxygen vacancy of with respect to the unsaturated $ZnCr_2O_4$ (111) surface oxygen atom

Site of oxygen vacancy	Energy of oxygen vacancy formation, eV
O1[a]	2.72
O2[a]	2.82
O3[a]	2.75
O4[a]	3.87
O5[a]	2.55
O5-O1[b]	3.38
O5-O3[b]	3.21
O5-O3-O1[c]	3.48

a. Formation of only one oxygen vacancy;
b. Formation of two oxygen vacancies;
c. Formation of three oxygen vacancies.
Formation of oxygen vacancies on $ZnCr_2O_4$ (111) surface was calculated according to reference (J. Phys. Chem. C, 2012,116(11):6636-44).

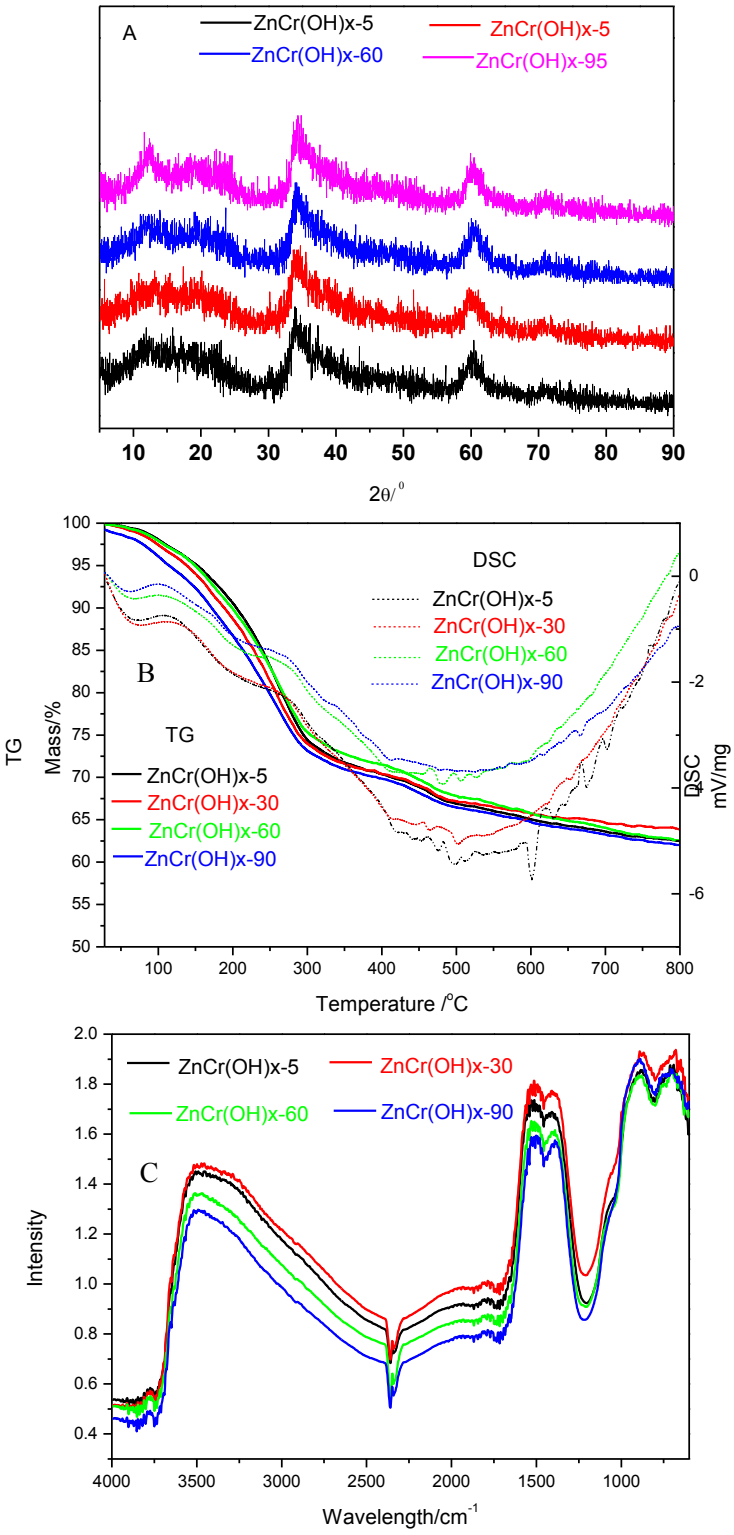

Fig. 2.1. XRD spectra (A), TG-DSC curves (B) and IR spectrum (C) for the ZnCr(OH)x-y samples.

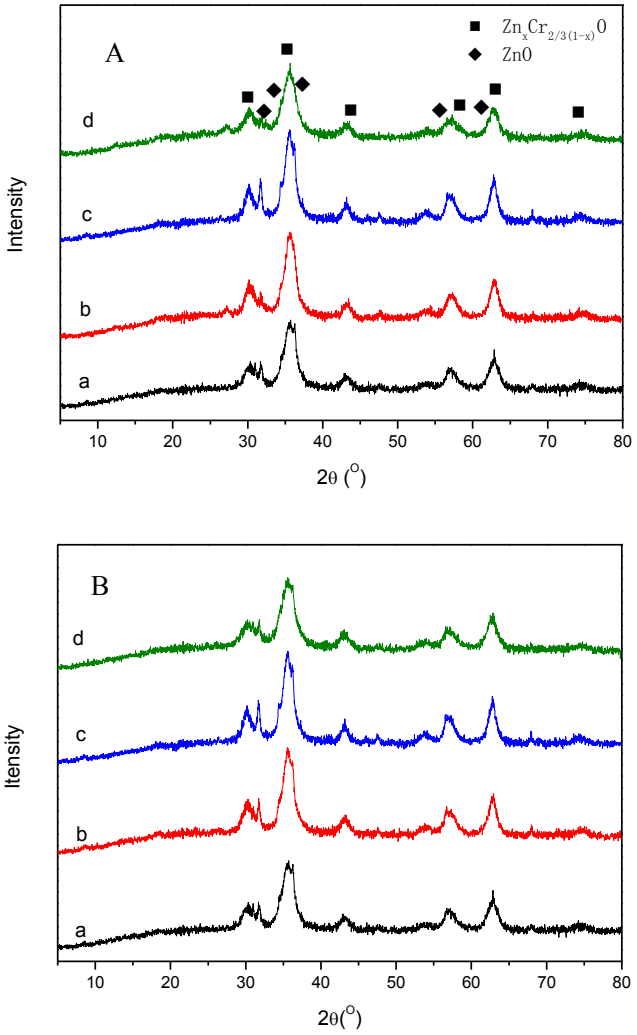

Fig. 2.2. XRD of spectra for the final catalysts before (A) and after (B) reaction (a): ZC-5; (b): ZC-30; (c): ZC-60 and (d): ZC-95.

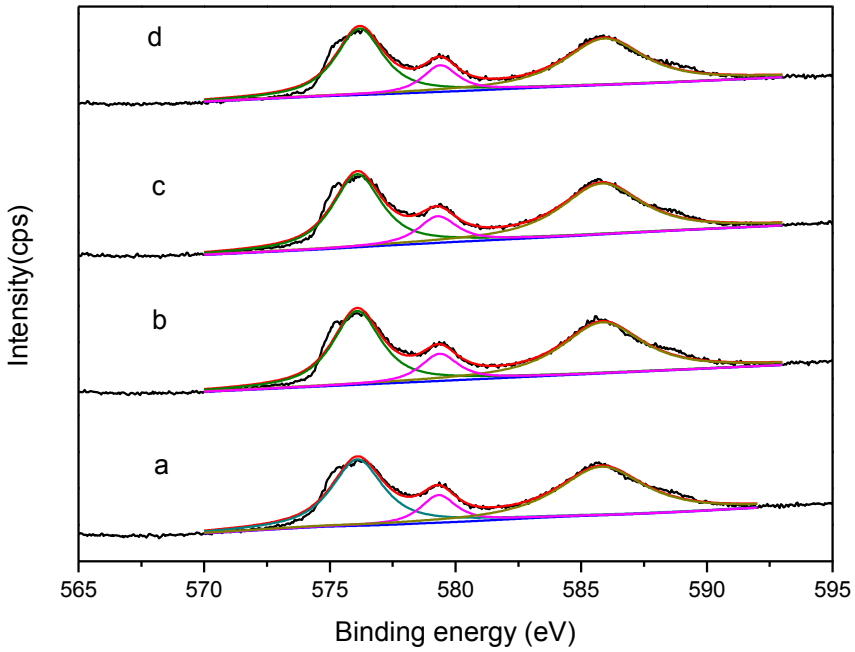

Fig. 2.3. Cr 2p XPS of spectra of catalysts (a): ZC-5; (b): ZC-30; (c): ZC-60 and (d): ZC-95.

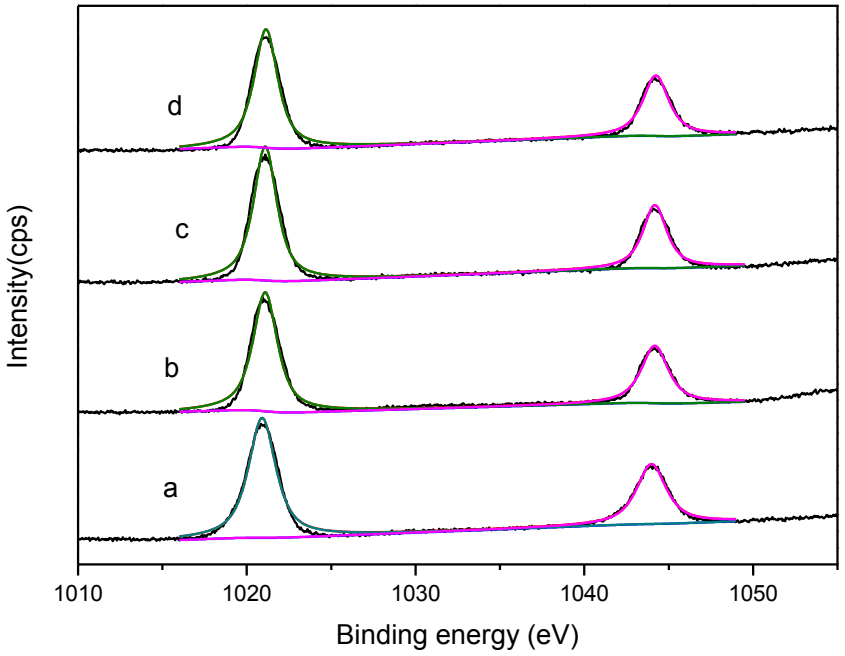

Fig. 2.4. Zn 2p XPS of spectra of catalysts (a): ZC-5; (b): ZC-30; (c): ZC-60 and (d): ZC-95.

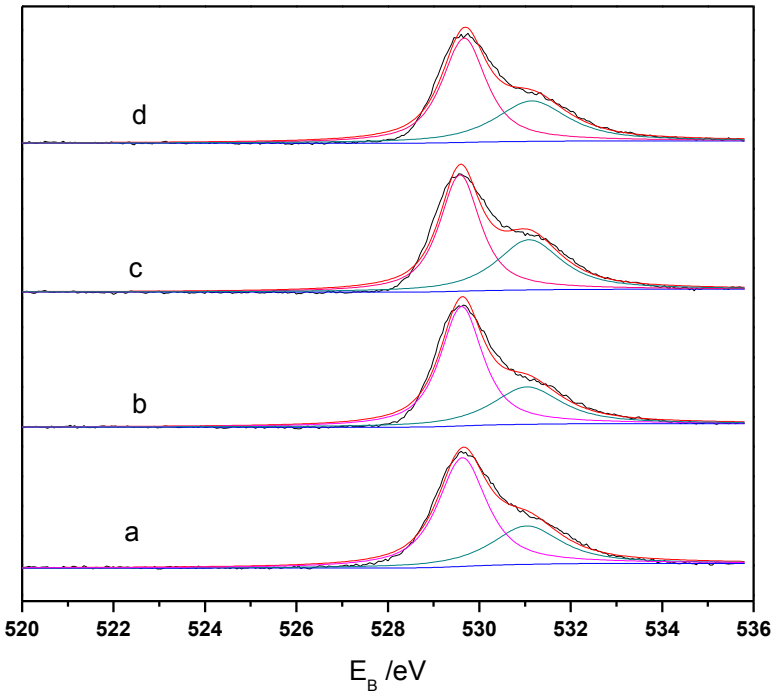

Fig. 2. 5. O1s XPS of spectra of catalysts: (a): ZC-5; (b): ZC-30; (c): ZC-60 and (d): ZC-95.

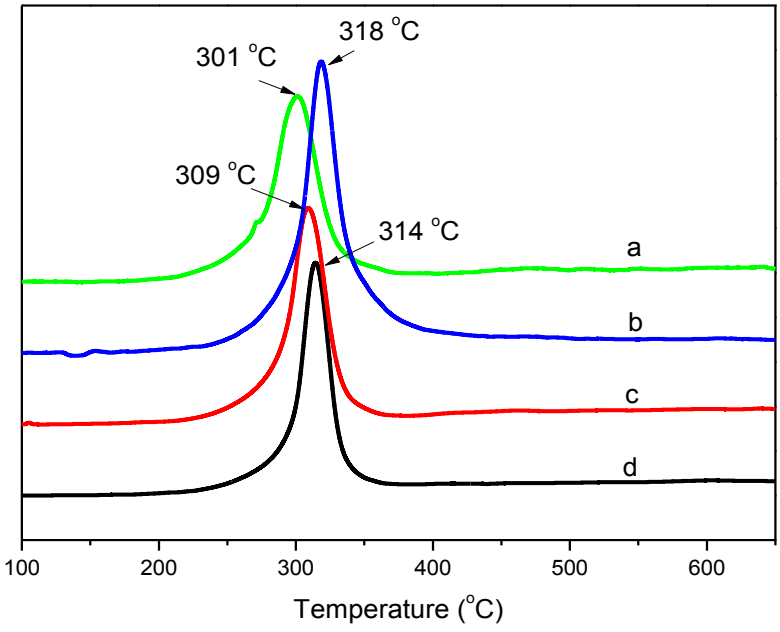

Fig. 2. 6. H_2-TPR profiles of the catalysts (a) ZC-5, (b) ZC-30, (c) ZC-60 and (d) ZC-95.

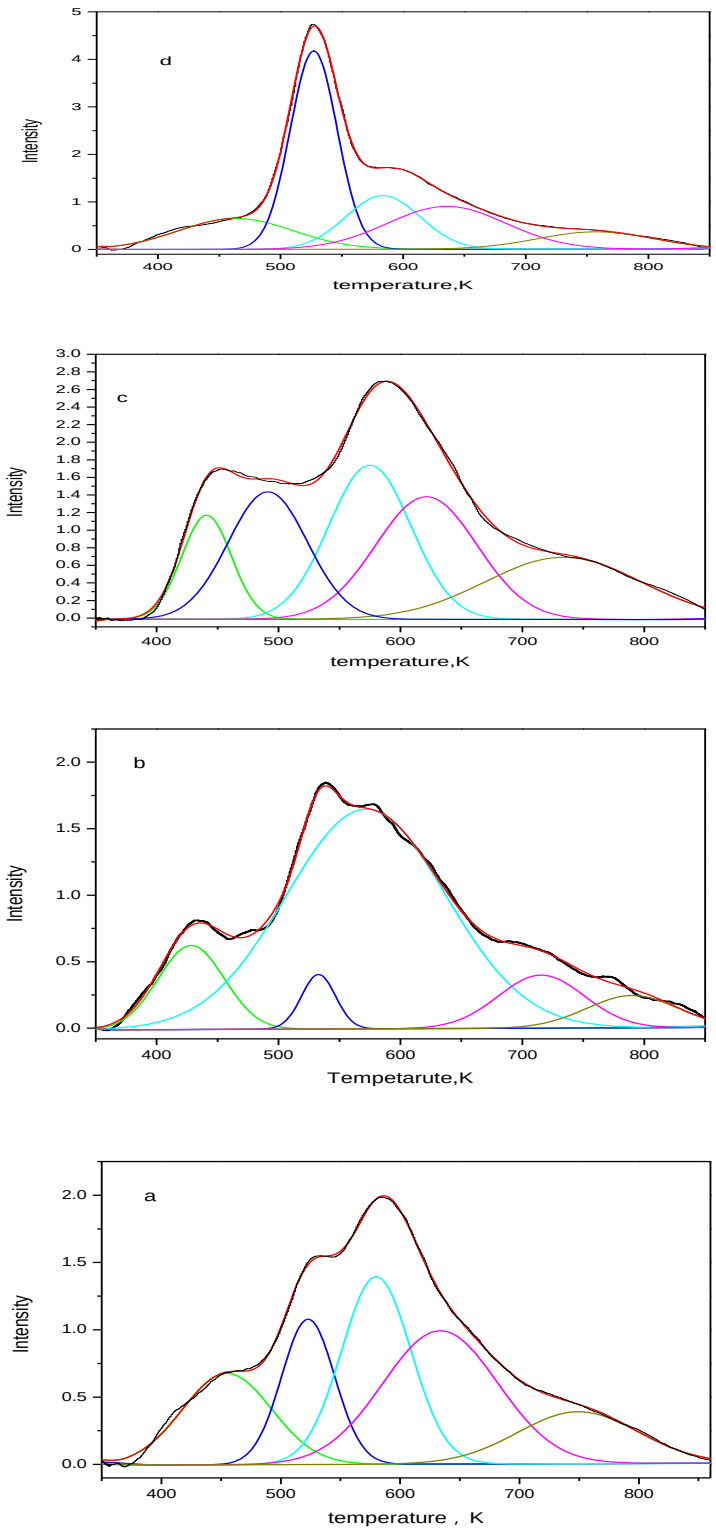

Fig. 2.7. CO_2-TPD spectra of catalysts (a): ZC-5; (b): ZC-30; (c): ZC-60 and (d): ZC-95.

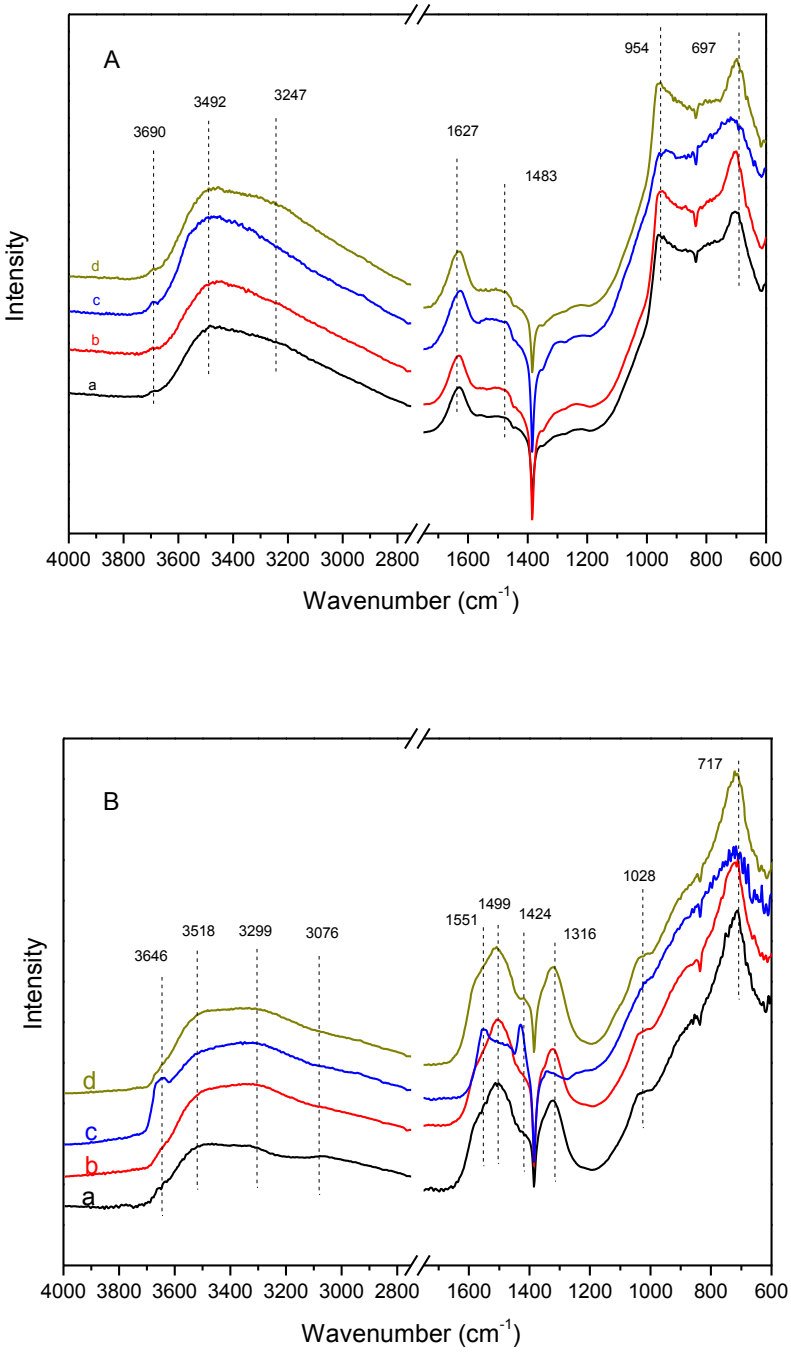

Fig. 2. 8. FTIR spectra of the bulk ZnCr catalysts samples recorded at 30 ^{o}C without treatment (A) and the reduced by H_2 at 400 ^{o}C (B).

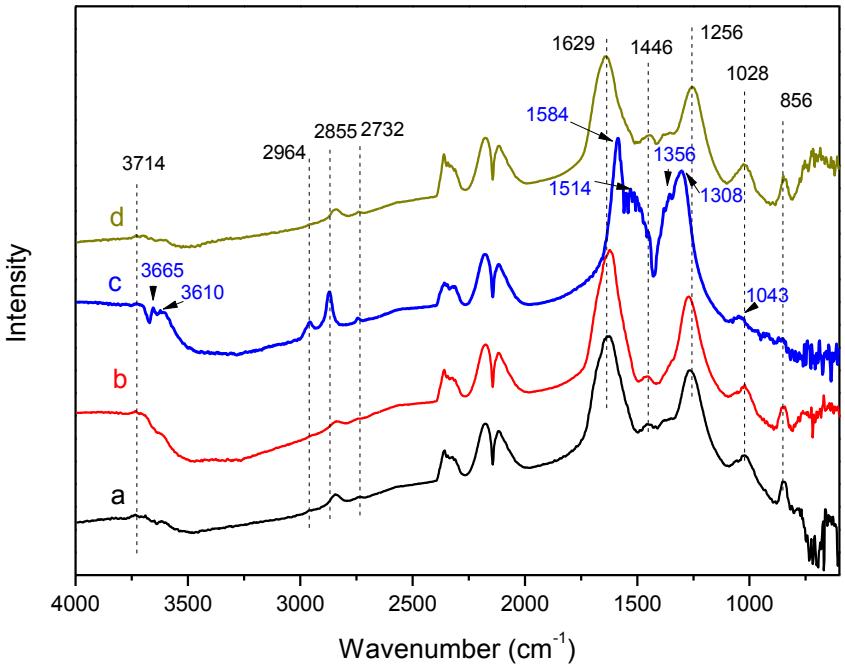

Fig. 2.9. FTIR spectra of CO absorption recorded at 400 ºC for the reduced catalysts samples. (a): ZC-5; (b): ZC-30; (c):ZC-60 and(d): ZC-95.

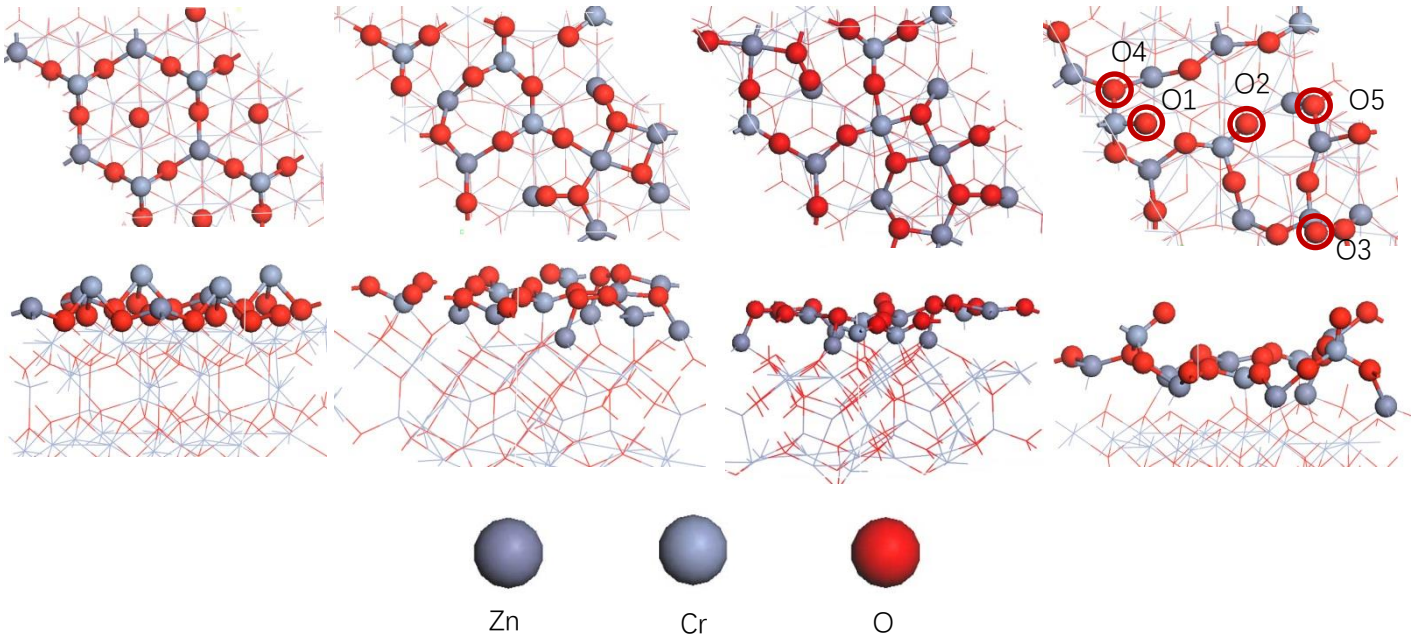

Fig. 2.10. Configurations of top view and side views of $ZnCr_2O_4$ (111) surface with different extent of exchanged surface Zn and Cr atoms.

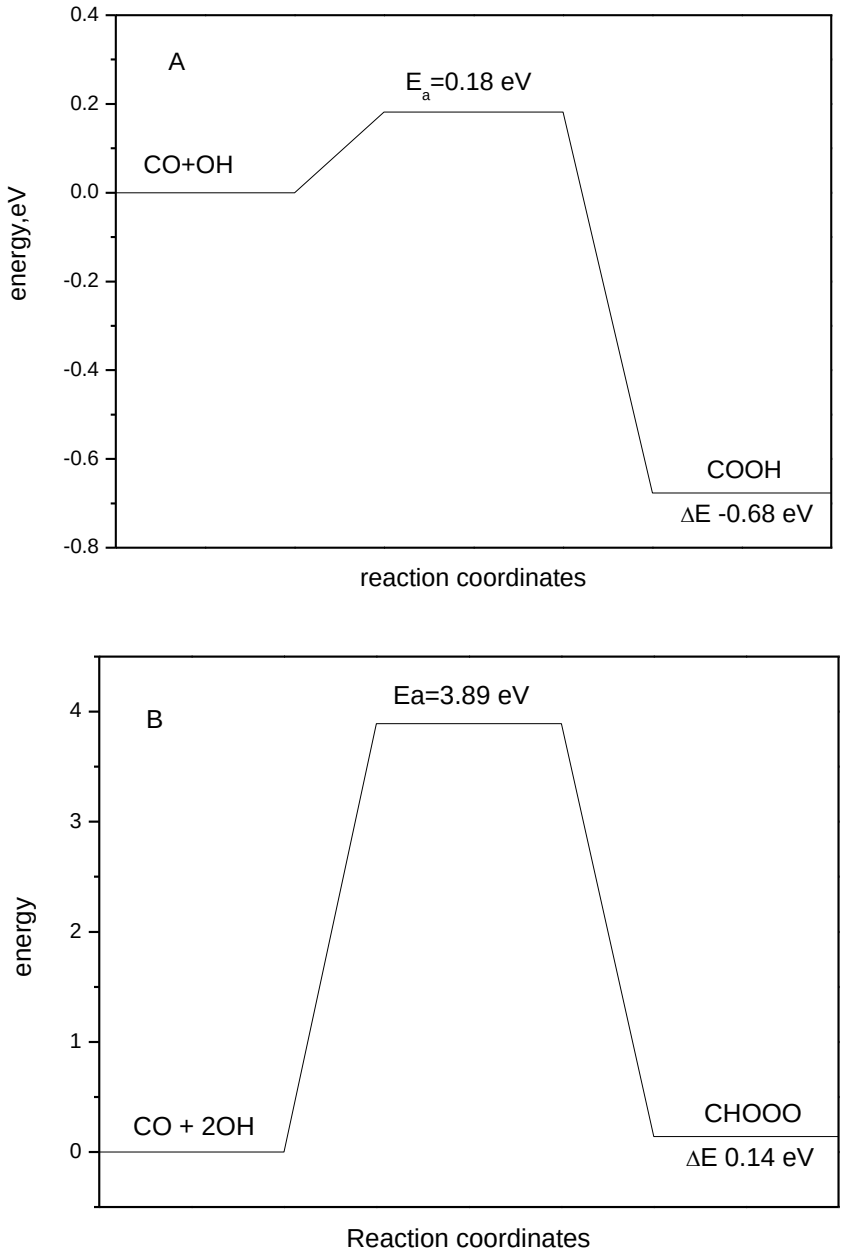

Fig. 2.11. The potential energy diagram for formate and carbonates formation through the rection between surface OH and CO. (A): formate formation; (B) carbonates formation.

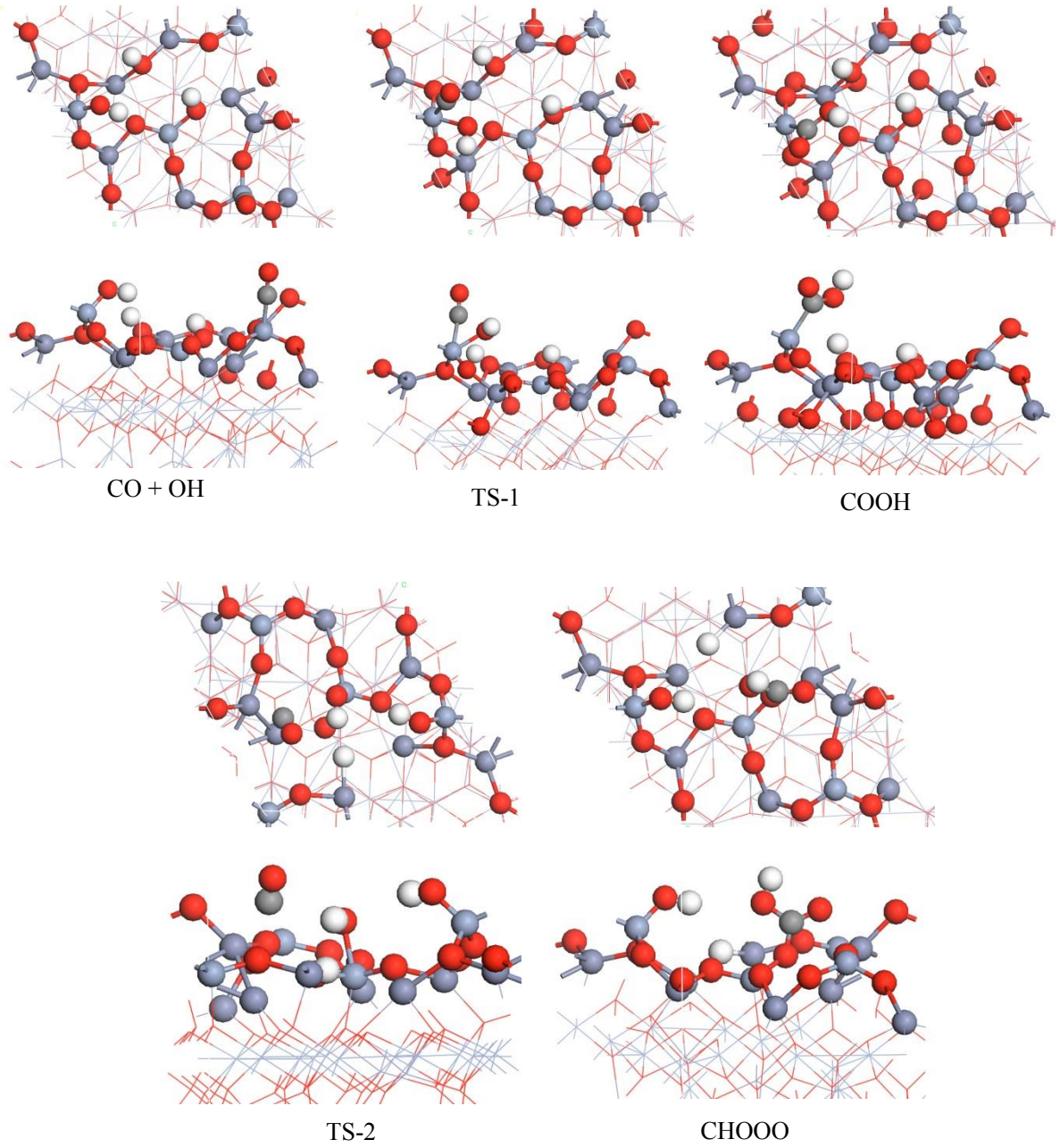

Fig. 2.12 . The top and side views of the initial states, transition states and final states for formate and carbonates formation on non-spinel-OH_3 surfaces.

Chapter 3

Roles of Ga^{3+} promoter for direct synthesis of iso-butanol via syngas over K-ZnO/$ZnCr_2O_4$ catalyst

ZG, Ga clusters and $ZnGa_2O_4$ were formed by introducing Ga^{3+} to K-ZnO/$ZnCr_2O_4$ iso-butanol catalyst. Only a moderate amount of ZG promotes the space time yield (STY) and selectivity of alcohols for iso-butanol synthesis.

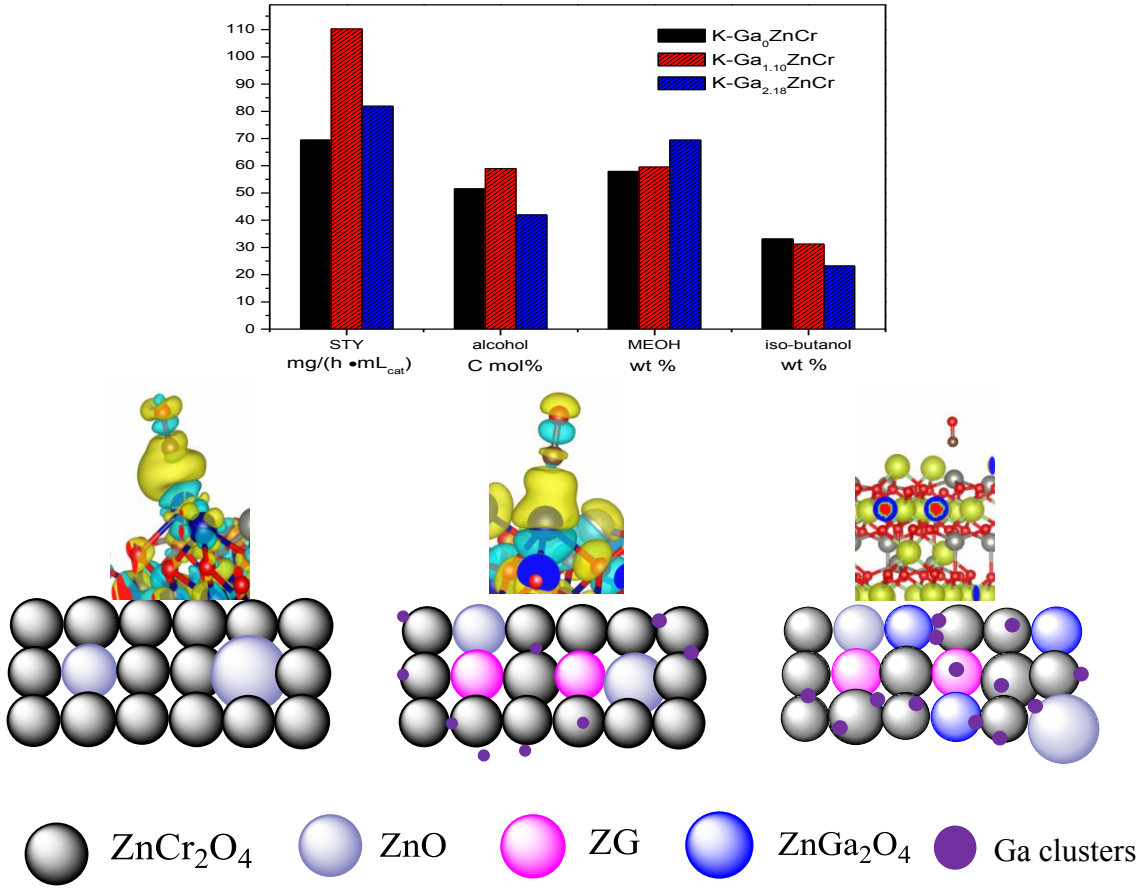

$ZnCr_2O_4$: zinc chromium spinel	ZnO: zinc oxide
ZG: tetra-coordinated Ga^{3+} located in ZnCr spinel	$ZnGa_2O_4$: zinc gallium spinel

Abstract

The direct synthesis of iso-butanol is an important reaction in syngas (composed of CO and H_2) conversion. K-ZnO/$ZnCr_2O_4$ (K-ZnCr) is a commonly used catalyst. Here, Ga^{3+} is used as an effective promoter to boost the efficiency of the catalyst and retard the production of CO_2. X-ray diffraction, X-ray photoelectron spectroscopy, ultraviolet-visible diffuse reflection spectrum and electron microscopy were used to characterize the structural variations with different amount of Ga^{3+}, the results showed that the paticle size of the catalyst decrease with the addition of Ga^{3+}. Temperature-programmed desorption of NH_3 and CO_2, and diffuse reflectance infrared Fourier-transform spectroscopy (DRIFTs) analysis of the CO adsorption revealed that the acidity and basicity were altered owing to the different form of Ga^{3+} adoption. X-ray photoelectron spectroscopy and density functional theory (DFT) calculations revealed that the formation of Ga clustes that coordinated on the exposed surfaces of $ZnCr_2O_4$, and undergo a tetra-coordinated Ga^{3+} exchange with one of Zn in $ZnCr_2O_4$ (ZG) and $ZnGa_2O_4$, probobly formed deponds on the amount of Ga added. The structural evolution of the Ga^{3+} promoted K-ZnO/$ZnCr_2O_4$ catalysts can be described as follows: （ⅰ）the main forms are ZG and Ga coordinated $ZnCr_2O_4$, in which the amount of Ga^{3+} is below 1.10 wt%; and（ⅱ）the Ga^{3+} containing compound is gradually changed from ZG to $ZnGa_2O_4$ and the amount of gallium cluster increased when the amount of Ga^{3+} was higher than 1.10 wt% . The catalytic performance evaluation results show that K-$Ga_{1.10}$ZnCr exhibits the highest space time yield and selectivity of alcohols, in which the three compounds play different roles in syngas conversion: ZG is the main active

site that boosts the efficiency of the catalysts, owing to the intensified CO adsorption and decreased activation energy of CHO formation through CO hydrogenation; $ZnGa_2O_4$ only modifies the surface basicity and acidity on catalyst, thereby impacting carbon chain growth after CO is adsorbed. The effects of Ga coordinated with $ZnCr_2O_4$ show little impact on CO adsorption owing to the weak electron donating effects of Ga.

Keywords: syngas, $ZnCr_2O_4$, iso-butanol, Ga^{3+} doption

3.1 Introduction

The increasing demand for clean fuel has ignited research on converting carbon containing substance to fuel or valuable chemicals [1]. Syngas, mainly composed of H_2 and CO, is usually obtained through gasification of coal or biomass or is produced by methane and CO_2 reforming, and is an important platform material for producing gasoline, diesel oil and may valuable chemicals [2]. Iso-butanol is an important chemical among all the downstream products of syngas and can be used as gasoline additives to improve the octane number [3, 4]. In addition, iso-butanol can also be used to purify rare earth or produce important chemicals [5]. However, until now, the main production route of iso-butanol is carbonylation of propylene and fermentation of sugar [4, 5]. Hence, it is urgent to produce iso-butanol using an alternative approach.

Direct synthesis of iso-butanol through syngas has been proven to be an effective method owing to the wide usage of carbon contained substance and high selectivity of iso-butanol [4, 6, 7]. Among all the catalysts, the K-ZnO/$ZnCr_2O_4$ (K-ZnCr) catalyst is considered to be a good candidate owing to its longer life time and reduced CO_2 emissions [4, 8, 9]. To determine the reaction mechanism of K-ZnCr catalyst, researchers performed a lot of work to disclose the structure-property relationships. For instance, Tian et al. proposed that the non-stoichiometry ZnCr spinel is the active site that produces iso-butanol, and this so-called non-stoichiometry structure is constructed by the disorder of Zn^{2+} and Cr^{3+} in spinel crystal crystal cell [8, 10, 11]. Gao et al. enhanced the performance of catalyst by modulating the configuration and amount of ZnO [12-14]. In addition to the studies on the structure activity performance of ZnCr

catalyst, other researchers also attempted to explore its reaction mechanism of alcohol formation. For example, Kevin J. Smith et al. revealed that the selectivity of methanol and iso-butanol is controlled by the activity of an α- or β-carbon atom of the growing alcohol [14]. Luca Lietti et al. investigated the complex reaction network of higher alcohol synthesis by studying the temperature-programmed reaction of C_3, C_4, and C_5 oxygenates over K-promoted ZnCr catalyst [15,16]. Inspired by these researchers, Wu et al. explored the rate-determining step of iso-butanol formation and found that the formation of C_2 oxygenates through CO and formyl (CHO) is the key step by controlling the reaction atmosphere and enriching the intermediate alcohols [5, 17].

Based on the reaction mechanism, some researchers have made numerous efforts to further promote the efficiency of ZnCr catalyst by adding promoters. For example, William S. Epling at al. added Pd and Mn to boost the selectivity of iso-butanol and alcohols under the reaction condition of 10 MPa, 430 ^oC on Cs- promoted ZnCr catalyst [18-21]. However, until now, the systematic study concentrated on the influence of the third composition on the structure of ZnCr iso-butanol catalyst is rarely reported. Moreover, among all these investigations, the amount of CO_2 in tail gas is relatively high. Therefore, reducing the amount of CO_2 emissions during iso-butanol synthesis is also an important issue.

In recent years, Ga^{3+} has been used as a promoter to modulate the electron properties, textural properties, configurations and distribution of active site composition of Co, Co/AC, CuAl, CuZnAl catalysts to further modify the activation of CO during synthesis of alcohols [6, 22-25]. In addition, Ga^{3+} can also be used to

modulate the efficiency of water-gas-shift reaction or to improve the performance of CO_2 conversion by altering the acid-base properties of the catalyst [26-28]. However, when Ga was introduced into Zn contained catalyst, the existing form of Ga and its effect on the performance of the catalyst was still conflicting. For example, Molly Meng-Jung Li et al. proposed that the formation of $ZnGa_2O_4$ creates an electronic heterojunction with excess ZnO to facilitate the reduction of Zn^{2+} to Zn in CuZnO methanol catalyst [27]. Hyungwon Ham et al. confirmed that phase transformation of gallium oxide from tetrahedral Ga-O sites to octahedral Ga-O sites suppressed the formation of dimethyl ether (DME) [29]. At present, whether the catalytic performance of K-ZnCr is promoted by the introduction of Ga^{3+} is not clear based on our knowledge. In addition, forms of existence of Ga, its impact on the structure of catalyst and the explicit role it plays during the reaction are still unknown. To unravel the above-mentioned problems, Ga^{3+} was added into K-ZnCr iso-butanol catalyst to modulate the surface structure through the formation of novel compounds to further improve the performance of the catalyst.

3.2 Experimental section

3. 2.1 Catalyst preparation

Ga^{3+} promoted K-ZnCr catalysts were prepared by precipitation-impregnation method. The precursors for Zn, Cr and Ga are zinc nitrate hexahydrate, chromium nitrate nine-hydrate and gallium nitrate hydrate, respectively. In a typical procedure, the aqueous solutions of $Zn(NO_3)_2 \cdot 6H_2O$ and $Cr(NO_3)_3 \cdot 9H_2O$ (molar ratio of

Zn:Cr=1:1) was precipitated with $(NH_4)_2CO_3$ aqueous solution. Detailed procedure is described in our precious report [30]. The precipitate was dried at 100 ºC for 12 h, then milled into a powder and impregnated with the aqueous solution of gallium nitrate hydrate, then dried at 100 ºC for 12 h and calcined at 400 ºC in a muffle furnace under a steady atmosphere for 4 hours to get GaZnCr samples. Finally, GaZnCr samples were impregnated with the aqueous solution of K_2CO_3, then dried and calcined according to the process of preparing GaZnCr to obtain the final catalysts, the samples can be abbreviated as K-GaZnCr. The amount of Ga (mole fraction) is changed from 0, 0.55 1.10, 1.64, to 2.18 wt%, respectively. The final catalysts were denoted as K-Ga_xZnCr, where x represents the loading amount of Ga.

3.2.2 Catalyst evaluation for iso-butanol synthesis

The performance of the catalysts was evaluated in a fixed-bed tubular reactor, composed of a titanium alloy tube (Φ10×2×400 mm) inserted in a furnace. 1.0 g of the catalyst with the particle size of 50 to 60 mesh was packed, and the two ends were stuffed with quartz sand to support the catalyst. Before introducing syngas, the catalyst was reduced using 10% H_2 in N_2 with a flow rate of 100 mL/h at 400 ºC for 6 h. After reduction, syngas with a molar ratio of H_2/CO = 2.4 was introduced into the reactor. The reaction conditions were as follows: pressure at 10.0 MPa, gas hourly space velocity (GHSV) 3300 h^{-1} and reaction temperature of 400 ºC. The detailed procedures of sample collection, the composition analysis of syngas, tail gas and liquid phase were described in our previous report [11, 30].

3.2.3 Characterization

The specific surface face areas were obtained according to the Brunauer-Emmett-Teller (BET) method using nitrogen adsorption and desorption isotherms at -196 ºC on an ASAP 2020 V4.03 equipment. Before the test, each sample was degassed at 200 ºC for 4 h. The morphology and microstructure of the catalysts were investigated using high resolution elecrtron microscopy (HRTEM, JEM-2100F) operated at 200 kV (produced by Japan Electronics Co., Ltd). The X-ray diffraction (XRD) data for K-Ga_xZnCr catalysts were recorded using a D8 Advance X-ray diffractometer in the 2θ range from 10º to 80º with Cu Kα radiation. To obtain a spectrum with high quality, the scanning step size and speed are set to 0.01 and 1º/min, respectively. The X-ray photoelectron spectroscopy (XPS) patterns were recorded using an AXIS ULTRA DLD X-ray photoelectron spectrometer equipped with a multichannel detector. Charge referencing was performed against adventitious carbon (C 1s, 284.8 eV). A Shirley-type background was subtracted from the signals. The recorded spectra were fitted using Gaussian-Lorentzian curves to determine the composition of the surface of the different samples. CO_2 and NH_3 temperature programmed desorption profiles were recorded on a TP-5050 automatic chemical adsorption instrument.

The test temperature is in the range from 50 ºC to 800 ºC. The catalyst samples were reduced using the mixture of 10% H_2 and 90% N_2. The reduction was performed at 400 ºC for 2.5 hours with the heating rate of 10 ºC/min. After reduction, the samples were cooled to 50 ºC under the protection of 10% H_2 and 90% N_2. Then, the catalysts were treated in a constant flow of N_2 with a rate of 30 mL/min to eliminate the

physically adsorbed water and contaminates. After that, NH_3 or CO_2 was introduced into the system for 0.5 h to achieve saturated adsorption. The samples were purged with N_2 for about 1 hour to remove the physically absorbed NH_3 or CO_2. Finally, the temperature was increased with the rate of 10 ^oC/min by a constant N_2 flow. The signals of CO_2 and NH_3 were recorded by a thermal conductivity detector respectively. X-ray fluorescence (XRF) spectra were recorded using an E3 Tiger XRF spectrometer with a silicon drift detector (SDD). Raman spectra and solid-state UV-visible spectra were also recorded to reveal the influence the Ga species on the K-Ga_xZnCr catalyst structure. A Raman test was performed using a HORIBA 800 with 532 nm excitation wavelength. Solid state UV-visible spectrums were recorded in SU3900 spectrophotometer, the scanning range is from 200 nm to 800 nm by using barium sulfate as the base.

For the above analysis, BET, XPS, Raman spectra and Solid state ultraviolet-visible diffuse reflectance spectrums were performed to the reduced catalyst samples. The composition of the reduction gas and procedure was identical to the procedure used before catalyst evaluation.

In addition, FT-IR spectra of CO adsorption were obtained on TENSOR-27 in the range of 4000 to 600 cm^{-1} with 4 cm^{-1} resolution, the detailed procedures for CO adsorption were described in our earlier reports [30].

3.2.4 Computational methods

The periodic DFT calculation was performed by using Vienna ab initio simulation Package (VASP) [31-34]. The generalized gradient approximation with the Perdew-

Burke-Ernzerh functional was used to deal with the electron exchange-correlation energy. The projector-augmented wave method was used to describe the interactions between electrons and atomic cores, the cutoff energy for the plane-wave basis set was 450 eV. Van der Waals interaction was taken into consideration by DFT-D3 method. The geometry optimizations was performed by conjugate gradient algorithm (IBRION=2) and quasi-Newton algorithm (IBRION=1) with the convergence criterion for energy and force were less than the value of 10^{-5} eV and 0.02 eV/Å, respectively. A 1×1×1 k-point grid method was applied to sample the Brillouin zone. The transition state seeking for the elementary reactions of CO activation was studied by climbing image nudged elastic band (CI-NEB) method [35]. The obtained saddle point was confirmed by frequency analysis to have a single imaginary frequency. All the surface atoms were fixed except for the relaxation of the adsorbed molecule or groups such as CO, C, H, CHO during CI-NEB calculations based on our computational resources.

The adsorption energies of related adsorbed species such as CO, CHO, H_2O and CO_2 were computed by the equation: $E_{ads} = E_{x/slab} - (E_x + E_{slab})$, where $E_{x/slab}$, E_{slab} and E_x are the total energies of species absorbed on the slab, the slab and the isolated gas species, respectively. The reaction energy ΔE and activation energy E_a are evaluated through the following equation (2) and (3):

$$\Delta H = E_{fs} - E_{is} \quad (2)$$

$$E_a = E_{ts} - E_{is} \quad (3)$$

where E_{fs}, E_{is} and E_{ts} are the energies of products, reactants and transition states, respectively.

3.2.5 Models

3.2.5.1 The possible locations of Ga^{3+} in $ZnCr_2O_4$

The possible locations of Ga^{3+} in the doped K-ZnO/$ZnCr_2O_4$ catalyst were confirmed by DFT calculation. The flowing possible locations of Ga^{3+} were fall in our consideration, that is (1) Zn^{2+} located at ZnO was replaced by Ga^{3+}, demoted as $Zn_{1/2}Ga_{1/2}O$, (ZGO); (2) Zn^{2+} located at the tetrahedron site of $ZnCr_2O_4$ was replaced by Ga^{3+}, denoted as $ZnCr_{16/7}Ga_{1/7}O_{34/7}$, (ZG); (3) Cr^{3+} located at the octahedral site of $ZnCr_2O_4$ was replaced by Ga^{3+}, denoted as $ZnCr_{15/8}Ga_{1/8}O_4$, (CG); (4) Ga^{3+} located at the vacancies in the bulk of $ZnCr_2O_4$. In addition, the possibility of ZGO, ZG, CG, and $ZnGa_2O_4$ formation through ZnO, γ- Ga_2O_3 , Cr_2O_3, and $ZnCr_2O_4$ were also calculated to explore the possible origins of $ZnGa_2O_4$, or Ga adopted ZnCr spinel. The detailed reactions that fall our consideration are listed in Table 3.1.

The binding energy E_B is calculated by the following expression to test the phase stability of Ga adopted ZnCr oxide: a larger E_B indicates that the structure is most likely to exist and be stable, that is :

$E_B = \sum E_{atom} n_{atom} - E_t$

where E_t is the total energy of the constructed crystal lattice, E_{atom} is the total energy of isolated atom (Zn, Cr, Ga, and O, respectively) in vacuum, n_{atom} is the number of the atom that composed the crystal [36, 37]. The formation energies were calculated based on the most stable oxides phases as references states according to David A. Andersson et al ‘s strategy [38].

3.2.5.2 Adsorption of Ga on(311), (310), and (202) surfaces of $ZnCr_2O_4$

The (311), (310) and (202) surfaces of $ZnCr_2O_4$ were obtained by cutting the respective surfaces of the optimized $ZnCr_2O_4$ spinel. Among all these surfaces, tri-coordinated oxygen atoms were chosen as the preferred adsorption sites, other coordination unsaturated atoms such as Zn and Cr on the surface are fall out of our investigation owing to the fact that the electronegativity of these two atoms are much smaller than atom O. K-point grid method for the three surfaces are 3×4×1 for (311) surface, 3×2×1 for (310) surface and 2×2×1 for (202) surface respectively, which was applied to sample the Brillouin zone.

3.3 Results and discussion

3.3.1 The BET surface areas of the catalysts

The textural parameters of the reduced K-Ga_XZnCr catalysts are listed in Table 3.2. As shown, the BET areas of the samples regularly changed with the addition of Ga^{3+}, that is 63.86 m^2/g for KGa_0ZnCr, 78.43 m^2/g for K-$Ga_{0.55}$ZnCr, 75.96 m^2/g for K-$Ga_{1.10}$ZnCr, 66.54 m^2/g for K-$Ga_{1.64}$ZnCr and 61.71 m^2/g for K-$Ga_{2.18}$ZnCr, respectively. This phenomenon is also observed when investigating the external surface area. However, as for the change of average pore diameter and its distributions (Fig. 3.1), one can see that the smaller pores were created by Ga^{3+} addition, which is in accordance with the study of Hyungwon Ham et al. and A Rong Kim et al. who discovered an increased surface area and decreased pore diameter when Ga was added in to Cu/m-Al_2O_3 catalyst or CuO-Cr_2O_3 water gas shift reaction catalyst [26, 29]. With the increase in the BET area, more active sites were created. Therefore a superior performance of

catalyst will be expected from the catalyst. The change in the catalyst texture may be caused by the interaction between Ga species and ZnCr oxides which alteres the morphology of the catalyst. The exact images of the Ga^{3+} doped catalyst are further characterized using HR-TEM in the following section.

3.3.2 HR-TEM characterization

The HR-TEM images of the K- ZnCr catalyst with and without Ga modification are shown in Fig. 3.2 and Fig. 3.3. When comparing the images of the two samples, one can see that after adding Ga^{3+} to K- ZnCr catalyst, the particles become smaller. As shown in the histogram, the particle size of K-Ga_0ZnCr sample is mostly in the range of 5.5 to 6.5 nm, while for K-$Ga_{1.10}$ZnCr sample, the particle is in the range of 4.5 to 6.5 nm with a uniform distribution. The average particle size decreased from 6.98 nm to 6.11 nm after Ga^{3+} introduction, implying that the microstructure of K-ZnCr catalyst was altered by Ga^{3+} addition, which is also observed for Ga doped CoZnAl catalyst [22]. When considering the exposed surface of K-ZnCr catalyst with or without Ga addition, one can see that the (311), (310) and (202) surfaces of $ZnCr_2O_4$ are the most exposed surfaces after Ga modification. The alteration of the particle sizes and distributions of crystal surface caused by Ga addition may be attributed to the interaction between Ga^{3+} and ZnCr oxides or the interactions between Ga cluster and ZnCr oxides. The explicit form of the Ga^{3+} doped species was verified by XPS analysis and DFT calculation in the following section. In addition, although the the change in particle sizes is in accordance with the observation of BET test, HR-TEM images only

gives part of the morphologies of the catalyst samples, the exact particle sizes of K-Ga_xZnCr samples should be analysed by characterizing the bulk structure of the samples, which will be investigated by analysing the XRD patterns in the subsequent section.

3.3.3 XRD characterization

The XRD patterns of catalyst samples with different addition amount of Ga^{3+} were shown in Fig. 3.4. As shown, all the K-Ga_xZnCr catalysts presented the diffraction peaks that were assigned to ZnO and $ZnCr_2O_4$, and no new peaks were observed when Ga^{3+} was introduced, implying the high dispersion of the Ga^{3+} compounds. The particle size of the (310) surfaces of $ZnCr_2O_4$ was calculated using the Scherrer equation and are listed in Fig.3.4A. As can be seen, the $ZnCr_2O_4$ particles become much smaller when Ga^{3+} is introduced. This trend is in accordance with the observations from HR-TEM analysis. In addition, to give a better understanding of the impact of Ga^{3+} to ZnO and $ZnCr_2O_4$, a Rietveld refinement was performed using MUAD software [39-42]. The results of the refinement are shown in Fig. 3.5. The mass fractions of ZnO and $ZnCr_2O_4$ according to the refinement were listed in Table s1. As shown, the weight fraction of $ZnCr_2O_4$ increase with increasing amount of Ga^{3+}, while this trend is opposite for ZnO, indicating that the composition of the K-ZnCr catalyst was altered by the introduction of Ga^{3+}. Furthermore, after 48 hours of time-on-stream, it can be observed from the corresponding catalysts that the diffraction peaks of both ZnO and $ZnCr_2O_4$ were intensified (Fig. 3.4B), implying the growth of particle size of these two species during

the reaction. Gao et al. illustrated that the configurations and adsorption energy of CO can be altered by the morphology of ZnO owing to its different interactions with $ZnCr_2O_4$ (111) surface [12]. Based on this discovery, we may deduce that the interaction between ZnO and $ZnCr_2O_4$ can be altered by the addition of Ga^{3+}. This may be caused by the interaction between Ga and $ZnCr_2O_4$, or the formation of other compounds such as $ZnGa_2O_4$ through the respective oxides of gallium, chromium and zinc. In the following section, a thermodynamic calculation was performed to verify the possible transformation process of the Ga species.

3.3.4 The possible locations of Ga^{3+} calculated by DFT

To deduce the possible locations of Ga^{3+} in K-ZnCr iso-butanol catalyst, a thermodynamic calculation was performed. When considering interactions between Ga^{3+} and ZnCr oxides, the following compounds can be formed. (ⅰ) gallium oxide (ⅱ) Ga^{3+} doped ZnO (ZGO) (ⅲ) one of the metals in $ZnCr_2O_4$ is replaced by Ga^{3+} to form a four coordination or six coordination spinel; and (ⅳ) $ZnGa_2O_4$. DFT calculations were performed to deduce the possible locations of Ga^3. If Zn^{2+} located at the tetrahedral coordination sites in ZnO and $ZnCr_2O_4$ were replaced by Ga^{3+}, the reduced cell parameters of *a* and *c* would be expected owing to the smaller ionic radius (0.47 Å for Ga^{3+} vs. 0.6 Å for Zn^{2+}). A similar deduction can also be expected if Cr^{3+} located at the six coordinated sites of $ZnCr_2O_4$ was replaced by Ga^{3+}(0.74 Å for Cr^{3+} vs. 0.62 Å for Ga^{3+}). However, an adverse consequence was obtained here (Table 3.3). The differences in the cell parameter *c* of $ZnCr_2O_4$ between speculation and the results

of Rietveld may be originated from the cation disordered ZnCr spinel. To further deduce the location of Ga^{3+}, binding energy E_B and formation energy E_f were calculated based on the optimized structure by DFT calculation. The configuration of the possible Ga^{3+} doped species and the reaction were shown in Table 3.1 and Fig.3.6. As shown in Table 3.1, E_B of these compounds follows the order below: ZG > $ZnCr_2O_4$ > $ZnGa_2O_4$ > CG > ZGO > ZnO, implying that ZG is the most stable Ga^{3+} doped ZnCr compound. When Ga^{3+} was added into a ZnCr catalyst, ZG may be one of the most possible existent forms of Ga species, rather than ZGO and CG, owing to its higher stability.

In addition to the doping of Ga^{3+} in $ZnCr_2O_4$, other structures may be formed. For example, the unsaturated sites of the $ZnCr_2O_4$ surfaces were coordinated by Ga^{3+} or clusters of Ga species. To verify this speculation, the adsorption of Ga on the most proposed surfaces of $ZnCr_2O_4$ such as (311), (310) and (202) (obtained through HR-TEM) were calculated. Based on the observation and speculation, the interaction between Ga and $ZnCr_2O_4$ was investigated by calculating the adsorption of Ga on the coordination unsaturated sites of the surfaces. The most stable adsorption configurations were listed in Fig.3.7. Bader charge distributions before and after Ga adsorption are also listed in the Table 3.4. As shown, all the surfaces accept electrons from Ga, the trend is 310 (0.2940) < 311 (0.4092) < 202 (0.7449). Generally, CO is rich in electron, a stronger adsorption of CO will be created if the surface is electron deficient. Therefore, a reverse CO adsorption could be expected. The calculated adsorption energies and configurations of CO (Table 3.5 and Fig. 3.8) support this conjecture.

Furthermore, except for the above observed surfaces, there may be lots of possible step surfaces owing to the fact that the surfaces of the particles are very uneven, which could be attributed to the other reaction sites for CO hydrogenation. To better analyses the structure and their effects on syngas conversion, more detailed characterization and computational work should be carried out. Owing to the complexity of the catalyst surface, these configurations are not easy to investigate using DFT calculations. Therefore the DFT calculation shown above gives only part of the functions of the particular structure. However, this approach could be used as a simplified method to study the real surface. In future studies, we will attempt to investigate the structure and function of these step surfaces.

3.3.5 Raman analysis to K-Ga_xZnCr catalysts

Raman peaks for the reduced K-Ga_xZnCr samples with an excitation wavelength of 532 nm were shown in Fig. 3.9. The peaks located at 392 and 900 cm^{-1} are the characteristic bands for the normal vibration modes of ZnO and Cr atoms in the tetrahedral and octahedral sites formed by the oxygen atoms [43]. The peaks located at 511 and 605 cm^{-1} represent the vibration of F_{2g} for $ZnCr_2O_4$ and 680 cm^{-1} is assigned to the symmetric Cr-O stretching vibration of the A_{1g} symmetry originating from the CrO_6 groups of spinel [44, 45]. The bands presented at 846 cm^{-1}, 867 cm^{-1} and 933 cm^{-1} are ascribed to the Cr=O stretching vibration in the chromate compound [44]. The peak located at 350 cm^{-1} belongs to the vibration mode associated with the multiple-phonon scattering processes of ZnO [46]. Based on the observation, one can see that

the vibration of ZnO, $ZnCr_2O_4$ and chromate were all weakened after the introduction of Ga^{3+}. Furthermore, for all the samples, the peaks located at 770 and 500 cm^{-1}, corresponding to the asymmetric stretching of Ga-O bond in the tetrahedral sites, show almost the same intensity with an enhanced amount of Ga^{3+} [47]. However, the typical Raman vibration mode that is ascribed to β-Ga_2O_3 was not observed [47]. Moreover, the peaks at 601 cm^{-1} and 712 cm^{-1} that were assigned to the T_{2g} and A_{1g} modes of $ZnGa_2O_4$ was intensified by increasing the amount of Ga^{3+} [48]. This may be the consequence of the interactions between ZnCr oxides with Ga. With the gradual increase the amount of Ga^{3+}, the extra ZnO was reacted with Ga_2O_3 to form $ZnGa_2O_4$, Zn located in the tetrahedral site of $ZnCr_2O_4$ was partly replaced by Ga to form ZG structure which exhausted both ZnO and $ZnCr_2O_4$. In addition, by increasing the amount of Ga^{3+}, chromate was consumed so the intense absorption of chromate vanished. Based on the above mentioned analysis, we may speculate that when a small amount of Ga^{3+} is introduced into K-ZnCr catalyst, ZG is the dominate structure. However, when further increasing the amount of Ga^{3+}, the ZnO will react with Ga_2O_3 to form $ZnGa_2O_4$. The surface composition and properties were altered by the different forms of Ga^{3+} species, which need to be confirmed by XPS and chemisorption characterization.

3.3.6 Ultraviolet-visible diffuse reflectance spectra

An interesting phenomenon for the reduced catalysts samples is the change in the color of the catalyst, for example, K-Ga_0ZnCr is a blue-green, upon gradually

increasing the amount of Ga^{3+}, the color becomes increasingly darker. This change was verified by ultraviolet visible diffuse reflectance analysis. As shown in Fig. 3.10, all the samples absorbed in the range of 200 ~ 800 nm, the absorbance of the samples was intensified by increasing the amount of Ga^{3+}. In addition, the diffuse reflectance spectrum gives evidence of the charge transfer of $O^{2-} \rightarrow Zn^{2+}$ in ZnO at 370 nm and in $ZnCr_2O_4$ at 300 nm [49]. The absorption band at 370 and 260 nm, attributed to $O^{2-} \rightarrow Cr^{6+}$ charge transfer, were also observed [49, 50]. With gradually increasing the amount of Ga^{3+}, the absorbance located at 300 nm become overlapped by the emergence of new peaks that located at 287 nm and 353 nm, indicating the formation of a new compound, which may be caused by the growth of ZG or Ga^{3+} coordinated on $ZnCr_2O_4$ surfaces.

Moreover, the indirect band gap energy E_g for the K-Ga_xZnCr samples are calculated using the equation $(\alpha h\nu)^2=C(h\nu-E_g)$ to investigate the influence of Ga addition on the electron structure of the catalysts [46, 51]. In the equation, α is the absorption coefficient, $h\nu$ is the photon energy with frequency ν, E_g is the indirect band gap energy, C is a constant. Fig. 3.11 shows the plot of $(\alpha h\nu)^2$ vs $h\nu$. The calculated indirect band gap energies for the samples are 2.51 eV for K-Ga_0ZnCr, 2.49 eV for K-$Ga_{0.55}$ZnCr, 1.75 eV for K-$Ga_{1.10}$ZnCr, 2.07 eV for K-$Ga_{1.68}$ZnCr, and 2.03 eV for K-$Ga_{2.18}$ZnCr respectively, which indicates that when Ga was introduced into the K-ZnCr catalyst, the band gap was reduced. Hamid Tajizadegan et al. observed an E_g value of 1.8 eV for a nanoparticle of $ZnCr_2O_4$ with the particle size of about 17 nm [52]. C.P. Huang et al. discovered that the E_g of TiO_2 is size dependened, the band gap decreased

from 3.239 to 3.173 eV when the particle size decreased from 29 to 17 nm and then increased from 3.173 to 3.289 eV as the particle size decreased from 17 to 3.8 nm [53]. Based on the phenomenon and published research, we deduce that the lower E_g after Ga addition may be caused by the smaller particle size of $ZnCr_2O_4$ observed through TEM and XRD. In addition, the coordination of Ga on the exposed oxygen of the $ZnCr_2O_4$ surfaces or the formation of ZG may be another reason that caused the reduced E_g owing to the fact that Ga can donate electrons to $ZnCr_2O_4$

3.3.7 Analysis of the surface composition of K-Ga_xZnCr by XPS spectra

The XPS spectra were investigated to disclose the structure evolution process of the K-ZnCr catalyst promoted by Ga^{3+}. The Cr $2p_{3/2}$ and Cr $2p_{1/2}$ spectra of all the samples are listed in Fig. 3.12. Four peaks were obtained for each of the samples after deconvoluting the recorded peaks. The binding energy (BE) of 575.75- 574.86 eV is the characteristic peak for Cr metal [54], more specifically, 585.27-579.08 eV and 575.88-576.00 eV are the characteristic peaks of Cr^{3+} [8, 11] and 578.49-579.08 eV is the peak of Cr^{6+} [55]. Analysis of the concentration of surface chromium showed that the main composition of surface chromium is Cr^{3+}, the amount of metallic Cr and Cr^{6+} species are only changed in the range of 5.32 % - 12.27% and 5.71 % - 21.21 %, respectively (Table 3.6), implying that the addition of Ga^{3+} has an obvious impact on the valence state of Cr. In addition, XPS spectra of Zn 2p is also performed. As is shown in Fig. 3.13, the BE values of 1020.46 - 1020.60eV and 1043.57 - 1043.68 eV are the characteristic of Zn $2p_{1/2}$ and Zn $2p_{3/2}$, respectively [45, 56, 57]. The BE of Zn 2p was

barely changed with the altered concentration of Ga^{3+}, indicating the similar chemical environment of Zn with and without the introduction of Ga^{3+} promoter. To further explore the influence of Ga^{3+} addition on the composition of the K-GaZnCr catalyst, XPS analysis of Ga 2p and Ga 3d were performed, and are shown in Fig. 3.14. The BE at 1116.23 - 1117.27 eV is the characteristic peak of $Ga2p_{3/2}$, 1443.06 - 1143.20 eV is the characteristic peak of $Ga2p_{1/2}$ [57]. These values are much smaller than the peaks in K-$ZnGa_2O_4$ and Ga_2O_3 (Fig. 3.15), indicating the chemical environment is quite different from pure Ga_2O_3 and K-$ZnGa_2O_4$. In addition, it is obvious that the BE of Ga $2p_{1/2}$ increased from 1143.06 eV (K-$Ga_{1.10}$ZnCr) to 1143.20 eV (K-$Ga_{2.18}$ZnCr) upon an enhancement the amount of Ga^{3+}, suggesting the chemical environment of Ga^{3+} was altered by the amount of its usage. To further study the coordination states of Ga^{3+} on the K-GaZnCr catalyst, the $Ga2p_{3/2}$ peaks were deconvoluted into two peaks, the results are shown in Fig. 3.14D. It can be seen that the Ga^{3+} ions occupy two different coordination sites in K-GaZnCr: peaks located at 1116-1117 eV, which can be assigned to Ga^{3+} at the tetrahedral sites [58-60], and peak at 1117.1-1117.6 eV can be assigned to Ga^{3+} located at the octahedral sites. In addition, for K-$Ga_{1.10}$ZnCr, the Ga^{3+} located at the tetrahedral sites reaches the maximum value, 74.31%. Another interesting finding is the assignment of $Ga2p_{1/2}$ shown in 1143.06-1143.20 eV. According to Pierre Delichere et al. the $Ga2p_{1/2}$ for $ZnGa_2O_4$ is located at 1144.3 eV, while for Ga_2O_3 it is 1144.15 eV [47, 56, 58, 61]. The decreased BE of $Ga2p_{1/2}$ may be caused by the formation of the ZG structure or the coordination of the Ga cluster on the surface of $ZnCr_2O_4$, because the electronegativity of Zn and Cr are smaller than that of Ga [62].

From the above analysis, no remarkable peaks corresponding to Ga_2O_3 were observed owing to the mismatched peaks of Ga $_{2p3/2}$ and Ga $_{2p1/2}$ spectrum for the Ga_2O_3 samples. To further confirm the existing form of Ga^{3+}, the 3d spectra of Ga was performed and the results are shown in Fig. 3.144 E-H. According to W. Yang et al. [63], Ga is mainly located at the tetrahedral (BE around 21.62) and octahedral sites(BE around 19.93 eV) for all the catalyst samples. The amount of six-coordinated Ga decreased gradually with the increasing amount of Ga addition (from 32.53 % for K-$Ga_{0.55}$ZnCr to 22.71 % for K-$Ga_{2.18}$ZnCr, Table 3.7), and the amount of four-coordinated Ga shows a reversible trend, indicating that different forms of gallium species were formed with different amounts of added Ga^{3+}. This trend is in accordance with the observation of Ga 2p spectra. In addition to the peaks that denote to Ga located at different coordination sites, peaks located at 16.94 to 17.06 eV and 23.37 to 23.85 eV were also observed. The former may be caused by the formation of ZG, while the latter may be the result of gallium clusters or the coordination of Ga to the unsaturated $ZnCr_2O_4$ surfaces.

By fitting the XPS spectrum of Cr 2p, Zn 2p and Ga 2p, the surface concentration of these elementary were calculated. As a comparison, the compositions of bulk catalysts were also investigated by XRF analysis. The results are shown in Table 3.8, the molar ratios of Zn/Cr in the bulk for each catalyst are in the range of 0.89 to 0.91, which is smaller than the feed rate. However, on the surface of the catalysts, a remarkable enhancement of Zn was observed. Furthermore, when comparing the rations of Zn/Ga and Cr/Ga for the bulk and surface, an enhancement of Ga was

observed. The enhancement of Zn and Ga on the surface of the catalyst may be ascribed to the interaction of Ga^{3+} with $ZnCr_2O_4$ as discussed in the above section.

To further investigate the structural evolution caused by Ga^{3+} addition, especially the surface oxygen species over Ga promoted catalysts, the O1s XPS spectra of the catalysts were recorded. As shown in Fig. 3.16 and Table 3.9, the surface oxygen species are mainly composed by lattice oxygen (O_{latt}) located at 529.5 eV, surface absorbed oxygen (O_{ads}) located at 531.1 eV and absorbed OH groups located at 532 eV [8]. O_{ads} and O_{OH} created by the disordered ZnCr catalyst are considered to be the active sites for CO activation and these are advantageous to the formation of formate group, which is an important C_1 precursor to form C_2 oxygenates. Therefore, the higher the concentration of O_{ads} and O_{OH}, the better performance of K-ZnCr catalyst could be expected. As listed in Table 3.9, the molar ratio of $(O_{ads} + O_{OH})/(O_{latt} + O_{ads} + O_{OH})$ ranged from 36.72 % to 46.94 %. In addition, the proportion of absorbed OH groups show irregular change upon increasing the amount of Ga^{3+}, which may be caused by the deduced particle size or the altered interactions between ZnO and $ZnCr_2O_4$. Furthermore, the amount of Ga cluster, ZG and $ZnGa_2O_4$ also changed with the amount of Ga added. This will also influence the basicity and acidity of the catalysts, which is very important for CO activation and iso-butanol formation. The detailed basicity-acidity information about K-GaZnCr catalyst was investigated using CO_2 and NH_3 TPD and is reported in the following section.

3.3.8 CO_2-TPD analysis to the basicity of the catalysts samples

In this section, the basicity of K-GaZnCr iso-butanol catalysts was tested using a CO_2-TPD study, and the results are shown in Fig. 3.17. As can be seen from Fig. 3.17, all the samples show a remarkable desorption of CO_2 at 170-204 ^oC, 260-288 ^oC, 350-367 ^oC, 440-484 ^oC and above 600 ^oC, respectively, corresponding to different basicity of the catalysts, that is weak basicity, medium basicity and strong basicity. The CO_2-TPD results demonstrated that ratios of weak basicity to strong basicity and medium basicity are in the range 0.57 -0.47 and 0.64 - 0.76 for K-Ga_xZnCr (x=0.0, 0.55, 1.10, and 1.64) and a sharp increase for K-$Ga_{2.18}$ZnCr (0.68 and 1.25), indicating that an excessive amount of Ga^{3+} is harmful to the density of weak basicity site, but is advantageous to the density of the medium and strong basicity sites, especially to the strong basicity sites. Generally, moderate basicity is important for the carbon chain growth through β-addition during the synthesis higher alcohol [14, 17, 64]. If the basicity of the catalyst is too strong, the adsorption of the unsaturated precursors for branched carbon chain growth, for example, propanol or/and formyl group, is so strong that the formation of higher branched carbon chain cloud not take place [5, 15, 16].

3.3.9 NH_3-TPD analysis of the catalysts

Fig. 3.18 shows the NH_3-TPD profiles of the K-Ga_xZnCr samples. As shown, all the samples give two major peaks that can be assigned to the weak acidity (around 210 ^oC) and medium-strong acidity (300 – 600 ^oC). The profiles were fitted into five peaks to further investigate the detailed distribution of acidity. According to the NH_3-TPD profiles, the ratios of weak acidity to medium-strong acidity increased with the

increasing amount of Ga^{3+} promoter. As for the medium-strong acidity, K-$Ga_{1.10}$ZnCr shows an identical ratio of medium acidity to strong acidity. The proper ratios of weak to medium-strong acidity and medium to strong acidity play a major part in inactivating CO and boosting the carbon chain growth during synthesis of higher alcohols [1]. In general, the strong acidity is beneficial to the dissociative adsorption of CO, while the weak and medium acidity contribute to the molecularly adsorption of CO [65]. Therefore, the moderate acidity is a key role in syngas conversion.

3.3.10 DRIFTs of CO adsorption on K-Ga_xZnCr catalysts

The adsorption of CO was performed using in situ diffuse reflectance infrared Fourier transform spectroscopy (DRIFTs) at 400 ºC after H_2 reduction of the K-Ga_xZnCr catalysts. As is shown in Fig. 3.19, all samples give the absorption of carbonates located at 1045 cm^{-1}, 1310 cm^{-1} and 1560 cm^{-1} and the absorption of formates located at 1590 cm^{-1}, 1610 cm^{-1} respectively [30, 66, 67]. Moreover, the anti-symmetric stretching vibration of CO_2^- and symmetric stretching vibration of CH located at 2955 cm^{-1}, 2865 cm^{-1}, 2745 cm^{-1} were also observed [67]. By comparing the intensity of formate and carbonates located at 1590 cm^{-1}, 1607 cm^{-1}, 1045 cm^{-1} and 1033 cm^{-1}, one can see that K-$Ga_{0.55}$ZnCr and K-$Ga_{1.10}$ZnCr give a much stronger absorption than the other three samples, indicating that more active sites exist on these two samples. Formate is an important processor of C_1 intermediate CHO for the growth of C-C chain, meanwhile it is also the processor for forming OCH_3 group which is the key intermediate to produce methanol [68]. As a result, the higher concentration of

formate, the higher space time yield (STY) of alcohols that can be expected.

3.3.11 The performance of K-GaZnCr catalysts

The typical catalytic performance of K-Ga_xZnCr catalysts are listed in Table 3.10. All the evaluation results for the catalysts were collected after 22 hours of time on stream in order to minimize the influence of the disturbance by frequent sampling. As can be seen in Table 3.10, by gradually increasing the amount of Ga^{3+}, the selectivity of CO_2 was decreased from 42.55% for K-Ga_0ZnCr to 34.64 % for K-$Ga_{1.10}$ZnCr, while the selectivity of alcohols was increased from 51.50 % to 59.03%. In addition, when the amount of Ga^{3+} is lower than 1.64%, the selectivity of methanol and iso-butanol are higher than 57.00 wt% and 31.00 wt%, respectively. Upon further increasing the amount of Ga^{3+}, the isobutanol selectivity in the total alcohols was reduced to only 23.21 wt%, while methanol (69.44 wt%) turned out to be the major composition of the alcohols. The amount of CH_x and DME were also increased sharply under a higher doping concentration of Ga^{3+}. The evaluation results indicate that the higher concentration of Ga^{3+} has an adverse effect on the performance of iso-butanol catalyst, which may be attributed to the altered structure of the catalyst. In other words, the main composition of the catalyst is ZnO and $ZnCr_2O_4$ without adding Ga^{3+}. When Ga^{3+} was added, ZG or saturated $ZnCr_2O_4$ were formed. With the gradual addition of Ga^{3+}, the extra ZnO will react with Ga_2O_3 to form $ZnGa_2O_4$ during calcination. Furthermore, K-$ZnGa_2O_4$ sample was prepared to verify the structure of $ZnGa_2O_4$ and its catalytic performance. The evaluation results show that K-$ZnGa_2O_4$ is probably a DME synthesis

catalyst, and this was validated using a K-$Ga_{2.18}$ZnCr sample and only 2.43 % DME was obtained, which was much higher than that obtained using the other four catalysts. Thus, the increased amount of DME in K-$Ga_{2.18}$ZnCr indicates the formation of $ZnGa_2O_4$ species. Other possible reasons, such as the formation of Ga cluster, the interaction of Ga with the coordinately unsaturated $ZnCr_2O_4$ surface will result in the loss of performance of the K-ZnCr catalyst, which was verified by the reduced CO adsorption energy. Moreover, the well-performing K-$Ga_{1.10}$ZnCr catalyst was evaluated for a long-period stability test. The results are shown in Table 3.11. During 102 hours of time on stream, the selectivity of the total alcohol and the fraction of iso-butanol values were found to be above 59.00 % and 31.23 wt % respectively. The STY of the alcohols is in the range of 0.0875-0.1103 g h^{-1} g cat^{-1}, which indicates that the K-$Ga_{1.10}$ZnCr catalyst exhibits a good stability during the reaction.

3.3.12 The effects of Ga^{3+} on the performance of K-ZnCr catalyst

In this section, we will further investigate the relationship between the structure of the Ga^{3+} doped catalysts and their performance. To begin with, the possible location of Ga^{3+} was deduced by calculating the E_B and E_f values, As shown in Table 3.1. The E_B values for $ZnCr_2O_4$, $ZnGa_2O_4$, ZG, CG, and ZGO follow the order: ZG (348.8783 eV) > $ZnCr_2O_4$ (334.9394 eV) > $ZnGa_2O_4$ (309.8619 eV) > CG (250.3525 eV) > ZGO (19.1836 eV), suggesting that ZG and $ZnCr_2O_4$ are more stable than the other compounds. In addition, the E_r value calculated using their most stable oxides follow the order: $ZnCr_2O_4$ (254.7572 eV) > ZG (243.7237eV) > $ZnGa_2O_4$ (229.6797 eV) >

CG (162.7697 eV), indicating that $ZnCr_2O_4$ and ZG are easier to form through their oxides. As suggested by Y Li et al., E_r determines the driving force of a formation reaction, a larger E_r will lead to the formation of a more stable compound [36]. By combination the *Er* with the E_B, we deduced that the most stable form of the Ga^{3+} doped ZnCr spinel is ZG. The detailed configuration of ZG is shown in Fig. 3.6. The cell parameters of *a, b*, and *c* for ZG are 8.3490, 8.3466, and 8.3495 Å, respectively, which are larger than the un-doped ZnCr spinel (a = 8.2300 Å, b = 8.2302 Å, c = 8.32304 Å). The calculated cell parameters are larger than the values that were deduced from the ionic radius of tetrahedral coordinated Zn^{2+} and Ga^{3+} (their radius are 0.74 Å and 0. 61 Å, respectively [69]). The difference may be caused by the higher valance of Ga^{3+}. When Zn^{2+} is partly replaced by Ga^{3+}, excessive positive charges need to be neutralized to remain electrically neutral meaning that re-distributions of all cations can be expected which will induce enlarged cell parameter. Furthermore, when Ga^{3+} was embed in the tetrahedral site of the ZnCr spinel, the Ga-O bond is only about 1.89 Å, which is much shorter than the Ga-O bond located in Ga_2O_3 crystal (1.94 to 2.10 Å). The calculated Bader charge distribution of Ga for Ga_2O_3, $ZnGa_2O_4$, and ZG are +1.87, +1.83, and +1.77, respectively, suggesting that the electron density of Ga in ZG is higher than the other gallium compounds which may explain the lower BE of Ga 2p in the XPS patterns for the K-GaZnCr catalysts.

Secondly, when ZG was formed, the surface composition of the catalyst was altered. The altered surface composition significantly affected the interaction between ZnO and $ZnCr_2O_4$ which will further impact the ratio of Zn/Cr, and the basicity and

acidity of the catalysts. To determine the different surface properties between $ZnCr_2O_4$ and ZG, the $ZnCr_2O_4$ (111) and ZG (111) surfaces were constructed, the adsorption of CO, H_2, H_2O and CO_2 were investigated using DFT calculation. The most stable configurations and adsorption energies of the species are shown in Fig. 3.20-Fig.3.23 and Table 3.12. The results show that Cr is the most favorable adsorption site (Fig. 3.21) for CO absorption on both $ZnCr_2O_4$ (111) and ZG (111) surfaces. The adsorption energies are -0.74 eV and -2.99 eV respectively, which indicate that Ga^{3+} adoption is helpful to the adsorption of CO. In addition, remarkable decreased adsorption energies of CO_2 and H_2O on the ZG (111) surface were also observed (Tabel 3.12), suggesting that CO_2 and H_2O are not favorable for adsorption on the ZG (111) surface. During syngas conversion, water gas shift reaction (WGSR) is an inevitable reaction that consumes a large amount of CO thus reduces the efficiency of carbon resource usage. Hence, it is important to reduce or suppress this reaction. The smaller adsorption energy of H_2O indicates that it is not easy for H_2O to participate in WGSR to produce CO_2. This is firmly verified by the evaluation results of K-Ga_xZnCr catalyst.

Thirdly, the productivity of hydrocarbons such as ethane and propane increased with the increasing amount of Ga^{3+}, that is form 2.95 % for K-$Ga_{0.0}$ZnCr to 19.96 % for K-$Ga_{2.18}$ZnCr. Although D. S. Cryder et al. proposed that the excess of surface chromium oxides gives rise to the amount of CO_2 and hydrocarbons [70], we conclude that the hydrocarbons in gas product are mainly caused by the presence of the ZG compound. The reason for this lies in the following two aspects: (ⅰ) the ratios of Zn/Cr on the surface of the samples are almost the same for K-Ga_xZnCr (x=0, 0.55, 1.10, 1.64,

and 2.18) samples, as detected by XPS, therefore the effects of extra chromium on the selectivity of the hydrocarbons can be excluded. (ii) CO is easier to dissociate on ZG (111) surface than on the $ZnCr_2O_4$ (111) surface, which can be verified using the CI-NEB calculation on the elementary reaction CO = C + O. The results show that the activation energy for CO dissociation is 3.32 eV lower on the ZG (111) surface than on the $ZnCr_2O_4$ (111) surface (shown in Fig. 3.24 A). The dissociated CO is considered to be the origin of the CH_x species, leading to the formation of hydrocarbons on the samples with a higher amount of added Ga^{3+}.

Finally, the formation of CHO by CO hydrogenation was also studied on the different catalyst surfaces to investigate the influence of surface structure on the CHO formation. CHO is regarded as an important intermediate to participate in the formation of the first C_2 oxygenates, which is the rate determing step for higher alcohol synthesis. In addition, CHO is also the precursor of the OCH_3 group, and then by step by hydrogenation, methanol will be produced. Therefore, the higher the concentration of CHO, the higher the selectivity of alcohol is expected. Lower values for the activation energy and reaction energy were obtained using DFT calculation, for example 0.96 eV and 0.24 eV on ZnCr spinel (111) surface *versus* 0.78 eV and -1.05 eV on ZG(111) surface (Fig. 3.24 B). The reduced activation energy and reaction energy for CHO formation indicate that Ga^{3+} adsorption is advantageous to the formation of CHO, which will further boost the selectivity of alcohols.

3.4 Conclusions

Ga^{3+} promoted K-ZnCr catalysts were prepared using the precipitation-impregnation method. The optimal K-$Ga_{1.10}$ZnCr catalyst shows a 58.70 % increase in the space time yield and 14.62 % promotion on the selectivity of the alcohols under the reaction conditions of 10.0 MPa, 400 ^{o}C and 3300 h^{-1} GHSV. Spectral analysis and first principle calculations revealed that Zn^{2+} ions, located at the tetrahedral site of the ZnCr spinel, were replaced by Ga^{3+} ions to form the ZG structure, which promoted the direct dissociation of CO and the formation of the CHO group. The Coordinately unsaturated $ZnCr_2O_4$ surfaces interacted with Ga or gallium clusters which reduced the adsorption of CO along with this process. However, upon further increasing the amount of Ga^{3+}, $ZnGa_2O_4$ was formed which would modulate the morphologies, surface acidity and basicity of the final catalysts, eventually inducing poor performance of the catalysts.

References

[1] M. Ao, G.H. Pham, J. Sunarso, M.O. Tade, S. Liu, Active Centers of Catalysts for Higher Alcohol Synthesis from Syngas: A Review, ACS Catalysis, 8 (2018) 7025-7050.

[2] H. Guo, S. Li, H. Zhang, F. Peng, L. Xiong, J. Yang, C. Wang, X. Chen, Y. Chen, Reaction Condition Optimization and Lumped Kinetics Study for Lower Alcohols Synthesis from Syngas Using a Two-Stage Bed Catalyst Combination System, Industrial & Engineering Chemistry Research, 53 (2014) 123-131.

[3] K.A.N. Verkerk, B. Jaeger, C.-H. Finkeldei, W. Keim, Recent developments in isobutanol synthesis from synthesis gas, Applied Catalysis A: General, 186 (1999) 407-

431.

[4] H.T. Luk, C. Mondelli, D.C. Ferre, J.A. Stewart, J. Perez-Ramirez, Status and prospects in higher alcohols synthesis from syngas, Chem. Soc. Rev., 46 (2017) 1358-1426.

[5] Y. Wu, N. Gong, M. Zhang, W. Zhang, T. Zhang, J. Zhang, L. Wang, H. Xie, Y. Tan, Insight into the branched alcohol formation mechanism on K-ZnCr catalysts from syngas, Catalysis Science & Technology, 9 (2019) 2592-2600.

[6] S. Gao, X. Li, Y. Li, H. Yu, F. Zhang, Y. Sun, H. Fang, X. Zhang, X. Liang, Y. Yuan, Effects of gallium as an additive on activated carbon-supported cobalt catalysts for the synthesis of higher alcohols from syngas, Fuel, 230 (2018) 194-201.

[7] S. Tian, L. Tan, Y. Wu, Y. Kou, H. Xie, N. Tsubaki, Y. Tan, The role of different state ZnO over non-stoichiometric Zn-Cr spinel catalysts for isobutanol synthesis from syngas, Applied Catalysis A General, 536 (2017) 57-66.

[8] S. Tian, S. Wang, Y. Wu, J. Gao, P. Wang, H. Xie, G. Yang, Y. Han, Y. Tan, The role of potassium promoter in isobutanol synthesis over Zn-Cr based catalysts, Catalysis Science & Technology, 6 (2016) 4105-4115.

[9] L. Tan, G. Yang, Y. Yoneyama, Y. Kou, Y. Tan, T. Vitidsant, N. Tsubaki, Iso-butanol direct synthesis from syngas over the alkali metalsmodified Cr/ZnO catalysts, Applied Catalysis A General, 505 (2015) 141-149.

[10] S. Tian, S. Wang, Y. Wu, J. Gao, Y. Bai, P. Wang, H. Xie, Y. Han, Y. Tan, Cation distribution in Zn-Cr spinel structure and its effects on synthesis of isobutanol from syngas: Structure-activity relationship, Journal of Molecular Catalysis A Chemical, 404

(2015) 139-147.

[11] X. Gao, Y. Wu, T. Zhang, L. Wang, X. Li, H. Xie, Y. Tan, Binary ZnO/Zn-Cr nanospinel catalysts prepared by a hydrothermal method for isobutanol synthesis from syngas, Catalysis Science & Technology, 8 (2018) 2975-2986.

[12] X. Gao, T. Zhang, Y. Wu, G. Yang, M.-H. Tan, L. Xiaoli, H. Xie, J. Pan, Y. Tan, Isobutanol synthesis from syngas on Zn-Cr based catalysts: New insights into the effect of morphology and facet of ZnO nanocrystal, Fuel, 217 (2018) 21-30.

[13] L. Wang, X. Gao, Y. Bai, M. Tan, K. Sun, T. Zhang, Y. Wu, J. Pan, H. Xie, Y. Tan, The synergistic effect between ZnO and $ZnCr_2O_4$ on the catalytic performance for isobutanol synthesis from syngas, Fuel, 253 (2019) 1570-1577.

[14] K.J. Smith, R.B. Anderson, A chain growth scheme for the higher alcohols synthesis, Journal of Catalysis, 85 (1984) 428-436.

[15] L. Lietti, P. Forzatti, E. Tronconi, I. Pasquon, Temperature-programmed reaction of C_4 oxygenates on unpromoted and K-promoted ZnCr oxide in relation to the mechanism of the higher alcohol synthesis, Journal of Catalysis, 126 (1990) 401-420.

[16] L. Lietti, E. Tronconi, P. Forzatti, Mechanistic aspects of the higher alcohol synthesis over K_2O-promoted ZnCr oxide: Temperature-programmed reaction and flow experiments of C_3, C_4, and C_5 oxygenates, Journal of Catalysis, 135 (1992) 400-419.

[17] Y. Wu, H. Xie, Y. Kou, N. Tsubaki, Y. Han, Y. Tan, The mechanism of higher alcohol formation on ZrO2-based catalyst from syngas, Korean Journal of Chemical Engineering, 32 (2015) 406-412.

[18] W.S. Epling, G.B. Hoflund, D.M. Minahan, Higher alcohol synthesis reaction

study VI: effect of Cr replacement by Mn on the performance of Cs- and Cs, Pd-promoted Zn Cr spinel catalysts, Applied Catalysis A General, 183 (1999) 335-343.

[19] D.M. Minahan, W.S. Epling, G.B. Hoflund, Reaction and Surface Characterization Study of Higher Alcohol Synthesis Catalysts: IX. Pd- and Alkali-Promoted Zn/Cr-Based Spinels Containing Excess ZnO, Journal of Catalysis, 179 (1998) 241-257.

[20] W.S. Epling, G.B. Hoflund, D.M. Minahan, Reaction and Surface Characterization Study of Higher Alcohol Synthesis Catalysts: VII. Cs and Pd Promoted 1:1 Zn/Cr Spinel, Journal of Catalysis, 175 (1998) 175-184.

[21] W.S. Epling, G.B. Hoflund, D.M. Minahan, Reaction and surface characterization study of Zn/Cr-based higher-alcohol synthesis catalysts X: Effects of excess promoter loading on surface chemistry, Reaction Kinetics and Catalysis Letters, 67 (1999) 225-232.

[22] Z. An, X. Ning, J. He, Ga-promoted CO insertion and C-C coupling on Co catalysts for the synthesis of ethanol and higher alcohols from syngas, Journal of Catalysis, 356 (2017) 157-164.

[23] A. Venugopal, J. Palgunadi, J.K. Deog, O. S. Joo, C. H. Shin, Dimethyl ether synthesis on the admixed catalysts of Cu-Zn-Al-M (M=Ga, La, Y, Zr) and γ-Al_2O_3: The role of modifier, Journal of Molecular Catalysis A: Chemical, 302 (2009) 20-27.

[24] S. H. Kang, J. W. Bae, P.S.S. Prasad, J. H. Oh, K. W. Jun, S. L. Song, K. S. Min, Influence of Ga addition on the methanol synthesis activity of Cu/ZnO catalyst in the presence and absence of alumina, Journal of Industrial and Engineering Chemistry, 15 (2009) 665-669.

[25] K. Sun, Y. Wu, M. Tan, L. Wang, G. Yang, M. Zhang, W. Zhang, Y. Tan, Ethanol and higher alcohols synthesis from syngas over CuCoM (M=Fe, Cr, Ga and Al) nanoplates derived from hydrotalcite-loike precursors, ChemCatChem, 11 (2019) 2695-2706.

[26] A.R. Kim, B. Lee, M.J. Park, D.J. Moon, J.W. Bae, Catalytic performance on CuO-Cr_2O_3-Ga_2O_3 mixed oxides for water gas shift reaction: Effects of Ga/Cr molar ratio, Catalysis Communications, 19 (2012) 66-69.

[27] M. M. J. Li, Z. Zeng, F. Liao, X. Hong, S.C.E. Tsang, Enhanced CO_2 hydrogenation to methanol over CuZn nanoalloy in Ga modified Cu/ZnO catalysts, Journal of Catalysis, 343 (2016) 157-167.

[28] Y.-x. Pan, P. Kuai, Y. Liu, Q. Ge, C.-j. Liu, Promotion effects of Ga_2O_3 on CO_2 adsorption and conversion over a SiO_2-supported Ni catalyst, Energy & Environmental Science, 3 (2010) 1322-1325.

[29] H. Ham, S.W. Baek, C.-H. Shin, J.W. Bae, Roles of structural promoters for direct CO_2 hydrogenation to dimethyl ether over ordered mesoporous bifunctional Cu/M–Al_2O_3 (M = Ga or Zn), ACS Catalysis, 9 (2019) 679-690.

[30] T. Zhang, Y. Wu, X. Gao, H. Xie, G. Yang, N. Tsubaki, Y. Tan, Effects of surface hydroxyl groups induced by the co-precipitation temperature on the catalytic performance of direct synthesis of isobutanol from syngas, Fuel, 237 (2019) 1021-1028.

[31] D.A. Eustace, D.W. McComb, A.J. Craven, Probing magnetic order in EELS of chromite spinels using both multiple scattering (FEFF8.2) and DFT (WIEN2k), Micron, 41 (2010) 547-553.

[32] G. Kresse, J. Furthmuller, Efficient iterative schemes for ab initio total energy calculations using a plane-wave basis set, Physical Review B, 54 (1996) 11169-11186.

[33] G. Kresse, D. Joubert, From ultrasoft pseudopotentials to the projector augmented-wave method, Physical Review B, 59 (1999) 1758-1775.

[34] J.P. Perdew, K. Burke, M. Ernzerhof, Generalized gradient approximation made simple, Physical Review Letters, 77 (1996) 3865-3868.

[35] G. Henkelman, B.P. Uberuaga, H. Jonsson, A climbing image nudged elastic band method for finding saddle points and minimum energy paths, Journal of Chemical Physics, 113 (2000) 9901-9904.

[36] Y. Li, F. Lian, N. Chen, Z.-j. Hao, K.-c. Chou, Structural predictions based on the compositions of cathodic materials by first-principles calculations, International Journal of Minerals, Metallurgy, and Materials, 22 (2015) 524-529.

[37] D. Zhou, J. Liu, S. Xu, P. Peng, First-principles investigation of the binary intermetallics in Mg–Al–Sr alloy: Stability, elastic properties and electronic structure, Computational Materials Science, 86 (2014) 24-29.

[38] D.A. Andersson, C.R. Stanek, Mixing and non-stoichiometry in Fe-Ni-Cr-Zn-O spinel compounds: density functional theory calculations, Phys Chem Chem Phys, 15 (2013) 15550-15564.

[39] L. Lutterotti, M. Bortolotti, G. Ischia, I. Lonardelli, H.-R. Wenk, Rietveld Texture Analysis from Diffraction Images, Zeitschrift fur Kristallographie Supplements, 2007 (2007).

[40] L. Lutterotti, Total pattern fitting for the combined size–strain–stress–texture

determination in thin film diffraction, Nuclear Instruments and Methods in Physics Research Section B: Beam Interactions with Materials and Atoms, 268 (2010) 334-340.

[41] L. Lutterotti, D. Chateigner, S. Ferrari, J. Ricote, Texture, residual stress and structural analysis of thin films using a combined X-ray analysis, Thin Solid Films, 450 (2004) 34-41.

[42] L. Lutterotti, S. Matthies, H.R. Wenk, A.S. Schultz, J.W. Richardson, Combined texture and structure analysis of deformed limestone from time of flight neutron diffraction spectra, J. Appl. Phys., 81 (1997) 594-600.

[43] C. Vargas-Hernández, O. Almanza, J.F. Jurado, EPR, μ -Raman and Crystallographic properties of spinel type $ZnCr_2O_4$, Journal of Physics: Conference Series, 167 (2009) 012037.

[44] S. Tian, S. Wang, Y. Wu, J. Gao, Y. Bai, P. Wang, H. Xie, Y. Han, Y. Tan, Cation distribution in Zn–Cr spinel structure and its effects on synthesis of isobutanol from syngas: Structure–activity relationship, Journal of Molecular Catalysis A: Chemical, 404-405 (2015) 139-147.

[45] H. Song, D. Laudenschleger, J.J. Carey, H. Ruland, M. Nolan, M. Muhler, Spinel-structured $ZnCr_2O_4$ with excess Zn is the active ZnO/Cr_2O_3 catalyst for high-temperature methanol synthesis, ACS Catalysis, 7 (2017) 7610-7622.

[46] T. Pandiyarajan, M.L. Baesso, B. Karthikeyan, Enhanced ultraviolet-blue emission and Raman modes in $ZnO:Cr_2O_3$ composite nanoparticles, European Physical Journal D, 68 (2014).

[47] J. Wang, L. Ye, X. Wang, H. Zhang, L. Li, C. Kong, W. Li, High transmittance β-

Ga_2O_3 thin films deposited by magnetron sputtering and post-annealing for solar-blind ultraviolet photodetector, Journal of Alloys and Compounds, 803 (2019) 9-15.

[48] X. Lu, Z. Du, B. Quan, W. Bian, H. Zhu, Q. Zhang, Structural dependence of the microwave dielectric properties of Cr^{3+}-substituted $ZnGa_2O_4$ spinel ceramics: crystal distortion and vibration mode studies, Journal of Materials Chemistry C, 7 (2019) 8261-8268.

[49] C. Cristiani, P. Forzatti, M. Bellotto, Structural investigation on a spinel-related Zn/Cr = 1 mixed-oxide system, J. Chem. Soc., Faraday Trans. 1, 85 (1989).

[50] M.M. Can, G.H. Jaffari, S. Aksoy, S.I. Shah, T. Firat, Synthesis and characterization of $ZnGa_2O_4$ particles prepared by solid state reaction, Journal of Alloys and Compounds, 549 (2013) 303-307.

[51] R.S. Weber, Effect of Local Structure on the UV-Visible absorption edges of molybdenum oxide clusters and supported molybdenum oxides, Journal of Catalysis, 151 (1995) 470-474.

[52] H. Tajizadegan, A. Heidary, O. Torabi, M.H. Golabgir, A. Jamshidi, Synthesis and characterization of $ZnCr_2O_4$ nanospinel prepared via homogeneous precipitation using urea hydrolysis, International Journal of Applied Ceramic Technology, 13 (2015).

[53] H. Lin, C.P. Huang, W. Li, C. Ni, S.I. Shah, Y.-H. Tseng, Size dependency of nanocrystalline TiO_2 on its optical property and photocatalytic reactivity exemplified by 2-chlorophenol, Applied Catalysis B: Environmental, 68 (2006) 1-11.

[54] O. Nishimura, K. Yabe, M. Iwaki, X-ray photoelectron spectroscopy studies of high-dose nitrogen ion implanted-chromium: a possibility of a standard material for

chemical state analysis, Journal of Electron Spectroscopy and Related Phenomena, 49 (1989) 335-342.

[55] R. Merryfield, M. McDaniel, G. Parks, An XPS study of the Phillips Cr/silica polymerization catalyst, Journal of Catalysis, 77 (1982) 348-359.

[56] P. Delichere, S. Daniele, L.G. Hubert-Pfalzgraf, Surface Segregation Study of Transparent $ZnGa_2O_4$ Films by XPS, Surface Science Spectra, 8 (2001) 303-311.

[57] M. Chen, P. Wu, Q. Wei, Y. Zhu, S. Yang, L. Ju, N. Zhu, Z. Lin, The role of oxygen vacancy over ZnCr-layered double oxide in enhancing solar light-driven photocatalytic degradation of bisphenol A, Environmental Chemistry, 15 (2018) 226-235.

[58] H. Fan, G. Wang, L. Hu, Infrared, Raman and XPS spectroscopic studies of Bi_2O_3-B_2O_3-Ga_2O_3 glasses, Solid State Sciences, 11 (2009) 2065-2070.

[59] X. Duan, F. Yu, Y. Wu, Microstructure and optical properties of Co_xZn_1-xGa_2O_4 (0 <= x <= 1) nanoparticles, European Journal of Inorganic Chemistry, (2013) 1287-1293.

[60] N. Li, P. Zhu, X. Duan, Composition dependent cation distribution in $Zn_xGa_2O^{3+}_x$ nanocrystals, Physica B-Condensed Matter, 530 (2018) 290-294.

[61] C. Han, W. Mao, K. Bao, H. Xie, Z. Jia, L. Ye, Preparation of Ag/Ga_2O_3 nanofibers via electrospinning and enhanced photocatalytic hydrogen evolution, International Journal of Hydrogen Energy, 42 (2017) 19913-19919.

[62] N.C. Jeong, J.S. Lee, E.L. Tae, Y.J. Lee, K.B. Yoon, Acidity scale for metal oxides and sanderson's electronegativities of lanthanide elements, Angewandte Chemie International Edition, 47 (2008) 10128-10132.

[63] W. Yang, J. Li, X. Zhang, C. Zhang, X. Jiang, B. Liu, Hydrothermal approach to

spinel-type 2D metal oxide nanosheets, Inorganic Chemistry, 58 (2019) 549-556.

[64] T.J. Mazanec, On the mechanism of higher alcohol formation over metal oxide catalysts: I. a rationale for branching in the synthesis of higher alcohols from syngas, Journal of Catalysis, 98 (1986) 115-125.

[65] B.T. Loveless, C. Buda, M. Neurock, E. Iglesia, CO Chemisorption and dissociation at high coverages during CO hydrogenation on Ru catalysts, Journal of the American Chemical Society, 135 (2013) 6107-6121.

[66] M.D. Rhodes, K.A. Pokrovski, A.T. Bell, The effects of zirconia morphology on methanol synthesis from CO and H_2 over Cu/ZrO_2 catalysts: Part II. Transient-response infrared studies, Journal of Catalysis, 233 (2005) 210-220.

[67] A. Riva, A. Vaccari, L. Mintchev, G. Busca, Structure and reactivity of zinc chromium mixed oxides. Part 2. study of the surface reactivity by temperature programmed desorption of methanol, J. Chem. Soc., Faraday Trans. 1, 84 (1988).

[68] L.C. Grabow, M. Mavrikakis, Mechanism of methanol synthesis on Cu through CO_2 and CO hydrogenation, ACS Catalysis, 1 (2011) 365-384.

[69] J.U. Brehm, M. Winterer, H. Hahn, Synthesis and local structure of doped nanocrystalline zinc oxides, J. Appl. Phys., 100 (2006) 9.

[70] D.S. Cryder, P.K. Frolich, Catalysts for the formation of alcohols from carbon monoxide and hydrogen IV. Decomposition and synthesis of methanol by catalysts composed of zinc and chromium oxides, Industrial and Engineering Chemistry, 21 (1929) 867-871.

Table 3.1 The total energy E_t, binding energy E_B, and reaction energy E_r for GaZnCr related reactions.

species or reactions	energy, eV		
	E_t	E_B	E_f
Zn^{2+}	-0.1645		
Cr^{3+}	-5.4867		
O^{2-}	-0.0123		
Ga^{3+}	-0.3167		
$ZnCr_2O_4$	-424.4362		
Ga_2O_3	-184.7276		
Cr_2O_3	-84.3126		
ZnO	-18.2438		
ZG	-438.5273		
CG	-334.6796		
ZGO	-19.6894		
O_2	-9.8497		
$ZnGa_2O_4$	-316.6387		
(1). $8Zn^{2+} + 16Cr^{3+} + 32O^{2-} = ZnCr_2O_4$		334.9394	
(2). $8Zn^{2+} + 16Ga^{3+} + 32O^{2-} = ZnGa_2O_4$		309.8619	
(3). $2Zn^{2+} + 2O^{2-} = ZnO$		17.8902	
(4). $4Cr^{3+} + 6O^{2-} = Cr_2O_3$		62.2920	
(5). $12Ga^{3+} + 18O^{2+} = Ga_2O_3$		180.7058	
(6). $Zn^{2+} + Ga^{3+} + 2O^{2-} = ZGO$		19.1836	
(7). $7Zn^{2+} + Ga^{3+} + 16Cr^{3+} + 32O^{2-} = ZG$		348.8783	
(8). $8Zn^{2+} + Ga^{3+} + 17Cr^{3+} + 32O^{2-} = CG$		250.3528	
(9). $ZnO + Ga_2O_3 = ZnGa_2O_4$			229.6797
(10). $8\ ZnO + Ga_2O_3 + 6\ ZnCr_2O_4 + 29/2\ O_2 = 14ZG$			192.4038
(11). $14\ ZnO + Ga_2O_3 + 16\ Cr_2O_3 = 14\ ZG + 9/2\ O_2$			243.7237
(12). $16/15\ ZnO + 1/15\ Ga_2O_3 + Cr_2O_3 = 16/15\ CG$			162.7697
(13). $ZnO + 15\ ZnCr_2O_4 + Ga_2O_3 = 16CG$			-76.0651
(14). $2\ ZnO + Ga_2O_3 = 4\ Zn_{1/2}Ga_{1/2}O + 1/2\ O_2$			-75.0422
(15). $ZnO + Cr_2O_3 = ZnCr_2O_4$			254.7572

Table 3. 2. The BET areas, pore volume and average pore diameter of K-Ga_xZnCr catalysts. (x=0, 1.5, 3.0, 4.5 and 6.0).

Catalyst	BET area [a] (m^2/g)	External surface area [b] (m^2/g)	Pore volume [c] (cm^3/g)	Average pore diameter [d] (nm)
K-Ga_0ZnCr	63.86	62.89	0.2197	12.08
K-$Ga_{0.55}$ZnCr	78.43	76.67	0.2490	11.48
K-$Ga_{1.10}$ZnCr	75.96	71.90	0.2388	11.35
K-$Ga_{1.64}$ZnCr	66.08	65.77	0.1924	10.46
K-$Ga_{2.18}$ZnCr	61.71	57.42	0.2052	12.75

Note: [a] BET area was calculated by applying the multi-point BET equation in the linear range. [b] t-Plot external surface area. [c] single point adsorption total pore volume at P/P_0=0.99. [d] desorption average pore diameter (4V/A by BET).

Table 3.3. The Rietveld refinement results by MAUD software for K-Ga_xZnCr samples. (x=0.0, 0.55, 1.10, 1.64 and 2.18).

catalyst	$ZnCr_2O_4$		ZnO			sig	R_{wp}
	a	wt.%	a	c	wt.%		
K-Ga_0ZnCr	8.3629	95.2054	3.2540	5.1914	4.7946 ±0.0950	0.8614	12.6072
K-$Ga_{0.55}$ZnCr	8.3645	99.3184	3.2540	5.1914	0.6816 ±0.0761	0.8076	11.4636
K-$Ga_{1.10}$ZnCr	8.3661	95.6749	3.2481	5.2171	4.3251 ±0.1264	0.8823	12.2794
K-$Ga_{1.64}$ZnCr	8.3637	96.7516	3.2481	5.2171	3.2484 ±0.1153	0.8700	12.4247
K-$Ga_{2.18}$ZnCr	8.3590	96.4870	3.2481	5.2171	3.5130 ±0.1128	0.8716	12.1301
ZnO			3.2200	5.2000			
$ZnCr_2O_4$	8.3271						

Tables 3.4. Bader charge distribution of CO and Ga on $ZnCr_2O_4$ (311), (310) and (202) surfaces with and without Ga promotion.

surfaces	Bader charge
311	
Ga-311	0.4092[a]
CO/311	0.1929[b]
CO/Ga-311	-0.0112[b]/0.7650[a]
310	0
Ga-310	0.2940[a]
CO on 310	0.0182[b]
CO/Ga-310	-0.1681[b]/0.2000[a]
202	
Ga-202	0.7449[a]
CO/202	0.0482[b]
CO/Ga-202	-0.0266[b]/0.8388[a]

Note: a) bader charge on Ga; b) bader charge on CO.

Table 3.5. The adsorption energy of CO on the exposed $ZnCr_2O_4$ surfaces with or without Ga modification.

Surfaces	Adsorption energy of CO, eV
Ga- 202	0.03
202	-0.02
311	-0.78
Ga- 311	-0.65
Ga- 310	-0.80
310	-0.64

Table 3.6. XPS data for Cr2p spectra's of K-Ga_xZnCr samples.

catalyst	concentration, mol%					
	Cr		Cr^{3+}		Cr^{6+}	
	Area	mol,%	Area	mol,%	Area	mol,%
K-$Ga_{0.0}$ZnCr	17168.58	10.23	63456.74+65357.93	76.77	21818.66	13.00
K-$Ga_{0.55}$ZnCr	24759.53	12.27	65025.79+81071.56	72.43	30852.13	15.30
K-$Ga_{1.10}$ZnCr	13991.78	7.22	61769.33+76872.51	71.56	41084.85	21.21
K-$Ga_{1.64}$ZnCr	9970.29	5.32	91694.99+74899.72	88.97	10686.77	5.71
K-$Ga_{2.18}$ZnCr	14936.69	7.09	93622.57+84781.25	84.66	17377.78	8.25

Table 3.7. XPS data for Ga3d spectra of K-Ga_xZnCr catalysts.

catalyst	concentration, mol%							
	Ga^{3+} at 17.06 eV		Ga^{3+} at 19.93 eV		Ga^{3+} at 21.62 eV		Ga^{3+} at 23.74eV	
	Area	mol,%	Area	mol,%	Area	mol,%	Area	mol,%
K-$Ga_{0.55}$ZnCr	1259.77	17.93	2284.44	32.52	2455.26	34.95	1025.53	14.60
K-$Ga_{1.10}$ZnCr	974.87	13.59	2309.46	32.19	2955.38	41.19	934.78	13.03
K-$Ga_{1.64}$ZnCr	1067.62	15.09	1889.29	26.70	2924.98	41.34	1193.22	16.87
K-$Ga_{2.18}$ZnCr	1406.51	18.41	1735.14	22.71	3749.57	49.08	748.80	9.80

Table 3.8. The bulk and surface element compositions of K-GaxZnCr catalysts.

catalysts	bulk[a]			On the surface[b]		
	Zn/Cr	Zn/Ga	Cr/Ga	Zn/Cr	Zn/Ga	Cr/Ga
K-Ga_0ZnCr	0.94	--	--	1.15	--	--
K-$Ga_{0.55}$ZnCr	0.91	79.82	55.88	1.13	28.03	26.90
K-$Ga_{1.10}$ZnCr	0.91	34.39	23.95	1.12	26.13	23.23
K-$Ga_{1.64}$ZnCr	0.89	22.71	16.12	1.14	17.48	15.64
K-$Ga_{2.18}$ZnCr	0.90	10.19	7.20	1.04	14.94	13.11

Note: a) the bulk composition is obtained by the analysis to XRF to the catalysts. b) the surface composition is obtained by fitting the spectral of XPS.

Table 3.9. The surface concentration of oxygenates species of K-Ga_xZnCr catalysts.

catalyst	$O_{latt}/(O_{latt} + O_{ads} + O_{OH})$	$O_{ads}/(O_{latt} + O_{ads} + O_{OH})$	$O_{OH}/(O_{latt} + O_{ads} + O_{OH})$
K-$Ga_{0.0}$ZnCr	63.28	30.86	5.86
K-$Ga_{0.55}$ZnCr	60.48	34.85	4.66
K-$Ga_{1.10}$ZnCr	62.10	32.06	5.84
K-$Ga_{1.64}$ZnCr	62.51	33.38	4.11
K-$Ga_{2.18}$ZnCr	52.06	41.68	6.26

Table 3.10. Typical catalytic performance of K-Ga_xZnCr iso-butanol catalysts.

Catalysts	CO conversion,%	STY g/(h•g cat)	Selectivity, C mol%					Distribution of alcohols, wt%				
			CH_4	CO_2	CH_X [a]	DME [b]	alcohol	MEOH [c]	EtOH [d]	PrOH[e]	i-BuOH[f]	C^{5+}OH[g]
K-$Ga_{0.0}$ZnCr	23.59	0.0695	0	42.55	2.95	0	51.50	57.98	0.93	4.38	33.13	3.57
K-$Ga_{0.55}$ZnCr	23.75	0.0996	1.69	38.73	6.70	0.01	52.87	57.23	0.92	3.97	36.03	1.84
K-$Ga_{1.10}$ZnCr	23.17	0.1103	0.85	34.64	5.46	0.01	59.03	59.53	1.02	4.53	31.23	3.69
K-$Ga_{1.64}$ZnCr	21.24	0.1101	1.81	37.23	7.40	0.03	53.72	58.94	0.87	3.96	31.58	4.64
K-$Ga_{2.18}$ZnCr	24.16	0.0819	1.26	34.36	19.96	2.43	41.99	69.44	0.99	4.09	23.21	2.19
K-$ZnGa_2O_4$	14.18	0.0427	1.73	19.53	2.91	58.70	17.13	87.84	1.89	0.53	5.84	1.36

Note: a) summary of the amount of ethane, propane and butane in the tail gas. b) dimethyl ether. c) methanol. d) ethanol. e) n-propanol and isopropanol. f) iso-butanol . g) amyl alcohol.

Table 3.11. The K-$Ga_{1.10}$ZnCr iso-butanol catalyst life testing.

		STY	Selectivity, C mol%					Distribution of alcohols, wt%				
TOS,h	CO conversion,%	g/(h•g cat)	CH_4	CO_2	CH_X[a]	DME[b]	alcohol	MEOH[c]	EtOH[d]	PrOH[e]	i-BuOH[f]	C^{5+}OH[g]
22	23.17	0.1103	0.85	34.64	5.46	0.01	59.03	59.53	1.02	4.53	31.23	3.69
31	24.91	0.1000	0.04	34.75	5.18	0.02	60.00	57.28	0.97	4.62	33.44	3.70
46	24.04	0.0955	0	33.77	5.13	0.01	61.08	56.75	1.01	4.52	31.92	5.80
55	23.44	0.1069	0.43	32.13	5.42	0.01	62.00	59.22	1.06	4.57	32.83	2.42
78	29.46	0.0875	0	32.57	4.47	0.01	62.95	58.37	1.02	4.56	33.00	2.96
102	21.34	0.1009	0	35.47	5.15	0.01	59.37	60.75	1.35	4.77	33.13	0

Note: a) summary of the amount of ethane, propane and butane in the tail gas. b) dimethyl ether. c) methanol. d) ethanol. e) n-propanol and isopropanol. f) iso-butanol . g) amyl alcohol.

Reaction conditions: temperature=400 ^oC, pressure=10.0 MPa, GHSV=3300 h^{-1}.

Table 3.12. The adsorption energy of H_2, CO, H_2O, CO_2 on ZnCr spinel and ZG surfaces.

catalyst	species and their adsorption energies			
	H_2	CO	H_2O	CO_2
$ZnCr_2O_4$ (111)	-2.88	-0.74	1.25	-1.22
ZG (111)	-1.06	-2.99	1.73	0.42
$ZnGa_2O_4$ (111)		-0.36	-1.83	-1.31

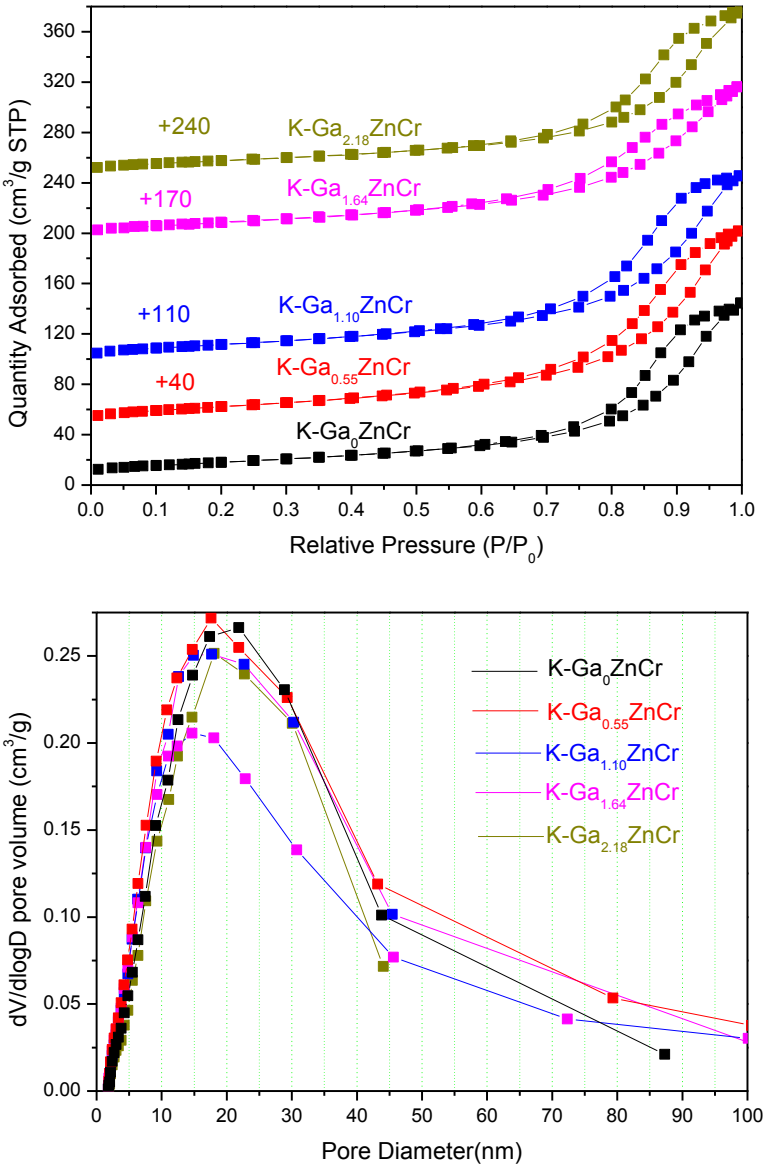

Fig. 3. 1. Isotherm linear plot (left) and BJH desorption of dV/dD pore volume (right) for K-GaxZnCr samples. (x=0.0, 0.55, 1.10, 1.64 and 2.18)

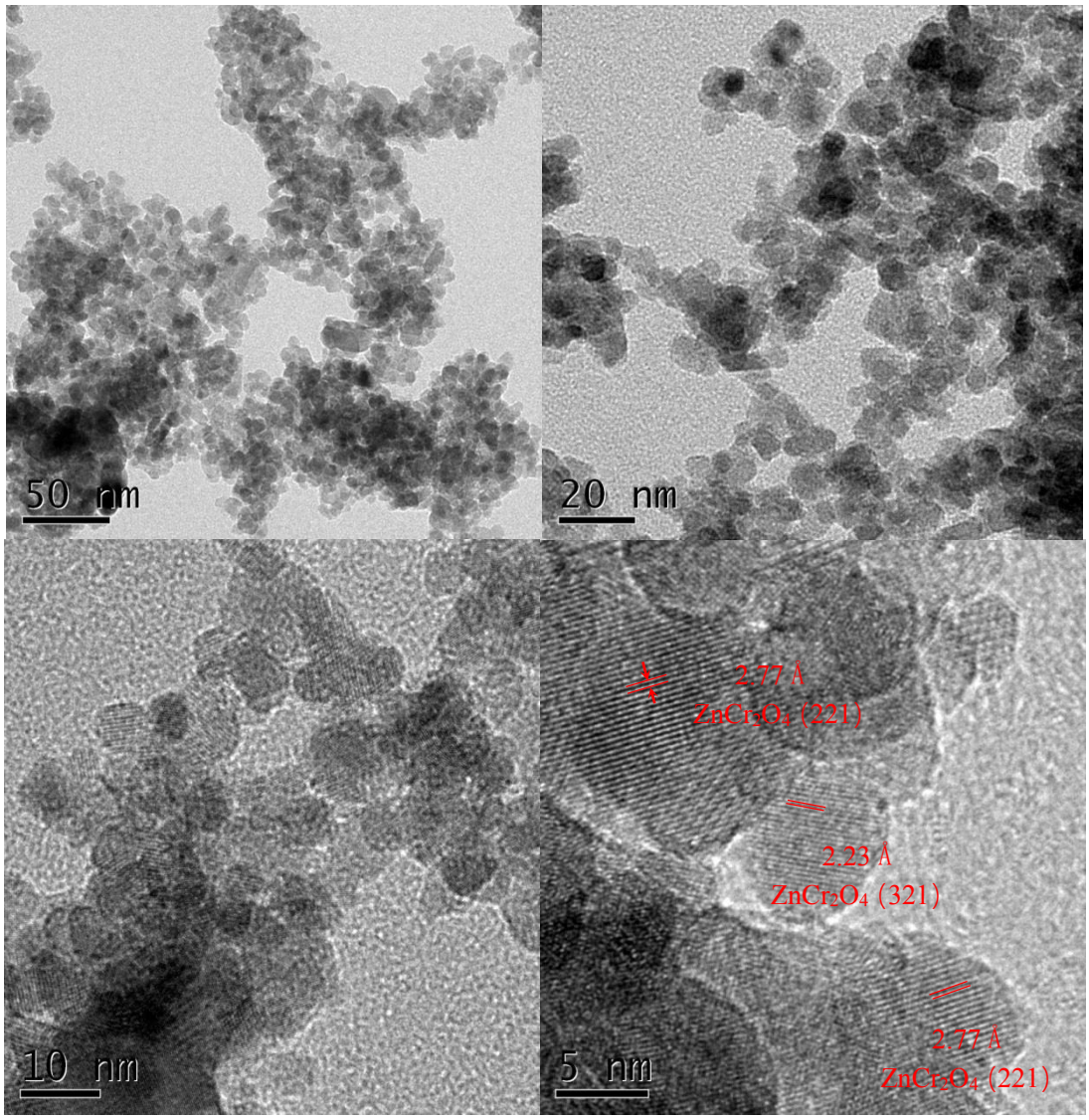

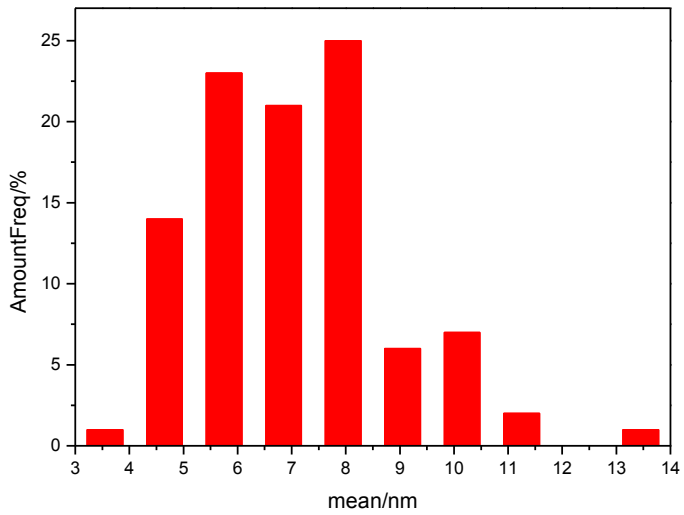

Fig. 3.2 HR-TEM images of K-$Ga_{0.0}$ZnCr catalyst.

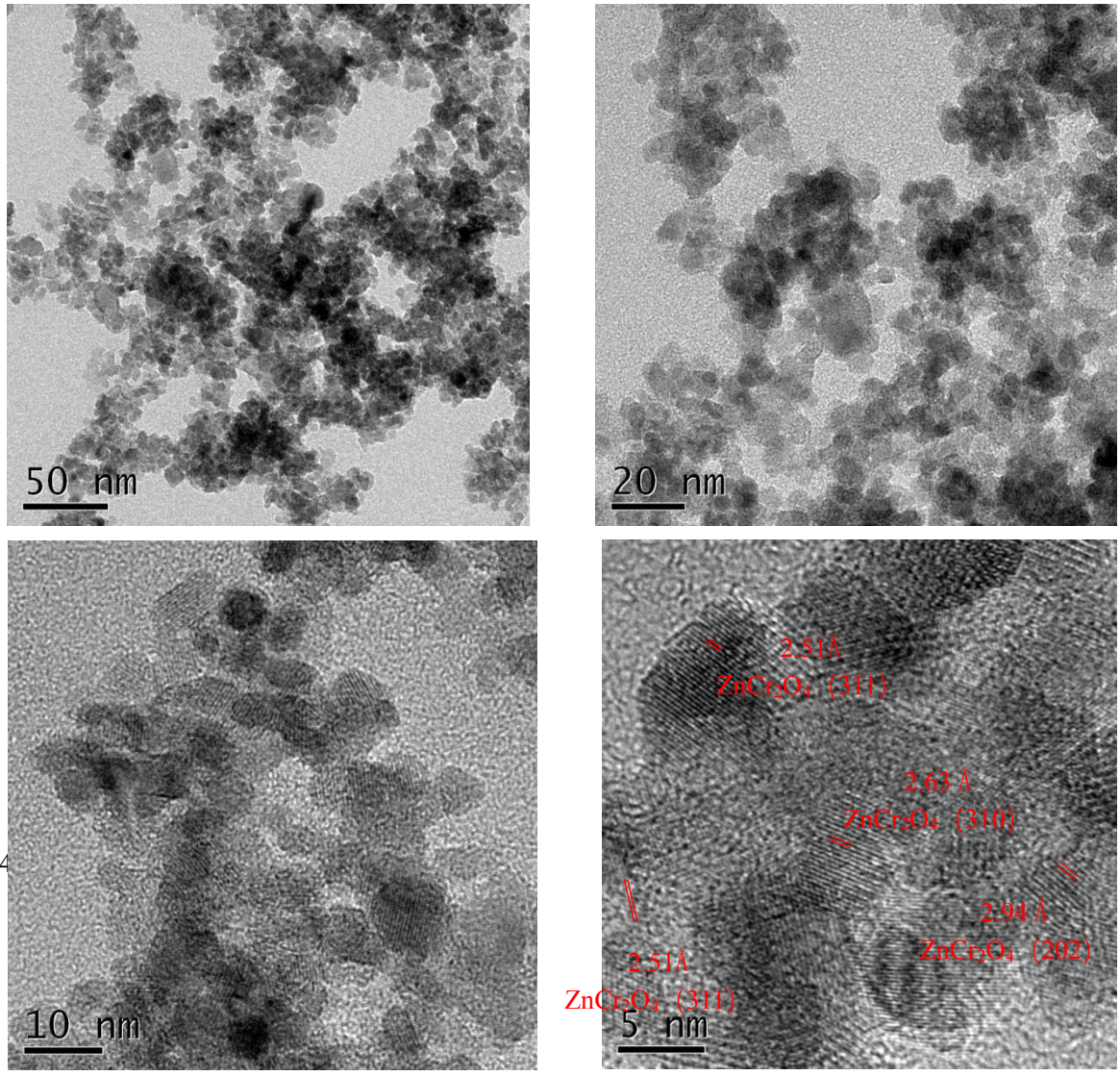

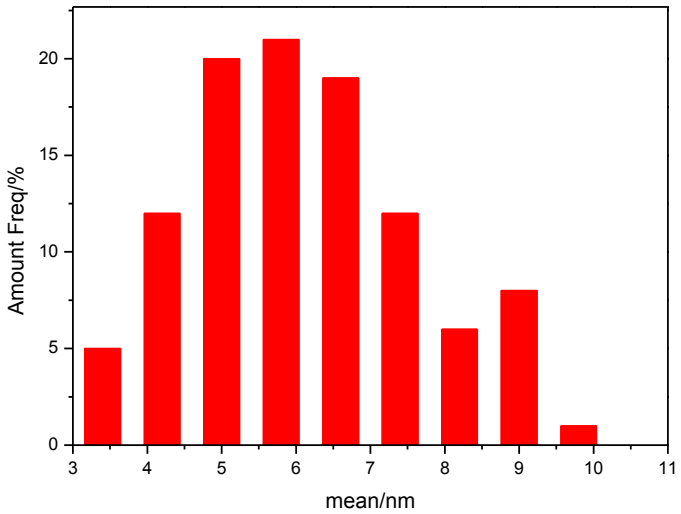

Fig. 3.3 HR-TEM images of K-$Ga_{1.10}$ZnCr catalyst.

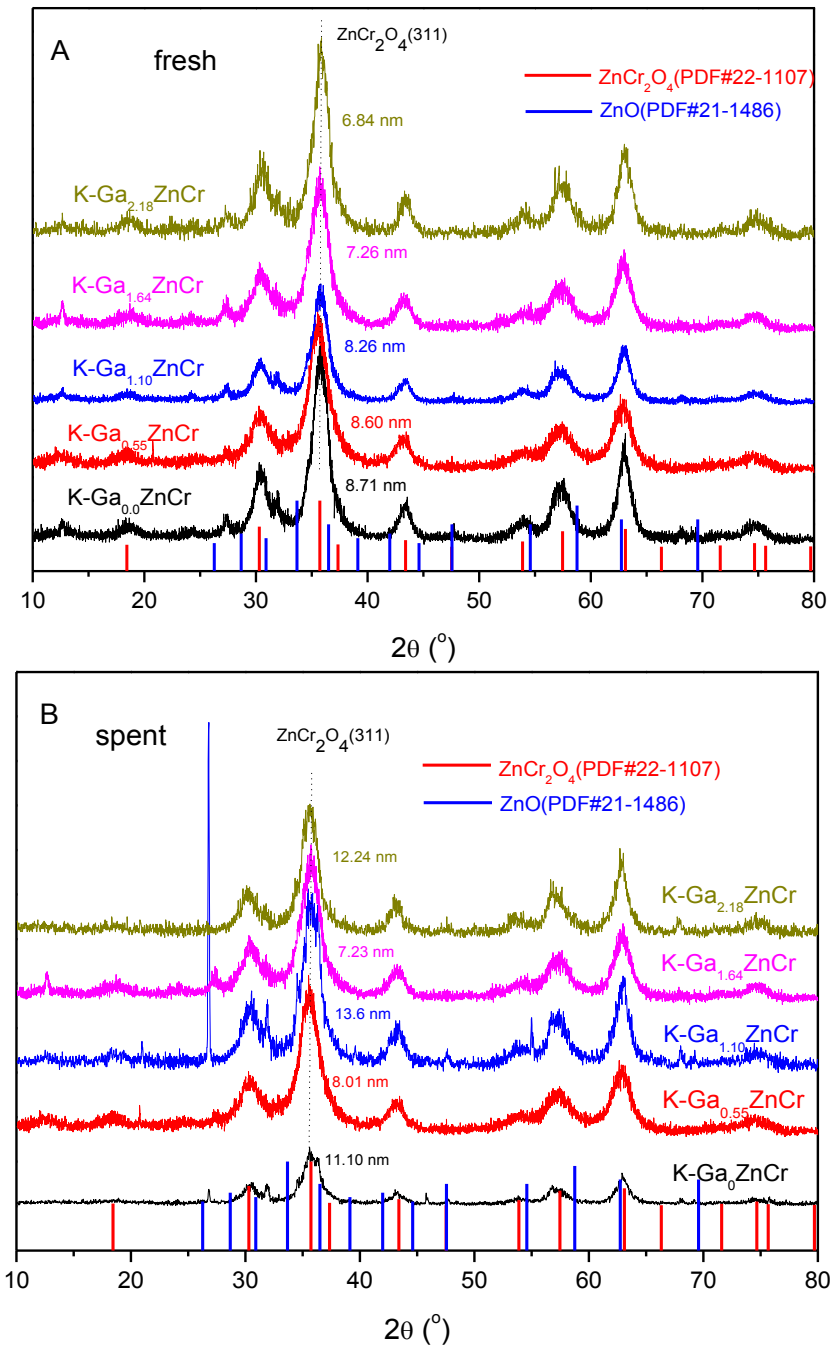

Fig. 3. 4. XRD patterns of fresh (A) and apent (B) K-Ga$_x$ZnCr catalysts.

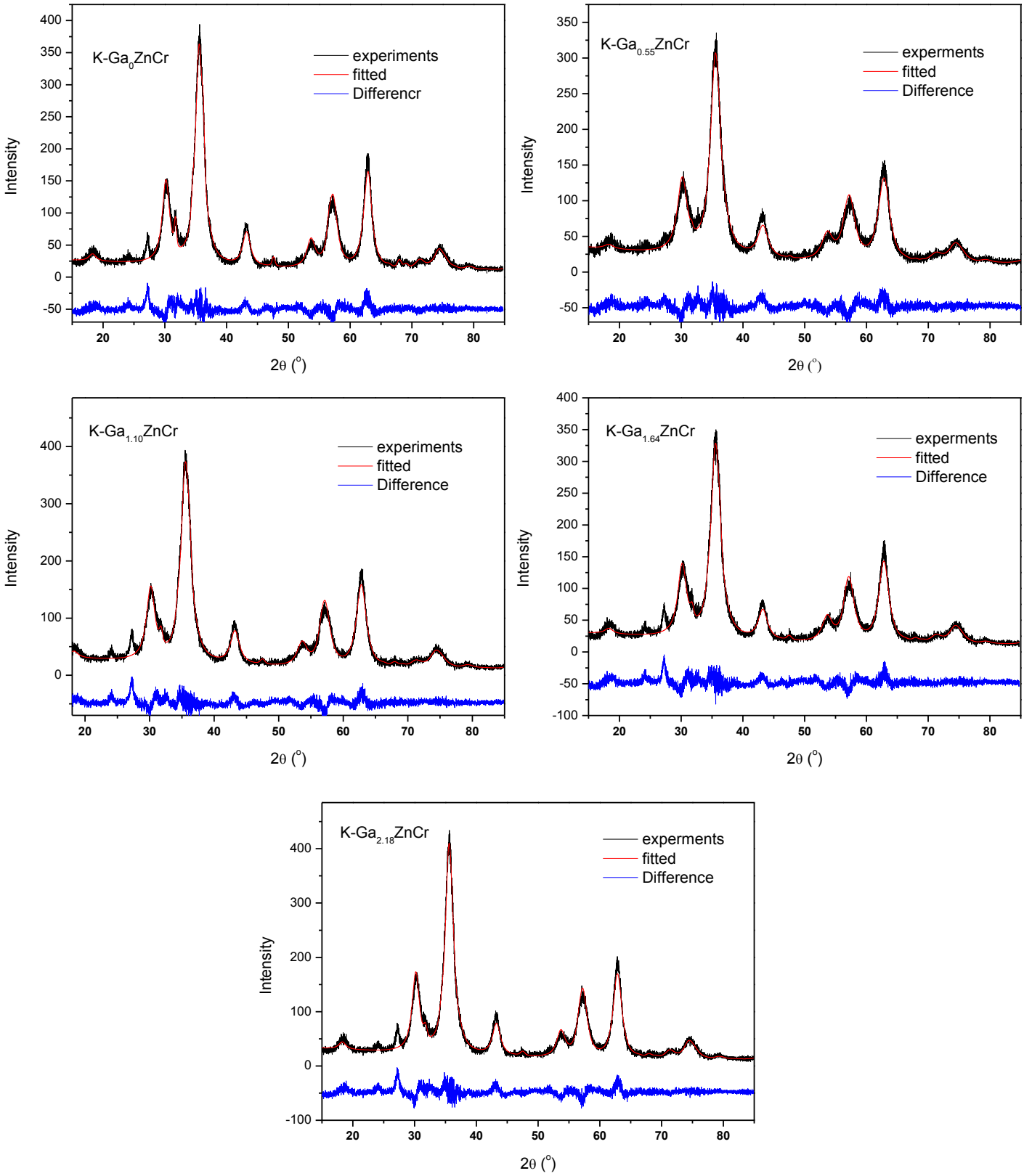

Fig. 3. 5. Rietveld refinement results to the XRD patterns of K-Ga$_x$ZnCr catalysts.

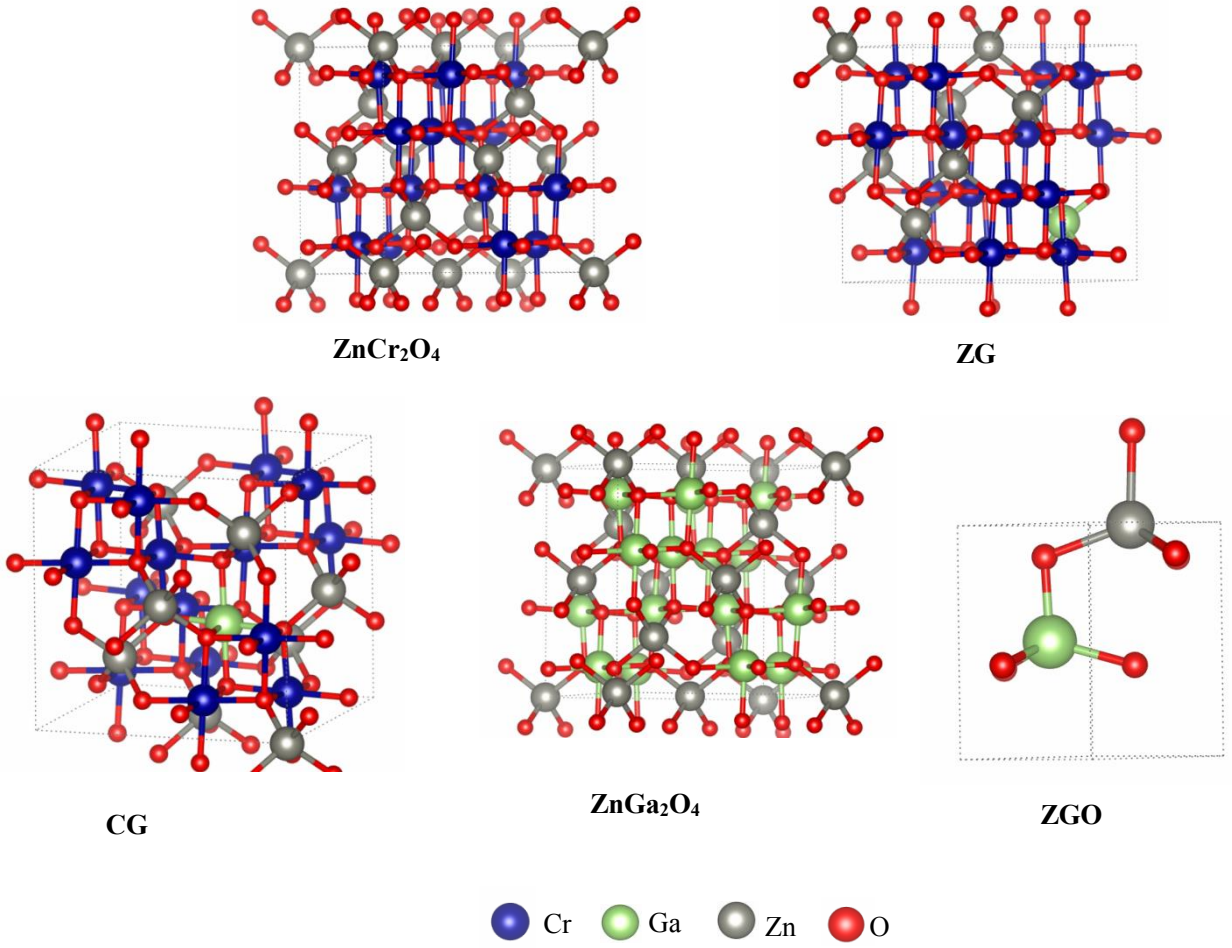

Fig. 3. 6 Schematic diagram of crystal structure for $ZnCr_2O_4$, ZG, CG, $ZnCa_2O_4$ and ZGO.

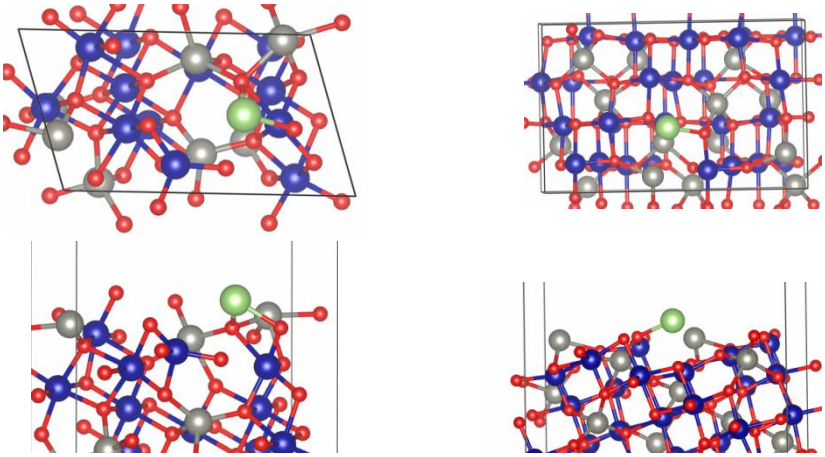

Ga on (311) of $ZnCr_2O_4$

Ga on (310) of $ZnCr_2O_4$

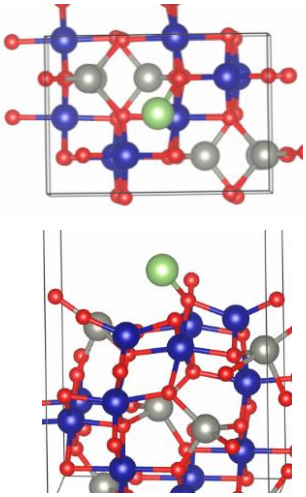

Ga on (202) of $ZnCr_2O_4$

Fig. 3. 7. Top and side views of the configurations for Ga adsorbed on the (311), (310) and (202) surfaces of $ZnCr_2O_4$.

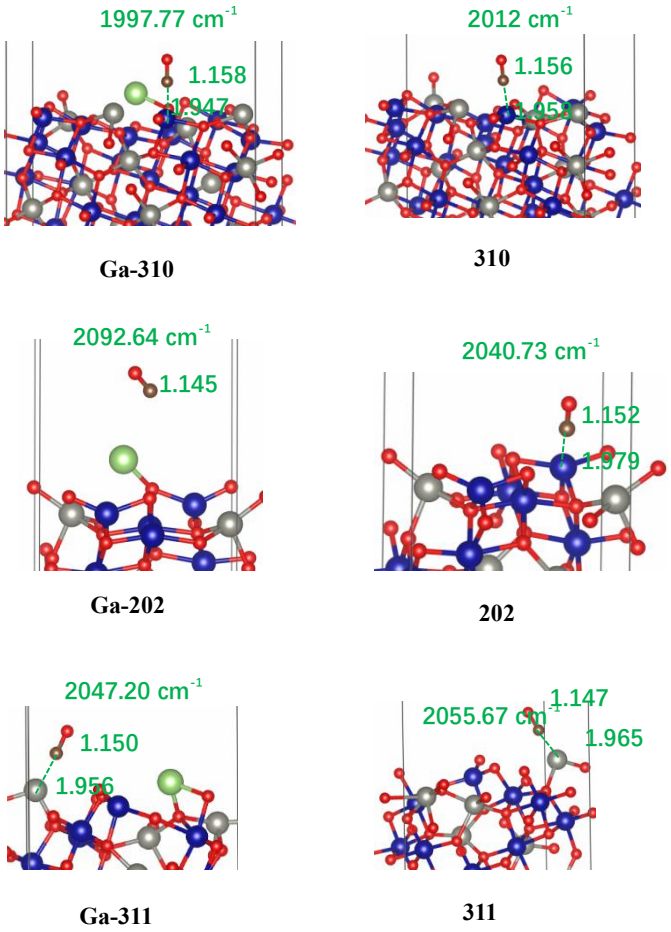

Fig. 3. 8. CO adsorption configurations and vibrational frequency on the (310), (202) and (311) surfaces of $ZnCr_2O_4$ and Ga-$ZnCr_2O_4$.

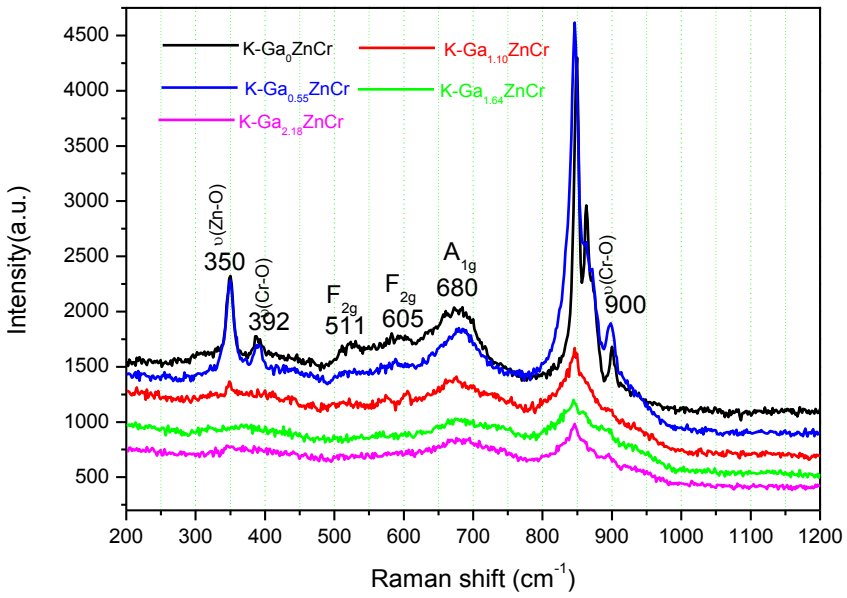

Fig. 3. 9. Raman spectra of K-GaZnCr catalysts

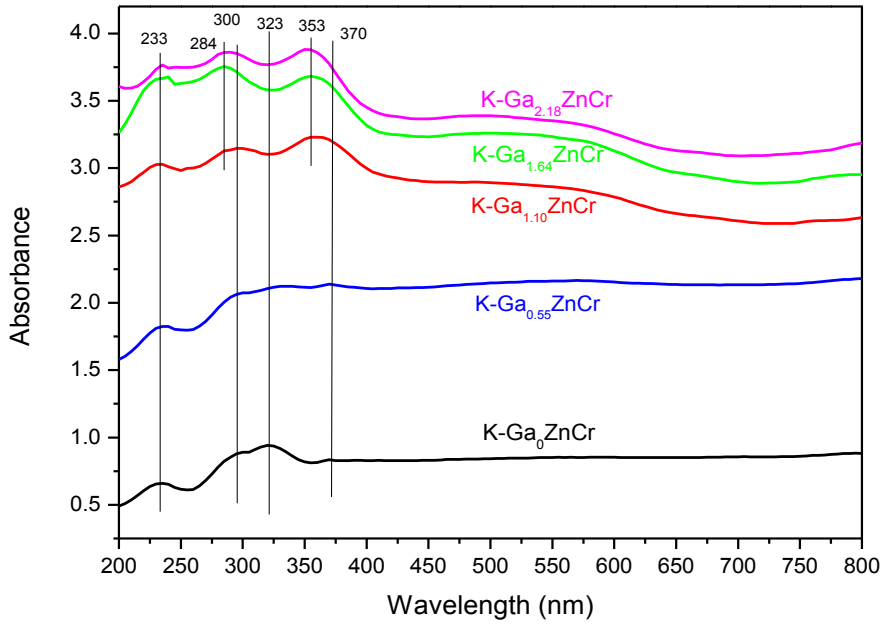

Fig. 3. 10. Ultraviolet-visible diffuse reflectance spectrums of K-Ga$_x$ZnCr catalysts

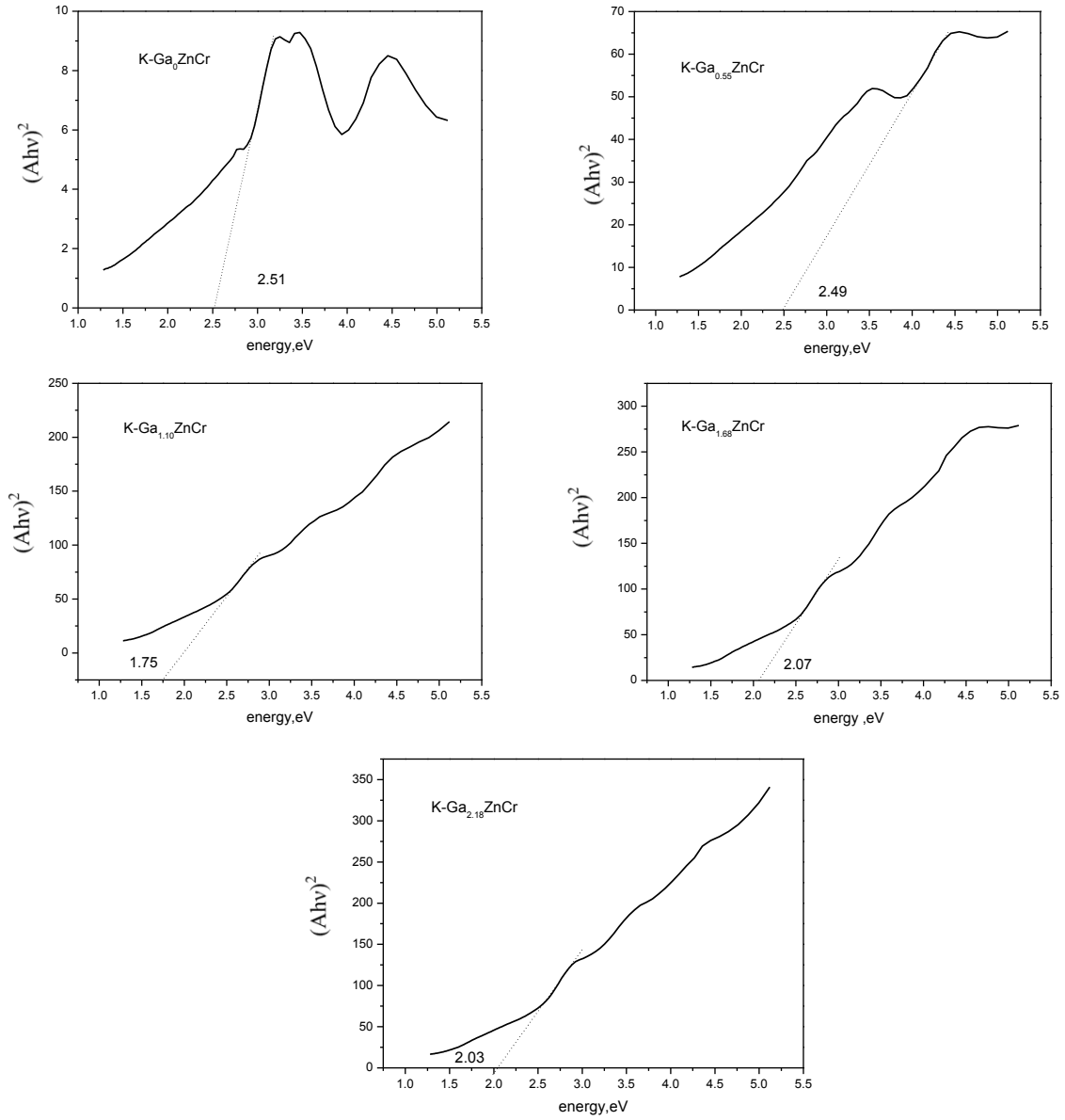

Fig. 3.11. Indirect band gap E_g calculated from ultraviolet-visible diffuse reflectance spectral for K-Ga_xZnCr catalysts.

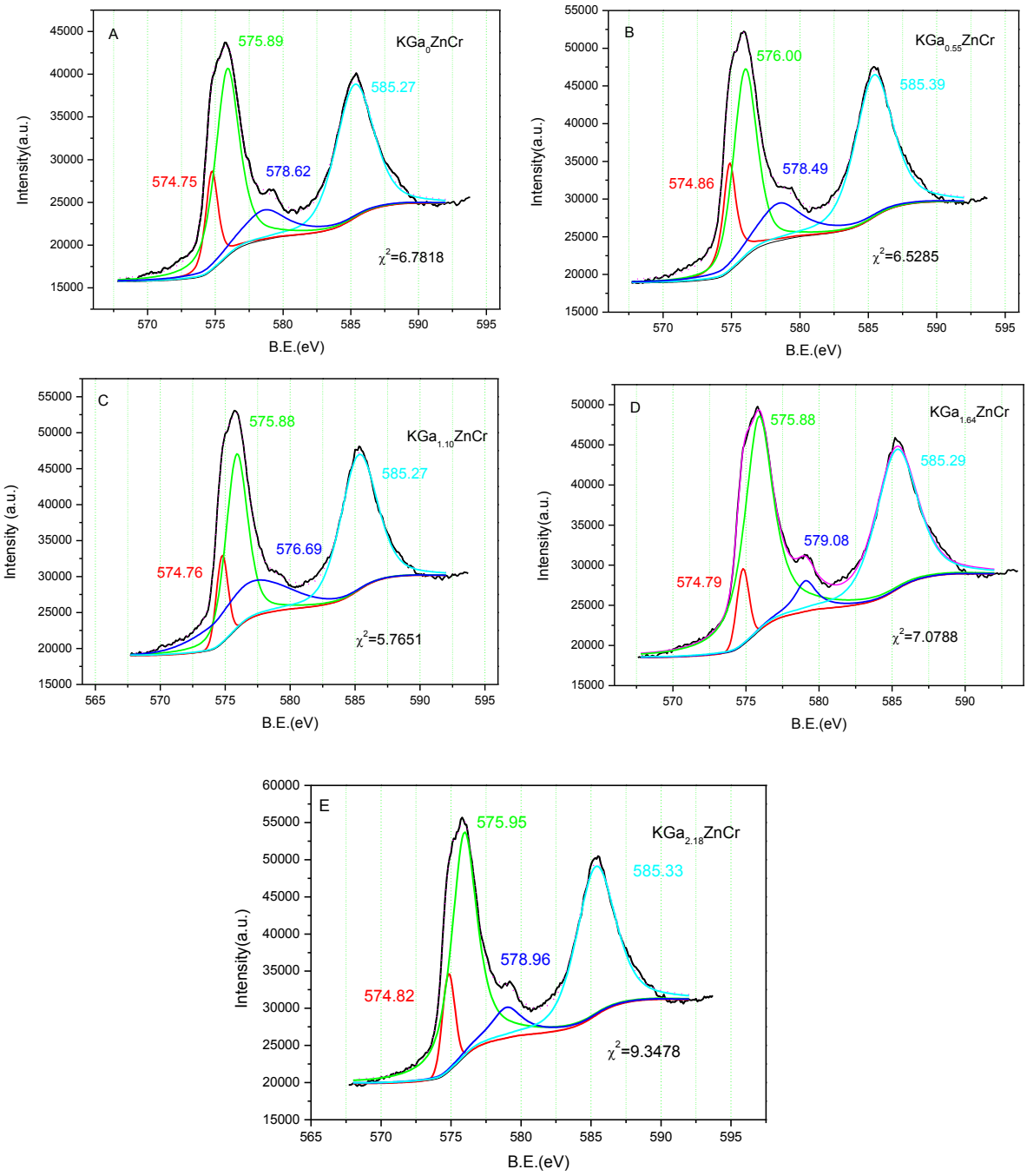

Fig. 3. 12. The XPS spectral of Cr_{2p} for K-Ga_xZnCr samples. (x=0.0, 0.55, 1.10, 1.64 and 2.18)

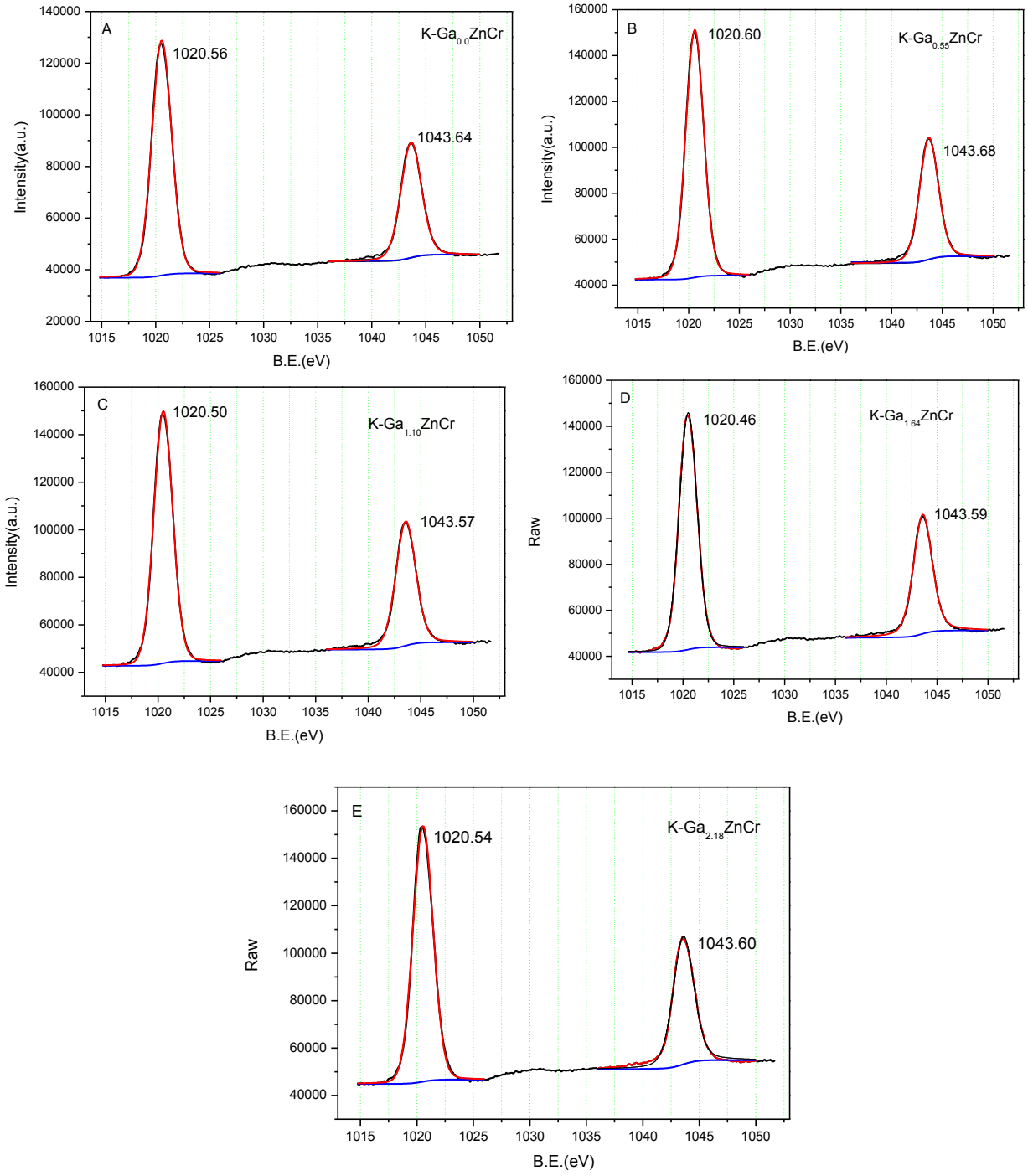

Fig. 3. 13. The XPS spectral of Zn_{2P} for K-Ga_xZnCr samples. (x=0.0, 0.55, 1.10, 1.64 and 2.18) .

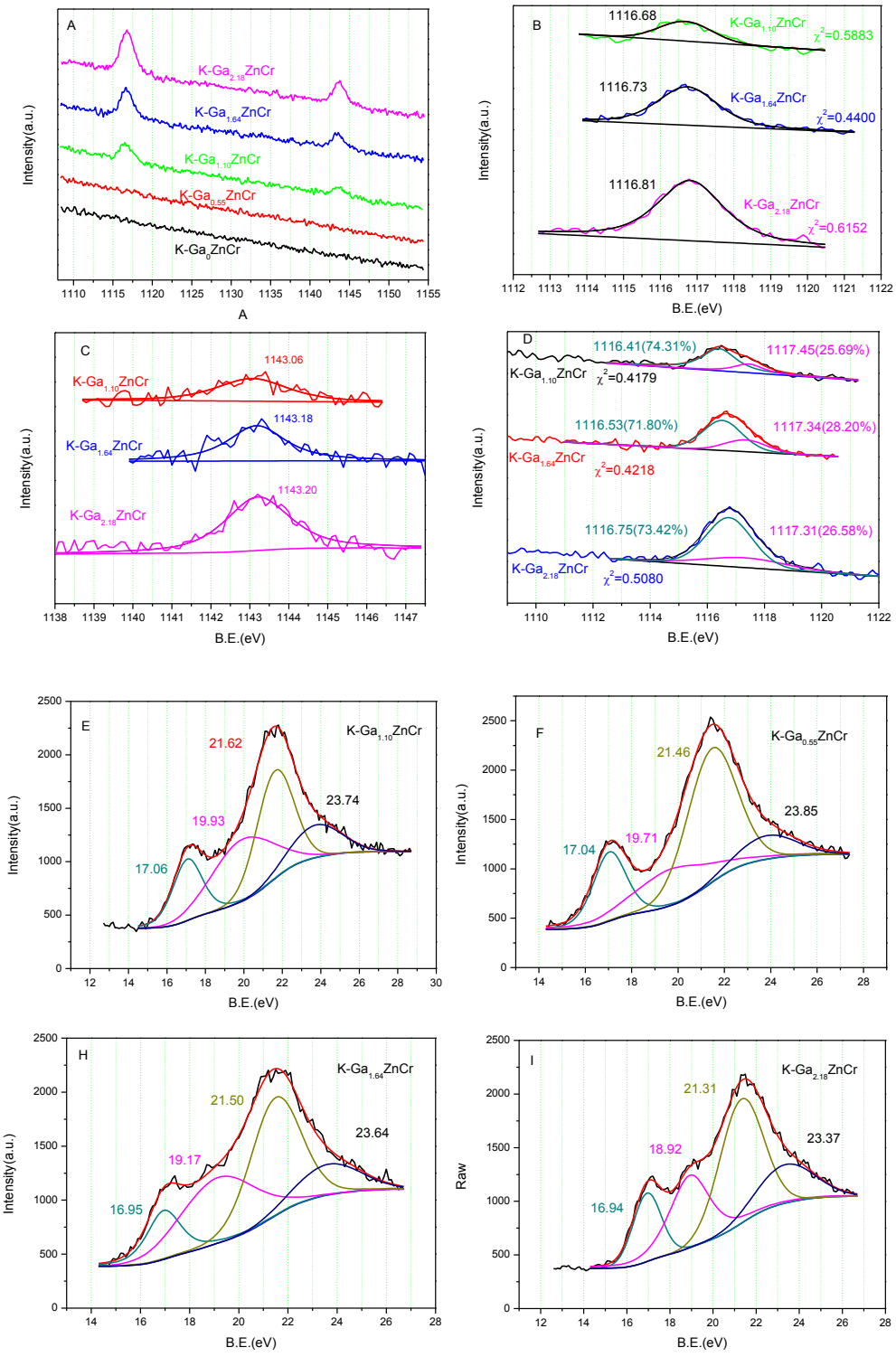

Fig .3.14 XPS spectral of Ga 2p (A-D) and 3d (E-I) of K-Ga$_x$ZnCr samples.(x=0.55, 1.10, 1.64 and 2.18).

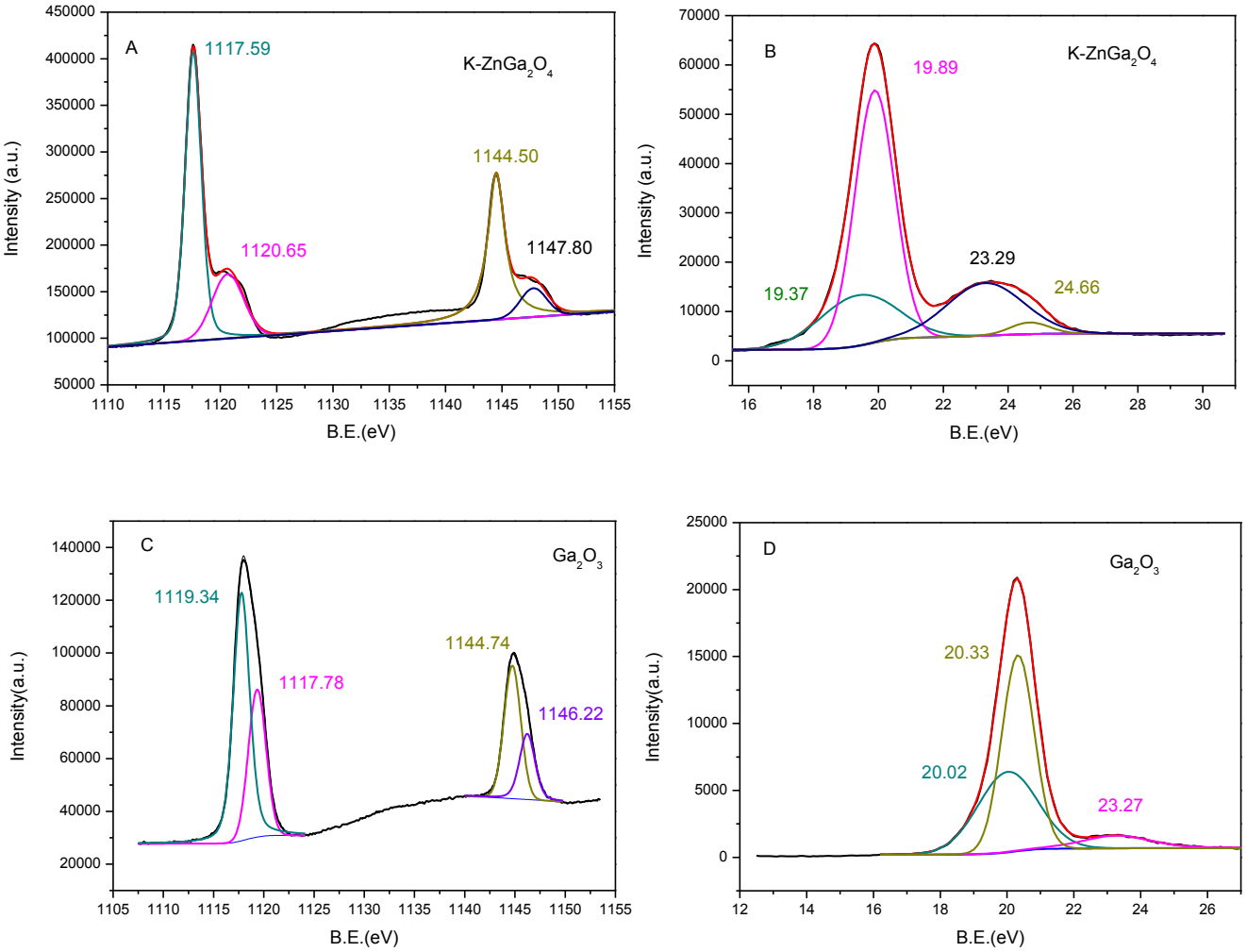

Fig. 3. 15. The XPS spectrals of Ga2p for K-$ZnGa_2O_4$ (A), Ga_2O_3 (C) and Ga3d for K-$ZnGa_2O_4$ (B), Ga_2O_3 (D). Ga_2O_3 (99.99%) was perched from Shanghai Aladdin Biochemicl Technology Co.Ltd

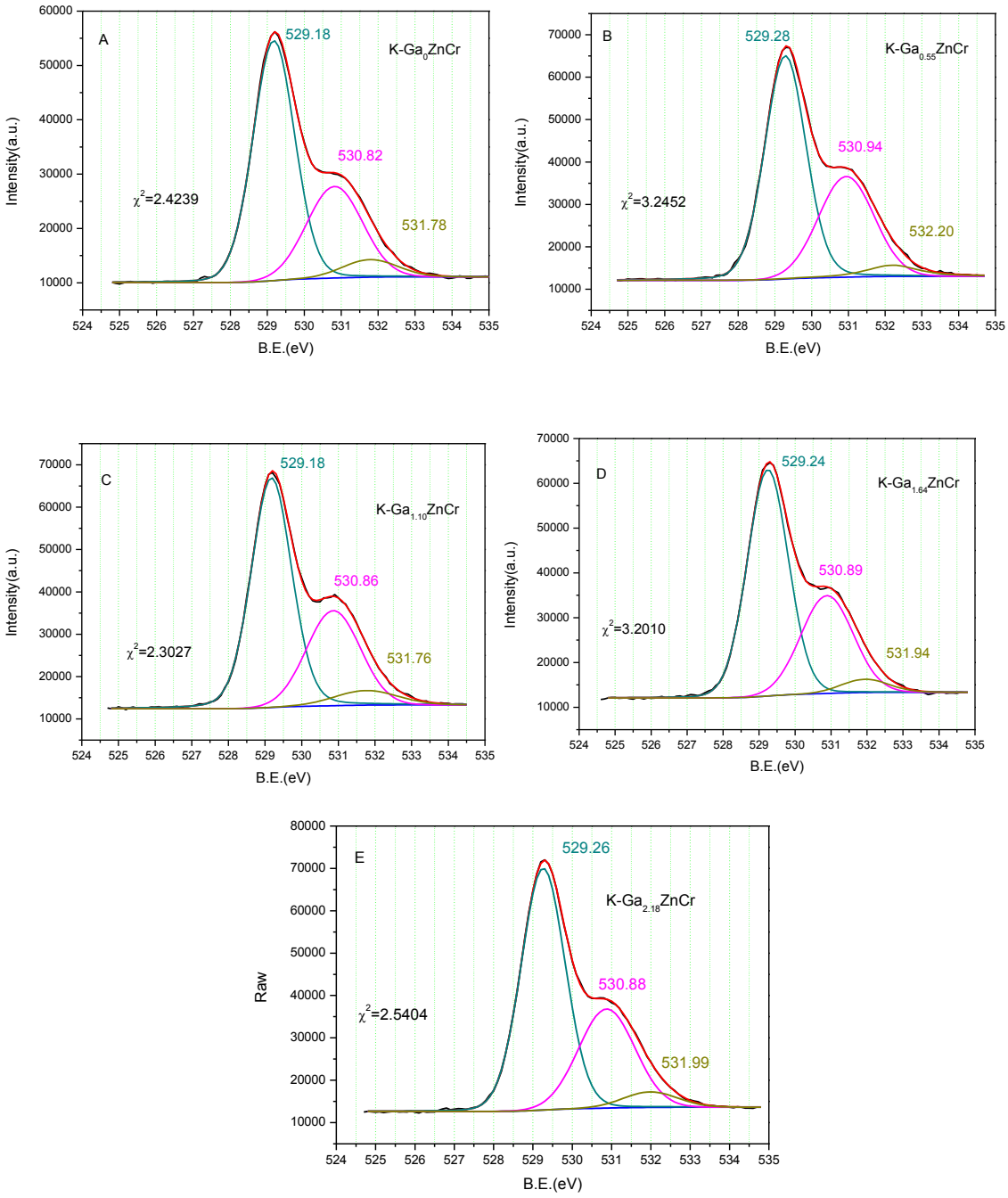

Fig. 3. 16. The XPS spectral of O1s for K-Ga$_x$ZnCr samples. (x=0.0, 0.55, 1.10, 1.64 and 2.18).

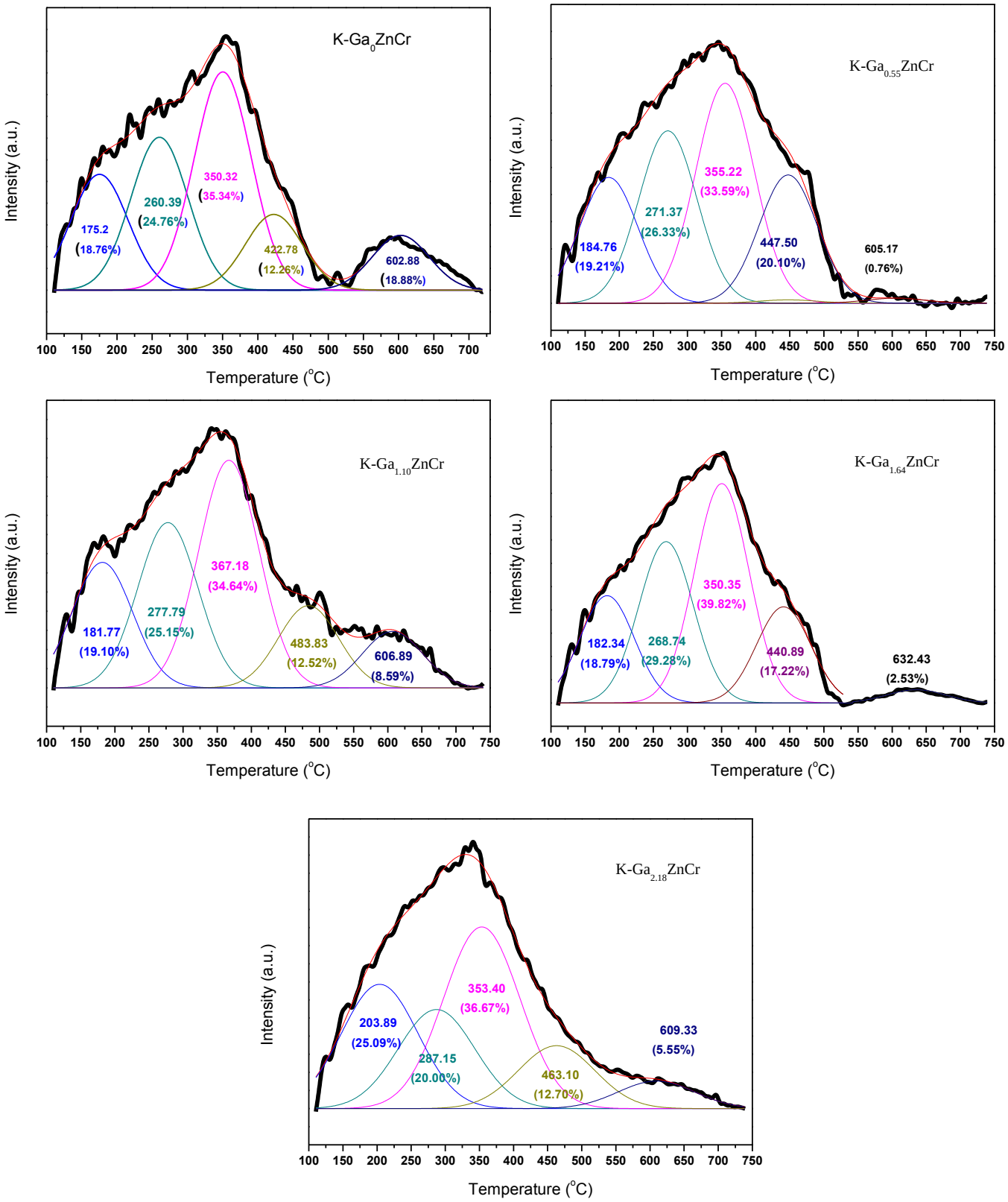

Fig. 3. 17. The CO_2-TPR profiles for K-Ga_xZnCr samples. (x=0.0, 0.55, 1.10, 1.64 and 2.18).

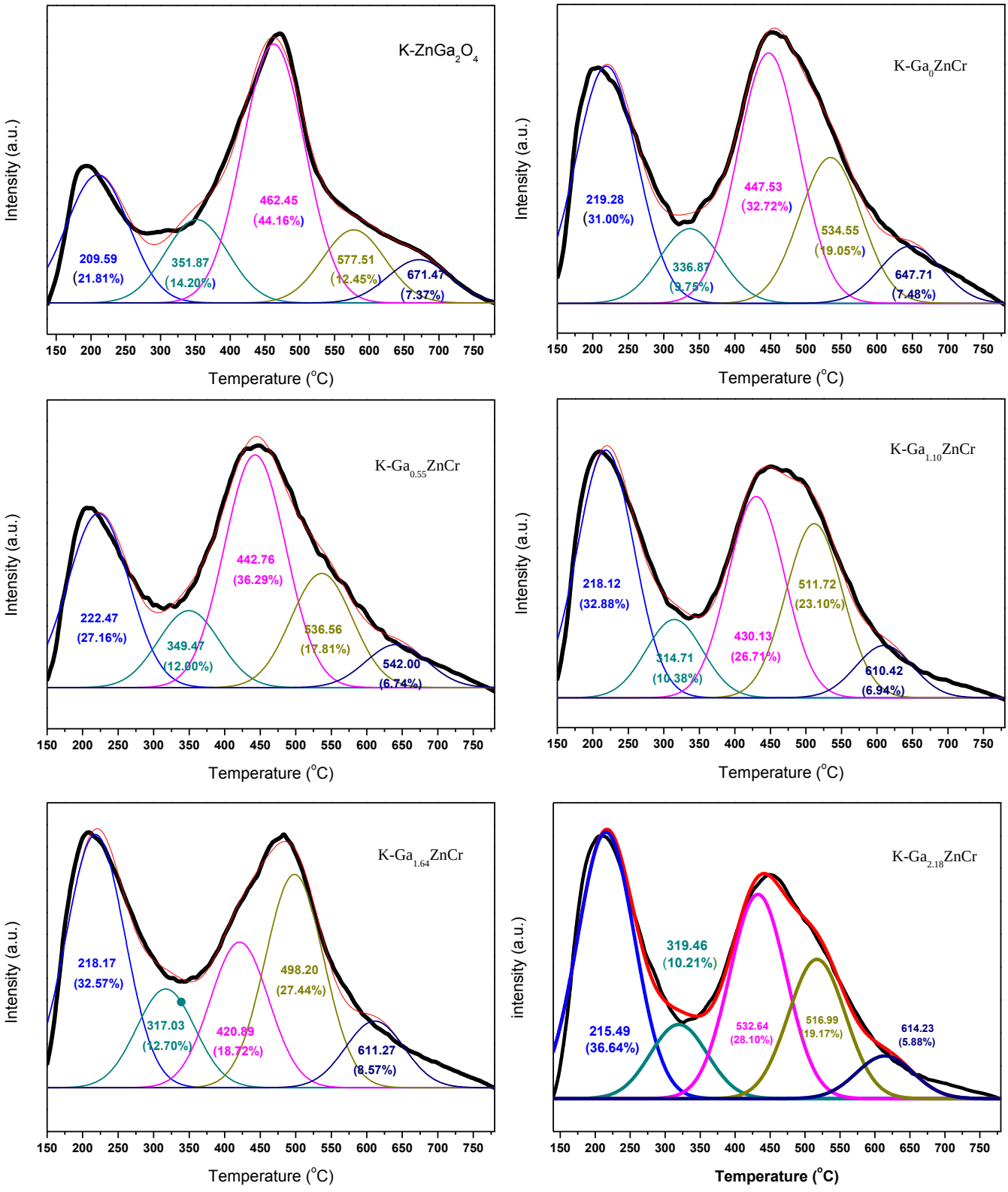

Fig. 3. 18. The NH_3-TPR profiles for K-$ZnGa_2O_4$ and K-Ga_xZnCr samples. (x=0.0, 0.55, 1.10, 1.64 and 2.18)**.**

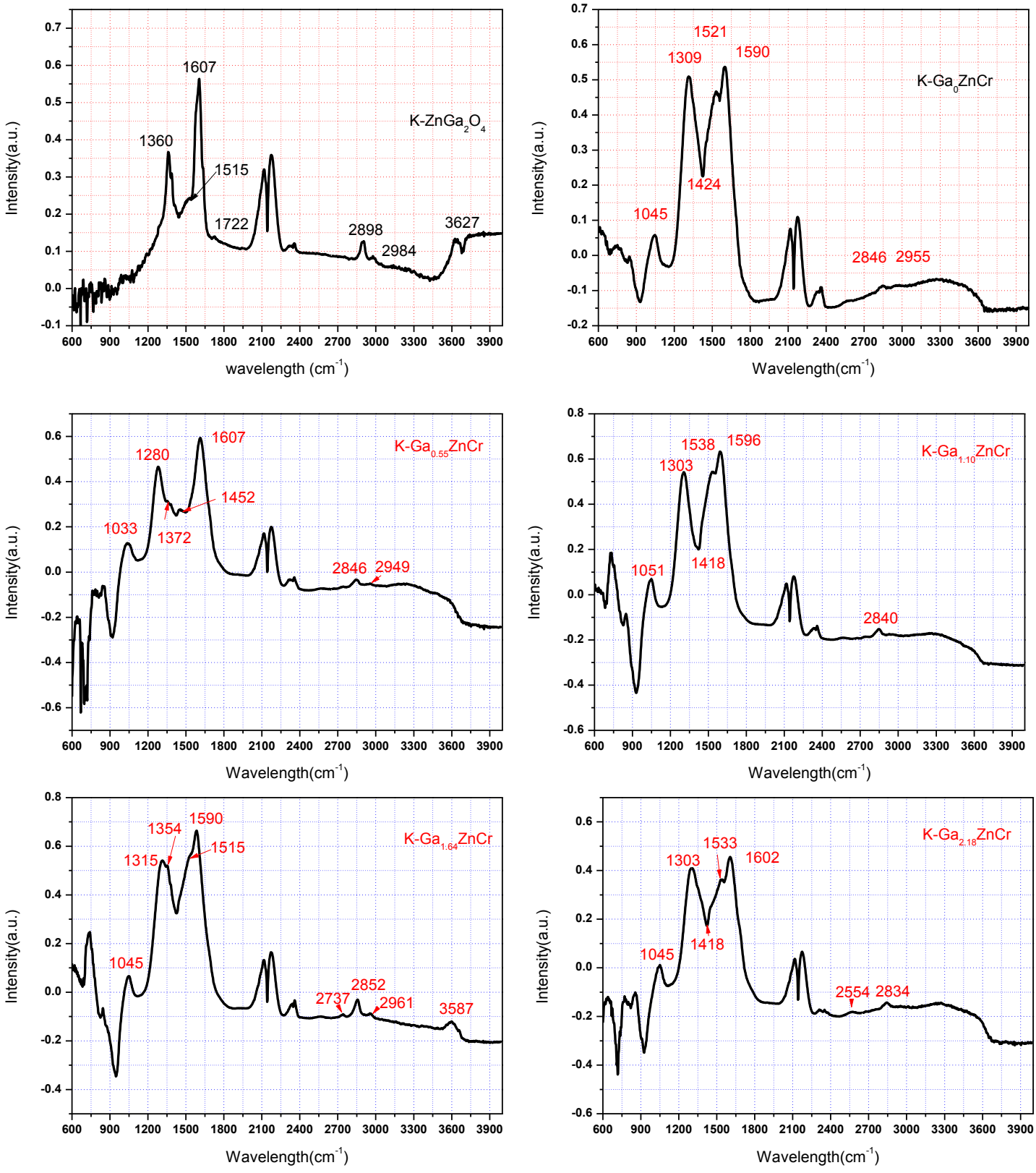

Fig. 3. 19. DRIFT spectral of CO absorption on K-$ZnGa_2O_4$ and K-Ga_xZnCr samples and 400 ^oC. (x=0.0, 0.55, 1.10, 1.64 and 2.18).

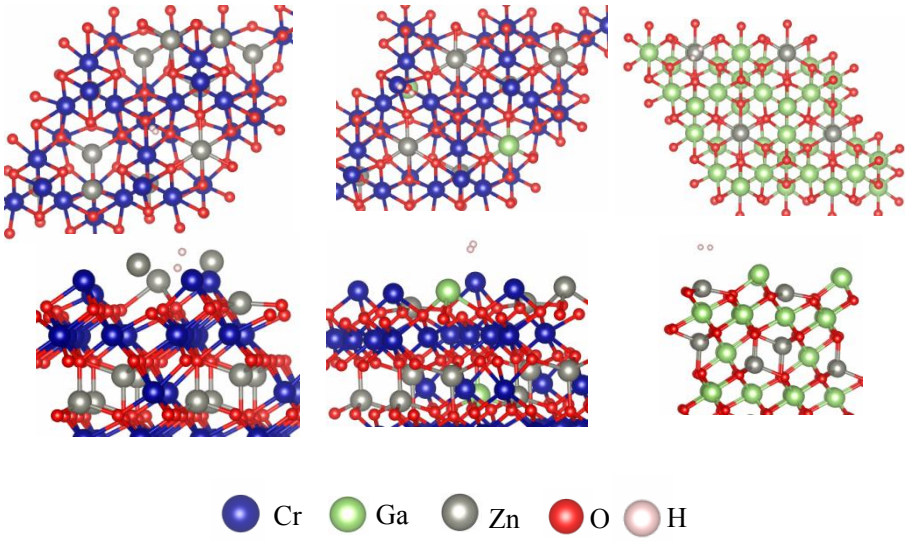

Fig. 3. 20. The most stable adsorption configurations of H_2 on $ZnCr_2O_4$ (111) surface, ZG (111) surface, and $ZnGa_2O_4$ (111) surface.

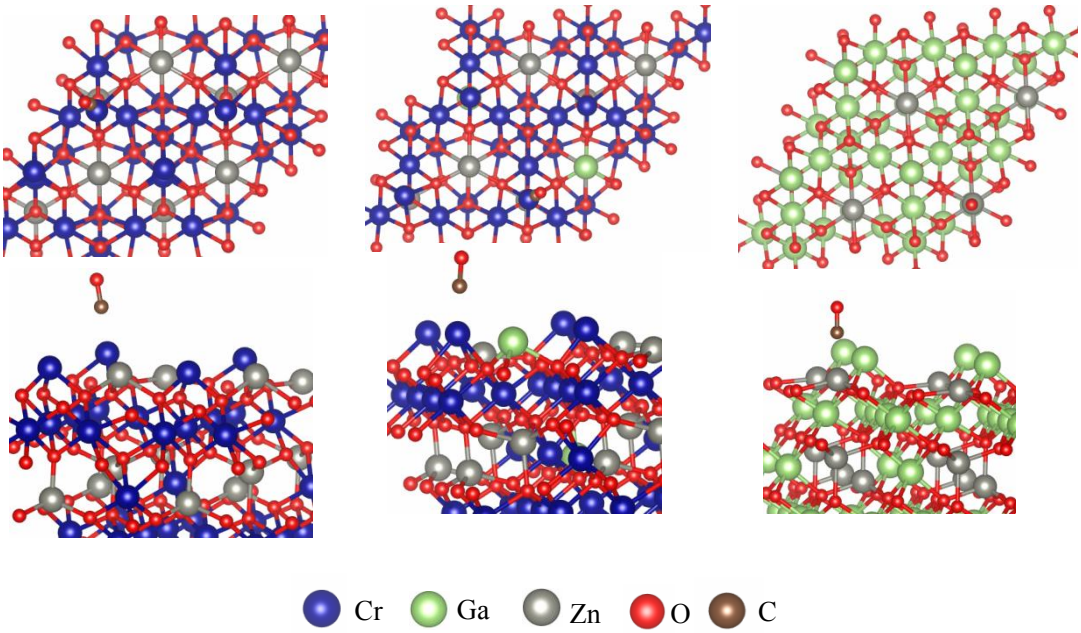

Fig. 3. 21. The most stable adsorption configurations of CO on $ZnCr_2O_4$ (111) surface, ZG (111) surface, and $ZnGa_2O_4$ (111) surface.

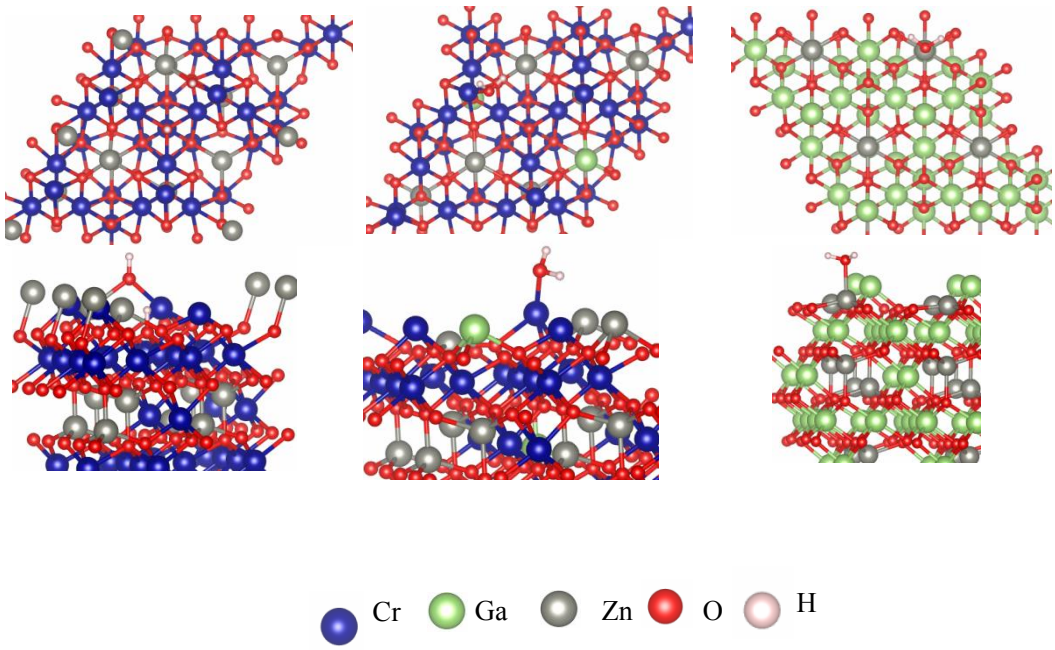

Fig. 3. 22. The most stable adsorption configurations of H_2O on $ZnCr_2O_4$ (111) surface, ZG (111) surface, and $ZnGa_2O_4$ (111) surface.

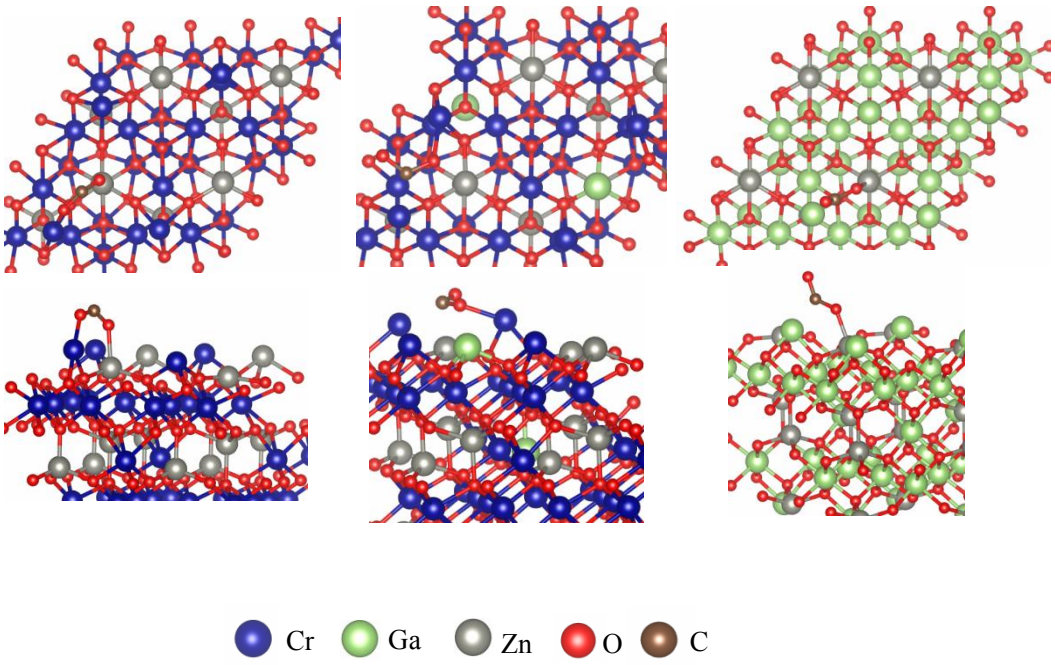

Fig. 3. 23. The most stable adsorption configurations of CO_2 on $ZnCr_2O_4$ (111) surface, ZG (111) surface, and $ZnGa_2O_4$ (111) surface.

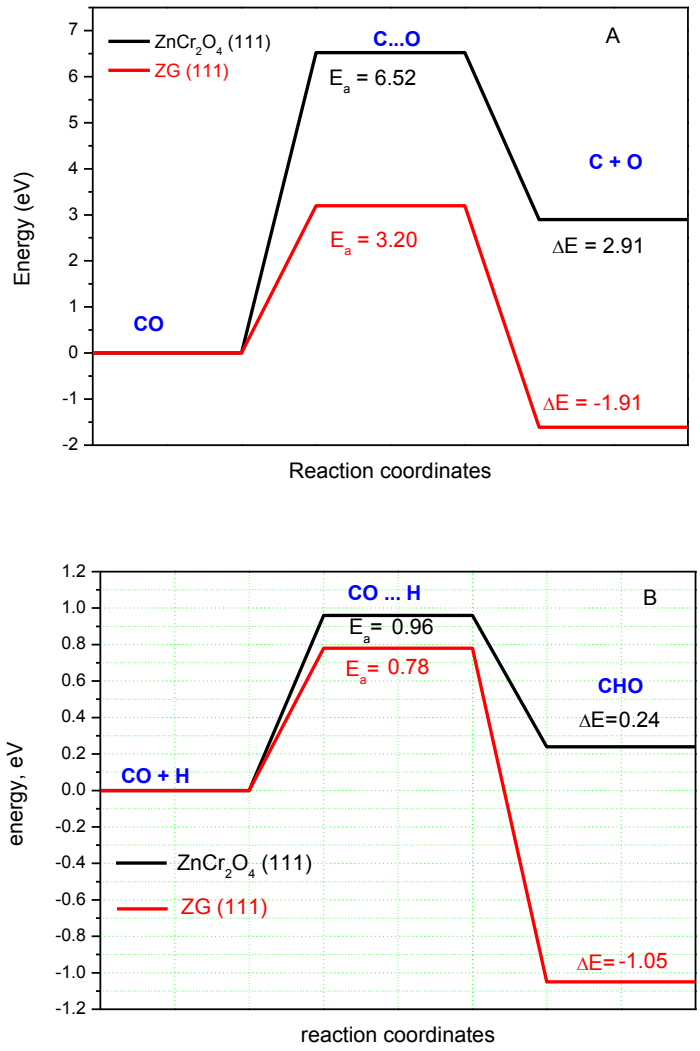

Fig. 3. 24. Reaction coordinates of direct dissociation of CO (A) and CHO formation (B) on $ZnCr_2O_4$ (111) and ZG(111) surfaces.

Cpapter 4

Summary

Owing to the energy crisis and increasing demand on more clean fuel and chemicals, alcohols synthesised from syngas have paid consideration attention. The C1-route driven by syngas can make full use of carbon bearing resources such as abundant coal, natural gas and biomass resources, is considered to be an important supplement of petrochemical and bio-fermentation process to synthesis of alcohols. Alkali metal oxides modified methanol catalysts (copper based low temperature methanol catalysts and ZnCr based high temperature methanol catalyst) are usually adopted as the important catalysts to synthesis alcohols owing to their higher alcohol selectivity. In this thesis, we focused on the two factors to investigate the relations between the catalyst structure and their catalytic performance for these catalysts. One is the effects of K_2O on the surface electron properties and the activation of CO on the surface of copper model catalyst through DFT calculation, the other is the attempt to improve the performance of K-ZnCr iso-butanol catalyst by both modulating the structure of the catalyst through controlling the precipitation conditions and doping Ga^{3+}. By means of the above work, a series of interesting conclusions were obtained in this thesis and listed below.

As mentioned in chapter 1, K_2O interacted strongly with Cu (111) surface through the atom oxygen and surface copper. By denoting its electron to Cu surface, the direct

dissociation of CO become much easier, methanol formation through CH_3O hydrogenation is suppressed owing to the increased activation energy by K_2O adsorption. However, after adsorption of K_2O, C_2 oxygenate formation becomes easier. The most favorable C_2 oxygenate formation route is through CH_2O and CH_2 formed through CH_2O dissociation.

As mentioned in chapter 2, the performance of K-ZnCr iso-butanol catalyst can be modulated by controlling the co-precipitation temperature. For ZC-60, the highest performance of iso-butanol synthesis is obtained: conversion of CO reaches 16.31 %, the selectivity of alcohol and iso-butanol are 53.49 C mol% and 18.30 wt %, respectively. Characterization to the structure and surface of the catalyst samples showed that ZC-60 presented the abundant amount of OH groups, which produced plenty of formate species during CO adsorption. DFT calculation shows that the terminal ended OH group is more favorable to produce formate species which is related to the high catalyst performance.

As mentioned in chapter 3, Ga^{3+} was introduced in to K-ZnCr iso-butanol catalyst to further boost the efficiency of the catalyst. The evaluation results show that K-$Ga_{1.10}$ZnCr presented a 58.70 % increase in the space time yield and 14.62 % promotion on the selectivity of the alcohols under the reaction condition of 10.0 MPa, 3300 h^{-1} GHSV. Spectral analysis and first principle calculations revealed that Zn^{2+} ions, located at the tetrahedral site of the ZnCr spinel, were replaced by Ga^{3+} ions to form the ZG structure, which promoted the direct dissociation of CO and the formation of the CHO group. The Coordinately unsaturated $ZnCr_2O_4$ surfaces interacted with Ga or gallium

clusters which reduced the adsorption of CO along with this process. However, upon further increasing the amount of Ga^{3+}, $ZnGa_2O_4$ was formed which would modulate the morphologies, surface acidity and basicity of the final catalysts, eventually inducing poor performance of the catalysts.

List of publications

1. **Tao Zhang**, Chunyang Zeng, Yingquan Wu, Nana Gong, Jiaqian Yang, Guohui Yang, Noritatsu Tsubaki, Yisheng Tan. Role of Ga^{3+} promoter in the direct synthesis of iso-butanol via syngas over a K-ZnO/$ZnCr_2O_4$ catalyst. ***Catalysis Science & Technology,*** 2021, 11: 1077-1088.
2. **Tao Zhang**, Yingquan Wu, Junfeng Zhang, Qingde Zhang, Guohui Yang, Noritatsu Tsubaki, Yisheng Tan. Insight into activation of CO and initial C_2 oxygenate formation during synthesis of higher alcohols from syngas on the model catalyst K_2O/Cu (111) surface. ***Applied Surface Science*****,** 2019, 479: 55-63.
3. **Tao Zhang,** Yingquan Wu, Xiaofeng Gao, Hongjuan Xie, Guohui Yang, Noritatsu Tsubaki, Yisheng Tan. Effects of surface hydroxyl groups induced by the co-precipitation temperature on the catalytic performance of direct synthesis of isobutanol from syngas. ***Fuel***, 2019, 237:1021-1028.
4. Minghui Tan, Sha Tian, **Tao Zhang,** Kangzhou Wang, Liwei Xiao, Jiaming Liang, Qingxiang Ma, Guohui Yang, Noritatsu Tsubaki, Yisheng Tan. Probing Hydrophobization of Cu/ZnO Catalyst for Suppression of Water-Gas Shift Reaction in Syngas Conversion. ***ACS Catalysis***, 2021, 11:4633-4643.
5. Yingquan Wu, Li Tan, **Tao Zhang,** Hongjuan Xie, Guohui Yang, Noritatsu Tsubaki, Jiangang Chen**.** Effect of preparation method on ZrO_2-based catalysts performance for isobutanol synthesis from syngas. ***Catalysts***, 2019, 9(9):752.

6. Xiaoxing Wang, Guohui Yang, Junfeng Zhang, Faen Song, Yingquan Wu, **Tao Zhang**, Qingde Zhang, Noritatsu Tsubaki, Yisheng Tan. Macroscopic assembly style of catalysts significantly determining their efficiency for converting CO_2 to gasoline. ***Catalysis Science & Technology***, 2019, 9:5401-5412.
7. Meng Zhang, Junfeng Zhang, Zeling Zhou, Shuyao Chem, **Tao Zhang**, Faen Song, Qingde Zhang, Noritatsu Tsubaki, Yisheng Tan, Yizhuo Han. Effects of the surface adsorbed oxygen species tuned by rare-earth metal doping on dry reforming of methane over Ni/ZrO_2 catalyst. ***Applied Catalysis. B: Environmental***, 2020, 264: 1-12.
8. Zhenzhou Zhang, Qingde Zhang, Lingyu Jia, Wenfeng Wang, **Tao Zhang**, Yizhuo Han, Noritatsu Tsubaki, Yisheng Tan. Effects of tetrahedral molybdenum oxide species and MoO_x domains on the selective oxidation of dimethyl ether under mild conditions. ***Catalysis Science & Technology***, 2016, 6:2975-2983.

Acknowledgements

At the end of this thesis, I would like to express deepest gratitude to Professor Noritatsu Tsubaki, my academic advisor. He gave me a precious opportunity to learn more in the area of syngas conversion which enables me to deep understand the science of catalysis. For his patient guidance and continued encouragement and support through the course of this study. I am always inspired by his love of science and strong working enthusiasm.

I am greatly appreciative to Professor Guohui Yang and Professor Yisheng Tan in Institute of Coal Chemistry, Chinese Academy of Science for their assistance during preration this thesis and kindhearted suggestion in the research. Besides, my appreciation also extend to Dr. Yingluo He, Dr. Minghui Tan, Professor Yizhuo Han, Professor Qingde Zhang, Professor Junxuan Pan, Professor Hongjuan Xie, Dr. Yingquan Wu, Dr. Junfeng Zhang, Dr. Xiaoxing Wang and Dr. Faen Song for their deepfriendship and great help.

Furthermore, I would like to give my thanks to students in present 902 research group of Institute of Coal Chemistry, Chinese Academy of Science and graduated from here for their great help.

Last but not the least, my thanks would go to my family for their long time support and great confidence in me. Only with their selfless support have I been able to accomplish the PhD study.